



ENGINYERIA ELECTRÒNICA ELÈCTRICA I AUTOMÀTICA

**UNIVERSITAT ROVIRA I VIRGILI**

Graduate Students Meeting on Electronics Engineering  
Tarragona and Online, July 1st and 2nd, 2021



**BOOK OF ABSTRACTS**





<b>Index</b>	3
<b>Program.</b>	5
<b>Keynote Talks</b>	7
<b>Students Proceedings</b>	13
Aristeidis Nikolaou Analytical Charge-Based Model for the Bias-Depended Drain-Current Variability in Organic Thin-Film Transistors	15
Kerim Yilmaz Quantum Confinement in Thin Body Multiple-Gate MOSFETs	17
Jakob Leise Channel-Segmentation Model for the Simulation of Organic Thin-Film Transistor Circuits Including Non-Quasistatic Effects	19
Sara M. de Cripán Machine learning-based retention time prediction of trimethylsilyl derivatives of metabolites	21
Christian Roemer Closed-Form Field Emission Current Model for Schottky Barrier Field-Effect Transistors	23
Jakob Pruefer Generic Scheme to Model the Schottky Barrier at the Drain Contact of Organic Transistors	25
Beatriu Domingo Tafalla Iron-doped carbon dots as electrocatalysts for CO <sub>2</sub> reduction	27
Maria Llambrich Automated data analysis workflow for GCxGC-TOF-MS measurements	29
S. Valedsaravi Grid-connected LCL Filter Design with Different Damping Methods	31
Shuja Bashir Malik Synthesis conditions optimization of zinc oxide (ZnO) hierarchical nanostructures for gas sensing applications	33
Eric Navarrete Chemical Vapor Deposited ZnO Nanowires for Ethanol and NO <sub>2</sub> Gas Detection	35

Pankaj Kapruwan	
Optical Platform to Analyze a Model Drug-Loading and Releasing Profile Based on Nanoporous Anodic Alumina Gradient Index Filters	39
Carla Merino	
Metabolic Dysregulations Associated to Thirdhand Smoke Exposure in Mice: Implications for Human Urine Biomonitoring	41
X. Genaro-Muñoz	
Contribution to the Development of a Multifrequency Energy Distribution System for Battery Charging in Electric Vehicles	43
Mohamed Ayoub Alouani	
Gas Sensing Properties of Perovskite Decorated Graphene	45
Lluc Sementé	
Modelization and annotation of peptides to reconstruct the spatial distribution of proteins in MALDI MSI using rMSIannotation	47
Aanchal Alagh	
3D assembly of WS <sub>2</sub> nanomaterial for H <sub>2</sub> S gas sensing application	49
Ramon Estalella	
Numerical approach to input filter design for switching converters	51
Gerard Baquer	
An automated annotation tool of lipid adducts and in-source fragments in MALDI-MSI	53
J.M. Badia	
MS2ID: An R package for high throughput mass spectral annotation	57





ENGINYERIA ELECTRÒNICA ELÈCTRICA I AUTOMÀTICA

UNIVERSITAT ROVIRA I VIRGILI

Graduate Students Meeting on Electronics Engineering

Tarragona and Online, July 1st and 2nd, 2021

# Program

Thursday, July 1<sup>st</sup>:

12.00 - Opening

12.10 – M.K. Radhakrishnan (NanoRel, Singapore)

“Revisiting a Birth which Impacted Humanity in Seven Decades”

13.30 – Pierrick Clément (EPFL, Switzerland)

“Integration of nano-engineered carbon nanotube hybrids on MEMS for (bio)sensing application”

16.30 – Adam Skorek (Université Québec Trois Rivières, Canada)

“Biofields and bioelectronics in Human-Machine interfaces”

Friday, July 2<sup>nd</sup>:

9.30 – Tushar Kumeria (University of New South Wales, Australia)

“Porous nanomaterials for biomedical applications”

11.00 – Ph. D. Students Oral Presentations

- Sara Martínez de Cripán - “Machine learning-based retention time prediction of trimethylsilyl derivatives of metabolites”

- Pankaj Kapruwan - “Optical Platform to Analyze a Model Drug-Loading and Releasing Profile Based on Nanoporous Anodic Alumina Gradient Index Filters”

- Xavier Genaro - “Contribution to the Development of a Multifrequency Energy Distribution System for Battery Charging in Electric Vehicles”

12:00 - Christoph Bookmeyer (Institut d’Investigació Sanitària Pere Virgili)

“Post-ionization techniques in MALDI mass spectrometry imaging”

13.30 - Closing





ENGINYERIA ELECTRÒNICA ELÈCTRICA I AUTOMÀTICA

---

**UNIVERSITAT ROVIRA I VIRGILI**

Graduate Students Meeting on Electronics Engineering

# Keynote Talks



## **M.K. Radhakrishnan**

### *Revisiting a Birth which Impacted Humanity in Seven Decades*

A birth, though looks accidental, soon after the end of second world war was not hailed too much during those days. However the child grew slowly, but steadily with many siblings during the next decades and the associated growth has captured all walks of human activities. The influence is such that even the breathing of present society is so controlled by the stimulus of this development.

A worldwide appraisal during the end of the last century gave the top rank to this tiny device – transistor. However, the related conglomerate of integrated circuit could start about 10 years later only after marathon efforts. However, the technology progression which happened during the following years has immensely helped in understanding various materials and interfaces at the most miniaturized scale. The studies in turn have helped in developing many useful tools and techniques for the benefit of mankind. All the technological innovations and related advancements in the society – life style, health care, entertainment, etc - are indebted to semiconductor device technology.

Currently, we stand at another juncture as well, where the fruits of developments in the last century science and the depth of knowledge mankind acquired through research in material science and various mathematical tools merge to emerge in the form of artificial intelligence, machine learning, quantum technology, etc as new sets of advancements in technological evolution. The progression of device technology and its transformation from micro to nano-electronics and to present stage will be discussed in this talk.

The major challenges in analysis and metrology are discussed with relevance to the limitations in application of the tools and the complexity in analysis. Understanding the device physics in terms of electron conduction through various interfaces can provide a deep insight into the challenges in the technology progression. The objective is to provide a broad picture of the vast area for study in the field of device technology, where the importance still lies on understanding the fundamentals of device physics, materials and interfaces.

## Pierrick Clément

### *Integration of nano-engineered carbon nanotube hybrids on MEMS for (bio)sensing application*

For (bio)chemical sensing applications, a simultaneous on-site detection of different analytes from a single sample with low system complexity has recently gained increasing importance especially for *in vitro* point-of-care diagnostic tests and environmental monitoring. Multiplexed nanoscale artificial systems with high-integration of transducer is a very promising technology to tackle this challenge. However, fragile functional nanomaterials with low atomic layers and “soft” biological probes face unsolved problems related to their integration at an individual level into devices without altering their properties during the fabrication steps. I aim to nano-engineer on single-walled carbon nanotubes (SWCNTs) with sub-nanoscale precision to control the exact position of molecules and atoms for the successful construction of ground-breaking nano-architectures to circumvent current performance limitations.

## **Adam Skorek**

### *Biofields and bioelectronics in Human-Machine interfaces*

Human-Machine Interfaces (HMI) based on biofields and bioelectronics are present in electrical, electronics, and computer engineering for years. In particular, the biofields defined as electromagnetics and thermal fields in living matter are naturally related to HMI studies and applications, including brain analysis with numerical modeling and simulations. Brain functionalities are inspiring all developments in Artificial Intelligence (AI), from theoretical investigations to machine learning, humanoid robots, and brains interface devices implementation, where bioelectronics combine applications of electronics with not only knowledge of the living matter but also their appropriate integration. The brain biofields interactions with external excitations as 5G telecommunications devices, transcranial magnetic stimulation and even directly with other brains biofields, are currently investigated and applied so more as never before. A presentation from a worldwide perspective of some modern research works with their results impacts is completed by the lecturer's experiences and guidelines for the future. Some practical examples and instructions for researchers, engineers and students are presented, stimulating the audience to various scientific as well R&D activities in this so promising area.

**Tushar Kumeria**

*Porous nanomaterials for biomedical applications*

**Christoph Bookmeyer**

*Post-ionization techniques in MALDI mass spectrometry imaging*





ENGINYERIA ELECTRÒNICA ELÈCTRICA I AUTOMÀTICA

---

**UNIVERSITAT ROVIRA I VIRGILI**

Graduate Students Meeting on Electronics Engineering

# Students Proceedings



# Analytical Charge-Based Model for the Bias-Depended Drain-Current Variability in Organic Thin-Film Transistors

Aristeidis Nikolaou, Jakob Leise, Jakob Pruefer, Ghader Darbandy, Benjamin Iñiguez, Alexander Kloes

**Abstract**—In this study, a consistent analytical charge-based model for the bias-dependent variability of the drain current of organic thin-film transistors is presented. The proposed model combines both charge-carrier-number-fluctuation effects and correlated-mobility-fluctuation effects to predict the drain-current variation and is verified using experimental data acquired from a statistical population of organic transistors with various channel dimensions, fabricated on flexible polymeric substrates.

## I. INTRODUCTION

Drain-current variability can be perceived as the time-independent variation of the drain current of two or more nominally identical transistors under the same biasing conditions. Drain-current variability of organic-TFT-based circuits is commonly determined using circuit-based Monte Carlo simulations [1] or novel noise-based simulation approaches [2], [3]. Here, a device-level charge-based variability model is introduced. The proposed physical model has two fitting parameters and can be applied directly to the experimental statistical population without the need for Monte Carlo or Noise-based simulations.

## II. DEVICES AND MEASUREMENTS

Organic p-channel TFTs with channel lengths ( $L$ ) of 2  $\mu\text{m}$ , 3  $\mu\text{m}$  and 5  $\mu\text{m}$  and a channel-width-to-length ratio ( $W/L$ ) of 10, were fabricated on a 125  $\mu\text{m}$ -thick flexible polyethylene naphthalate (PEN) substrate in the inverted coplanar (bottom-gate, bottom-contact) device architecture, using stencil lithography based on high-resolution silicon stencil masks [4]. The TFTs consist of 25 nm-thick aluminum gate electrodes, a 5.3 nm-thick hybrid  $\text{AlO}_x/\text{SAM}$  gate dielectric, 30 nm-thick gold (Au) source and drain contacts coated with a pentafluorobenzene-thiol (PFBT) monolayer and a 25 nm-thick vacuum-deposited layer of the small-molecule organic semiconductor DPh-DNTT [5]. The maximum process temperature was 90  $^\circ\text{C}$ . For each channel length, 16 nominally identical TFTs were fabricated and characterized. The measurement protocol

This project is funded by the German Federal Ministry of Education and Research ("SOMOFLEX", No. 13FH015IX6) and the German Research Foundation (DFG) under the grant KL 1042/9-2 (SPP FFlexCom). We would like to thank U. Zschieschang and H. Klauk (Max Planck Institute for Solid State Research, Stuttgart 70569, Germany) for the substrate fabrication and AdMOS GmbH for support.

A. Nikolaou, J. Leise, J. Pruefer, G. Darbandy and A. Kloes are with NanoP, TH Mittelhessen University of Applied Sciences, 35390 Giessen, Germany (e-mail: aristeidis.nikolaou@ei.thm.de). A. Nikolaou, J. Leise, J. Pruefer and B. Iñiguez are with DEEEA, Universitat Rovira i Virgili, Tarragona, Spain.

comprises transfer characteristics at a drain-source voltage ( $V_{DS}$ ) of  $-3.0\text{ V}$  and gate-source voltages ( $V_{GS}$ ) from 0 to  $-3.0\text{ V}$  with a step size of  $-50\text{ mV}$ , recorded at room temperature.

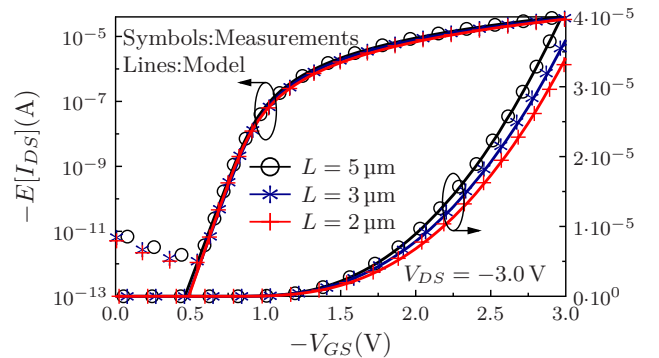


Fig. 1. Mean-value drain current  $E[I_{DS}]$  versus gate-source voltage of coplanar DPh-DNTT TFTs with channel lengths ( $L$ ) of 2  $\mu\text{m}$ , 3  $\mu\text{m}$  and 5  $\mu\text{m}$ . Symbols: measurement data, solid lines: model.

## III. DRAIN-CURRENT-VARIABILITY-MODEL

For the derived variability model, the charge-based organic-TFT model described in [6] is the basis. The proposed current-voltage model provides a single current equation that is valid for all operation regions that can be obtained from

$$I_{DS} = \mu W \left( \frac{kT}{q} \frac{Q_S - Q_D}{L} + \frac{Q_S^2 - Q_D^2}{2LC'_{ox}} \right) \times (1 + \lambda (V_{DS} - V_{Dsat})), \quad (1)$$

where  $W$  is the channel width,  $L$  is the channel length,  $C'_{ox}$  is the unit-area gate-dielectric capacitance,  $\lambda$  is the channel-length modulation factor and  $\mu$  is the effective carrier mobility.  $Q_S$  and  $Q_D$  describe the density of quasi-mobile charges per gate area at the source and drain end of the channel, respectively and can be expressed as

$$Q_{S,D} = \frac{S}{\ln(10)} C'_{ox} \mathcal{L} \left\{ \exp \left( \frac{V_{GS,D} - V_{T0}}{S/\ln(10)} \right) \right\}, \quad (2)$$

where  $\mathcal{L}$  is the first branch of the Lambert W function,  $S$  is the subthreshold swing and  $V_{T0}$  is the threshold voltage. The variance of the total normalized drain-current fluctuation is given by

$$\frac{\sigma^2 I_D}{I_D^2} = C^* |_{\Delta N} B^*(q_{ch}) |_{\Delta N} \quad (3)$$

where

$$C^*|_{\Delta N} = \frac{q^4 N_t}{WLa^2(kT)^2 C_{ox}^2} \quad (4)$$

and

$$B^*(q_s, q_d)|_{\Delta N} = \frac{1}{i_d} \left( \frac{2(a-1)a^*\mu}{a} + 1 \right) \ln \left( \frac{1+aq_s}{1+aq_d} \right) + \frac{1}{i_d} \left( \frac{1-a}{1+aq_s} - \frac{1-a}{1+aq_d} \right) + (a^*\mu)^2 + \frac{1}{i_d} 2(a^*\mu)(q_s - q_d). \quad (5)$$

The normalized drain current  $i_d$  can be expressed as  $i_d = I_D/\mu(aU_T)^2 C_{ox}' W/L$ . The terms  $q_s = Q_S/Q^*$  and  $q_d = Q_D/Q^*$  account for the normalized charge densities at the source and drain end of the channel, respectively. The terms  $N_t$  and  $a^*$  are the fitting parameters of the variability model.  $N_t$  accounts for the variability due to the carrier-number-fluctuation effect and can be extracted at the subthreshold region. Parameter  $a^*$  expresses drain-current variability due to mobility-fluctuation and can be extracted at the maximum gate-source and drain-source voltages. The detailed derivation of the drain-current variability model is thoroughly described in [7]. Note that neither the current-voltage model nor the proposed variability model cover the off-state regime (leakage current region) below the turn-on (switch-on) voltage, i.e., the range of gate-source voltages between 0 and  $-0.5$  V.

#### IV. RESULTS AND DISCUSSION

Fig. 1 shows the mean-value transfer characteristics of DPH-DNTT TFTs fabricated in the coplanar device architecture, having channel lengths ( $L$ ) of  $2\mu\text{m}$ ,  $3\mu\text{m}$  and  $5\mu\text{m}$ , for a drain-source voltage of  $-3.0$  V. The experimental mean values were calculated over a population of 16 nominally identical TFTs fabricated on the same substrate. Symbols represent the measurement data and lines represent the results of the current-voltage model. In Fig. 2, the standard deviation of the drain current normalized to the device area  $\sigma(I_{DS}/WL)$  is plotted as a function of the gate-source voltage  $V_{GS}$  for the three different channel lengths. Table I summarizes the values of  $N_t$  and  $a^*$  extracted from the variability model and the effective carrier mobilities of the coplanar DPH-DNTT TFTs for each channel length at the maximum gate-source and drain-source voltages.

#### V. CONCLUSIONS

In conclusion, we have developed a physical charge-based drain-current variability model suitable for organic thin-film transistors. The proposed model is based on charge-carrier-number-fluctuation and correlated-mobility-fluctuation effects and can be applied to TFTs fabricated in the coplanar device architecture. We have shown that the drain-current variability decreases with increasing TFT area (product of channel length and channel width), particularly in the subthreshold region. We also found that the value of the parameter  $a^*$  tends to increase with decreasing channel length, due to the fact that a smaller channel length causes a smaller effective carrier mobility and more pronounced edge effects. Regardless of the channel

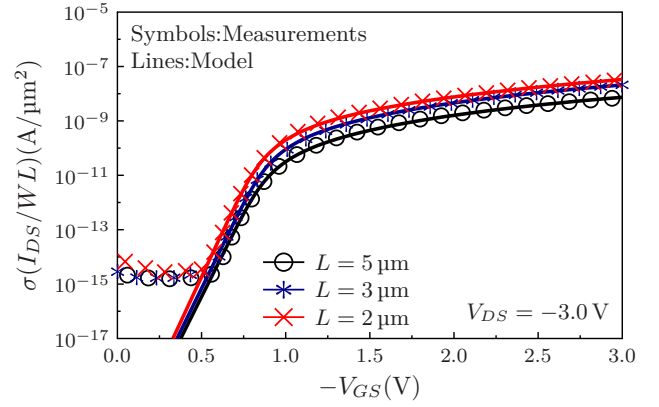


Fig. 2. Standard deviation of the drain current normalized to the device area  $\sigma(I_{DS}/WL)$  versus gate-source voltage of the same TFTs. Symbols: measurement data, solid lines: model

dimensions and the device architecture, the results of the proposed model are in good agreement with the experimentally measured bias-dependent drain-current variability of organic TFTs.

TABLE I  
EXTRACTED PARAMETERS OF THE VARIABILITY MODEL

	$N_t$ ( $\text{m}^{-2}$ )	$a^*$ ( $\text{Vs}/\text{m}^2$ )	$\mu_{eff}$ ( $\text{cm}^2/\text{Vs}$ )
$L = 5\mu\text{m}$	$1.5 \times 10^{19}$	625	3.3
$L = 3\mu\text{m}$	$7.5 \times 10^{18}$	850	3.0
$L = 2\mu\text{m}$	$6.0 \times 10^{18}$	430	2.7

#### REFERENCES

- [1] S. Jacob, S. Abdinia, M. Benwadih, J. Bablet, I. Chartier, R. Gwoziecki, E. Cantatore, A. van Roermund, L. Maddiona, F. Tramontana, G. Maiellaro, L. Mariucci, M. Rapisarda, G. Palmisano, and R. Coppard, "High performance printed n and p-type OTFTs enabling digital and analog complementary circuits on flexible plastic substrate," *Solid-State Electronics*, vol. 84, pp. 167–178, 2013.
- [2] A. Nikolaou, J. Leise, J. Pruefer, U. Zschieschang, H. Klauk, G. Darbandy, and A. Kloes, "Noise based variability approach for DC statistical analysis of organic TFT based circuits," in *2020 IEEE Latin America Electron Devices Conference (LAEDC)*, 2020, pp. 1–4.
- [3] A. Nikolaou, J. Leise, J. Pruefer, U. Zschieschang, H. Klauk, G. Darbandy, B. Iniguez, and A. Kloes, "Noise-based simulation technique for circuit-variability analysis," *IEEE Journal of the Electron Devices Society*, vol. 9, pp. 450–455, 2021.
- [4] U. Zschieschang, F. Letzkus, J. N. Burghartz, and H. Klauk, "Parameter uniformity of submicron-channel-length organic thin-film transistors fabricated by stencil lithography," *IEEE Transactions on Nanotechnology*, vol. 16, no. 5, pp. 837–841, 2017.
- [5] J. W. Borchert, U. Zschieschang, F. Letzkus, M. Giorgio, R. T. Weitz, M. Caironi, J. N. Burghartz, S. Ludwigs, and H. Klauk, "Flexible low-voltage high-frequency organic thin-film transistors," *Science Advances*, vol. 6, no. 21, 2020.
- [6] F. Hain, M. Graef, B. Iniguez, and A. Kloes, "Charge based, continuous compact model for the channel current in organic thin-film transistors for all regions of operation," *Solid-State Electronics*, vol. 133, pp. 17–24, 2017.
- [7] A. Nikolaou, G. Darbandy, J. Leise, J. Pruefer, J. W. Borchert, M. Geiger, H. Klauk, B. Iniguez, and A. Kloes, "Charge-based model for the drain-current variability in organic thin-film transistors due to carrier-number and correlated- mobility fluctuation," *IEEE Transactions on Electron Devices*, vol. 67, no. 11, pp. 4667–4671, 2020.

# Quantum Confinement in Thin Body Multiple-Gate MOSFETs

Kerim Yilmaz, Ghader Darbandy, Benjamín Iñíguez, François Lime and Alexander Kloes

**Abstract**—In this work, a mathematical correlation regarding quantum confinement (QC) for thin body transistors is derived, which shows that the mostly unwanted quantum effects occur in gate-all-around (GAA) structures already for thicker channels compared to double-gate (DG) transistors. Both transistor types experience a comparable influence with regard to quantization if the channel thickness of GAA FETs is 53% more than that of DG FETs.

**Index Terms**—Compact Modeling, Device Simulation, Double-Gate (DG), Equivalent Dimensions, MOSFET, Nanowire GAA FET, Quantum Confinement, Quantum-Mechanical Simulation, Short-Channel, Thin Body

## I. INTRODUCTION

The closer the device dimensions get to the single-digit nanometer range, the more quantum-mechanical effects (QME) must be considered in device modeling. The two most significant but not desired ones are quantum confinement (QC) from gate-to-gate and direct source-to-drain tunneling (DSDT). The former belongs to the category of thin body effects (TBE) and the latter to short-channel effects (SCE). Other SCEs such as the degradation of the subthreshold swing ( $S_{\text{sth}}$ ) and the drain-induced barrier lowering (DIBL) can be suppressed to some extent by increasing the electrostatic gate control through enclosing the entire channel with gate material. Therefore, GAA FETs are usually of greater interest and the most promising devices. This measure to reduce SCEs also inevitably have an influence on TBEs.

The critical channel thickness  $T_{\text{ch}}$  and channel width  $W_{\text{ch}}$  below which QC effects appear are declared to be 10 nm for DG FETs [1]–[3] and assumed to be the same in GAA FETs [4], [5]. The influence of channel width and thickness has been extensively discussed and successfully modeled in recent scientific work on nanosheet FETs [6]. The non ideal conditions for the subband energies based on an ideal 1-D particle-in-a-box model with infinite boundaries are circumvented by introducing empirically determined fitting parameters. The model works for a certain range of aspect ratio of nanosheet FETs, but cannot simply be extended to a comparison of different MG configurations.

Kerim Yilmaz is with NanoP, TH Mittelhessen - University of Applied Sciences, Giessen, Germany and also with the DEEEA, Universitat Rovira i Virgili, Tarragona, Spain (e-mail: kerim.yilmaz@ei.thm.de).

Benjamín Iñíguez and François Lime are with DEEEA, Universitat Rovira i Virgili. Alexander Kloes and Ghader Darbandy are with NanoP, THM.

## II. QUANTUM CONFINEMENT

In this section we investigate the role and compare the influence of QC in the direction normal to the silicon/oxide interface on the current in MOSFETs with different MG configurations and relate them to each other. In detail we focus on the energetic distance  $\Delta E^{\text{QC}}$  of the first subband from the conduction band edge. We consider the quantum effects in DG, quadratic quadruple-gate (QG) and cylindrical GAA transistors by assuming a 2-D infinite potential well in confinement direction. In [7] the 2-D, time-independent, free-particle Schrödinger equation, in the relevant Cartesian or cylindrical coordinates has been solved, so that the following smallest energy levels appear:

$$\text{DG: } \Delta E_{\text{DG}}^{\text{QC}} = \frac{\hbar^2}{2 m_{\text{eff}} T_{\text{ch}}^2} \cdot \pi^2 \quad (1)$$

$$\text{QG: } \Delta E_{\text{QG}}^{\text{QC}} = \frac{\hbar^2}{2 m_{\text{eff}} T_{\text{ch}}^2} \cdot 2\pi^2 \quad (2)$$

$$\text{GAA: } \Delta E_{\text{GAA}}^{\text{QC}} = \frac{\hbar^2}{2 m_{\text{eff}} T_{\text{ch}}^2} \cdot 4 \cdot 2.4048^2, \quad (3)$$

where  $\hbar$  is the reduced Planck constant and  $m_{\text{eff}}$  is the effective electron mass. To achieve the same quantum mechanical influence, the parameters  $\Delta E^{\text{QC}}$  are set equal and resolved according to their radii as follows:

$$\Delta E_{\text{DG}}^{\text{QC}} = \Delta E_{\text{GAA}}^{\text{QC}} \leftrightarrow T_{\text{ch}}^{\text{GAA}} = 1.53 T_{\text{ch}}^{\text{DG}} \quad (4)$$

$$\Delta E_{\text{DG}}^{\text{QC}} = \Delta E_{\text{QG}}^{\text{QC}} \leftrightarrow T_{\text{ch}}^{\text{QG}} = \sqrt{2} T_{\text{ch}}^{\text{DG}} \quad (5)$$

Both (4) and (5) predict that the influence of QC increases significantly with the increasing number of gates around the channel and with their shrinking distance from channel center. Hence, the largest QC effect occurs in cylindrical GAA transistors. So it has to be weighed up, what is preferred more, increase the device performance by more gates and thus less SCEs or weaken it simultaneously because of stronger quantization. Furthermore, it can be concluded that the critical channel thickness for GAA transistors, below which QC effects cannot be neglected, is 15 nm instead of 10 nm.

In [8] QC is implemented at two places in our modified DG compact model for GAA FETs. Firstly, a quasi classical implementation is done by reducing the intrinsic charge carrier concentration  $n_i$  due to the widening of the band gap  $E_G$ . For simplicity, the same  $\Delta E^{\text{QC}}$  has been assumed for conduction and valence band. Since  $n_i$  is exponentially related to the band gap as

$$n_i \propto \exp\left(-\frac{E_G}{2 k_B T}\right), \quad (6)$$

the effective intrinsic charge carrier concentration  $n_{i,\text{eff}}$  for GAA FETs is given as

$$n_{i,\text{eff}} = n_i \cdot \exp\left(-\frac{\Delta E_{\text{GAA}}^{\text{QC}}}{k_B T}\right). \quad (7)$$

Secondly, we know from various publications that QC increases the threshold voltage ( $V_T$ ) [2], [3]. This can be explained by the fact that with a larger band gap the potential barrier becomes larger. Thus the inversion potential  $\Phi_i$  increases by  $\Delta E^{\text{QC}}/q$ . The impact of QC on  $V_T$  can be given by the relationship that a change in gate potential with respect to changes in surface potential ( $\Phi_S$ ) is equal to the change in  $V_T$  with respect to the changes in band gap due to QC. Thus the following applies in general to the threshold voltage shift:

$$\Delta V_T^{\text{QC}} = \frac{dV_{\text{GS}}}{d\Phi_S} \Delta E^{\text{QC}}/q. \quad (8)$$

In analogy to [9] we obtained  $V_T$  by linear extrapolating  $\Phi_S$  in the subthreshold region to an inversion potential  $\Phi_i$ , which is used as a fitting parameter.

It should be noted that the impact of QC on the mobility has been neglected in this work. For simplicity, the used mobility model corresponds to the one in [10] and includes the perpendicular gate electric field and velocity saturation effects. Nevertheless, a more sophisticated model as proposed in [11] could easily be implemented.

### III. RESULTS AND DISCUSSION

To determine the impact of the confined electron carrier density on the quasi-Fermi level we need to consider several valleys in the band structure instead of the single-valley representation. Quantization effects are implemented in Synopsys TCAD Sentaurus simulations with the connection to an external parabolic 2-D Schrödinger solver, which is the physically most sophisticated model.

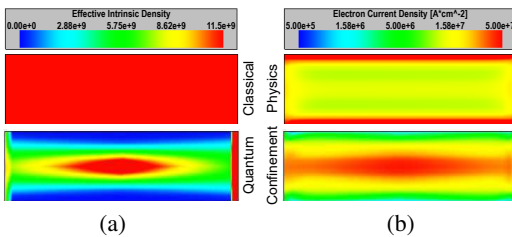


Fig. 1. Comparison of the effective intrinsic density of free electrons (a) and the electron current density inside of the channel (b) between classical physics and activated quantum confinement for  $R = 3$  nm,  $L_{\text{GAA}} = 20$  nm,  $T_{\text{ox}} = 1$  nm,  $V_{\text{gs}} = 1$  V and  $V_{\text{ds}} = 0.1$  V.

In Fig. 1 we see the change in effective intrinsic density and electron current density within the channel from classical physics to that with activated QC of an ultra-thin GAA FET. Both show that the charge and current distribution is changing dramatically due to the wave characteristic of electrons in a quantum-mechanical approach. The boundary condition for the wave function at the channel/oxide interface is near to zero. Thus the probability to locate there an electron goes towards zero as well. As a consequence, the QC forces the charge to the center of the channel. Even in the on-state, where the potential barrier at the channel surface is smaller than at the center, the

inversion channel is formed along the channel center. This is due to the relatively higher density of states in this area.

In Fig. 2 we compare the impact of QC on the transfer characteristics between GAA and DG simulations. First of all, the chosen channel length is long enough to avoid SCE and to focus only on the quantum-mechanical impact on the current. With this plot we verify the accuracy of the conversion factor in (4) and proof simultaneously that current reduction by QC occurs already for larger channel thickness ( $T_{\text{ch}}$ ) in MG transistors. If  $T_{\text{ch}}$  is equal to 6 nm, then the extent of current reduction and threshold voltage increase for GAA transistors is significantly greater. The classical current is divided by 12.8 (GAA) compared to 2.8 (DG). If the channel thickness of the same transistor is larger by a factor of 1.53, then the effect is comparable to that of DG FETs without increasing the channel thickness. Now the classical subthreshold current is divided by 2.9 (GAA), which is very close to 2.8 (DG).

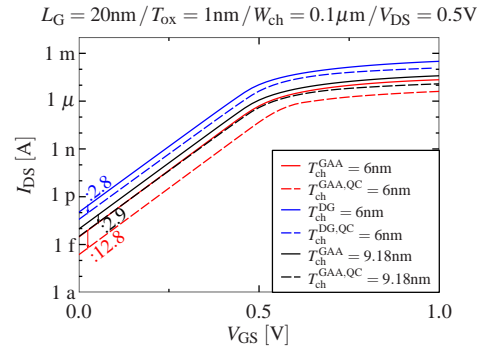


Fig. 2. Comparison of the transfer characteristics between GAA and DG simulations with classical (solid lines) or with activated quantum confinement (dashed lines).

### IV. CONCLUSIONS

We analyzed the effect of circular QC and clearly showed by simulation that a full surrounding of the channel with gate material results in a higher critical channel thickness and hence an earlier onset of the undesired quantum effects. Furthermore, it was shown that in the on-state, the inversion channel does not form at the surface as usual, but along the channel center. In addition, the current strength decreases significantly due to lower density of states and effectively higher band gap.

### REFERENCES

- [1] A. S. Medury and H. Kansal, *2019 IEEE EDSSC*, Jun. 2019.
- [2] Y. Omura, S. Horiguchi, M. Tabe and K. Kishi, *IEEE Electron Device Letters*, vol. 14, no. 12, pp. 569–571, Dec. 1993.
- [3] H. Majima, H. Ishikuro and T. Hiramoto, *IEEE Electron Device Letters*, vol. 21, no. 8, pp. 396–398, Aug. 2000.
- [4] D. Sharma and S. K. Vishvakarma, *SSE*, vol. 86, pp. 68–74, Aug. 2013.
- [5] H. A. E. Hamid, B. Iñíguez and J. R. Guitart, *IEEE Transactions on Electron Devices*, vol. 54, no. 3, pp. 572–579, Mar. 2007.
- [6] A. Dasgupta, S. S. Parihar, P. Kushwaha, H. Agarwal, M.-Y. Kao, S. Salahuddin, Y. S. Chauhan and Chenming Hu, *IEEE Transactions on Electron Devices*, vol. 67, no. 2, pp. 730–737, Feb. 2020.
- [7] C. W. David, "The Particle in a Box (and in a Circular Box)," *Chemistry Education Materials*, 2006.
- [8] K. Yilmaz, G. Darbandy, Gilles Reimbold, B. Iñíguez, F. Lime and A. Kloes, *IEEE TED*, vol. 67, no. 12, pp. 5381–5387, Dec. 2020.
- [9] A. Kloes, M. Schwarz, T. Holtij and A. Navas, *IEEE Transactions on Electron Devices*, vol. 60, no. 8, pp. 2691–2694, Aug. 2013.
- [10] A. Kloes, M. Schwarz and T. Holtij, *IEEE Transactions on Electron Devices*, vol. 59, no. 2, pp. 349–358, Feb. 2012.
- [11] A. Dasgupta, S. S. Parihar, H. Agarwal, P. Kushwaha, Y. S. Chauhan and C. Hu, *IEEE EDL*, vol. 41, no. 3, pp. 313–316 Mar. 2020.



# Channel-Segmentation Model for the Simulation of Organic Thin-Film Transistor Circuits Including Non-Quasistatic Effects

Jakob Leise, Jakob Pruefer, Aristeidis Nikolaou, Ghader Darbandy,  
Benjamin Iniguez, Alexander Kloes

**Abstract**—A charge-based macro model for small-signal AC and transient analyses of organic thin-film transistors (TFTs) has been developed. Due to the comparatively small charge-carrier mobility in organic TFTs, the dynamic behavior of the gate-field-induced carrier channel is greatly influenced by the frequency of the applied gate-source and drain-source voltages. The model presented here is based on the formerly developed charge-based DC and AC models and provides an extension in order to describe the frequency-dependent behavior of charges. The model is compared to the results of frequency-dependent admittance measurements and of numerical simulations of the transient switching behavior of organic TFTs fabricated in the staggered architecture and provides a good agreement. The model has been implemented in the hardware description language Verilog-A.

**Index Terms**—AC analysis, capacitance model, charge-based model, macro modeling, non-quasistatic behavior, organic thin-film transistors, transient analysis

## I. INTRODUCTION

Organic thin-film transistors (TFTs) are of interest for flexible, large-area electronics applications, such as active-matrix displays and integrated circuits [1]. For the design of such systems, a preliminary simulation is required, which ideally makes use of compact models that describe the physical behavior of the devices in an accurate and computationally efficient manner [2]. In this paper, we describe an extension of the charge-based DC [3] and AC [4] models developed previously in our group in order to capture non-quasistatic effects. The reason why transistors in general show a non-quasistatic behavior is that accumulation charges cannot be created or disappear, but they have to leave or enter the transistor through the drain and source contacts. Since the charge-carrier channel has an Ohmic resistance, the charges cannot reach a certain position in the channel with infinite speed. The channel capacitances and the Ohmic resistance of the channel behave like a distributed RC transmission line.

This project is funded by the German Federal Ministry of Education and Research ("SOMOFLEX", No. 13FH015IX6) and EU H2020 RISE ("DOMINO", No. 645760), and the German Research Foundation (DFG) under the grant KL 1042/9-2 (SPP FFlexCom). We would like to thank Dr. Hagen Klauk from the Max Planck Institute for Solid State Research in Stuttgart, Germany, for providing us the measurement data and helping us in the review process. We would like to thank AdMOS GmbH for support.

J. Leise, J. Pruefer, A. Nikolaou, G. Darbandy and A. Kloes are with NanoP, TH Mittelhessen University of Applied Sciences, 35390 Giessen, Germany (e-mail: jakob.simon.leise@ei.thm.de). J. Leise, J. Pruefer, A. Nikolaou and B. Iniguez are with DEEEA, Universitat Rovira i Virgili, Tarragona, Spain.

## II. MODELING APPROACH

The transistor is modeled as a distributed RC transmission line, which for simplification purposes consists of a finite number of ( $n$ ) elements. This is a standard procedure which is also used for other transistors [5], [6]. We have presented this model in [7]. Figure 1(a) shows the schematic cross-section of an organic TFT in the staggered architecture including the transmission-line model and Fig. 1(b) shows the circuit symbol of the transistor. Each of the  $n$  capacitors represents

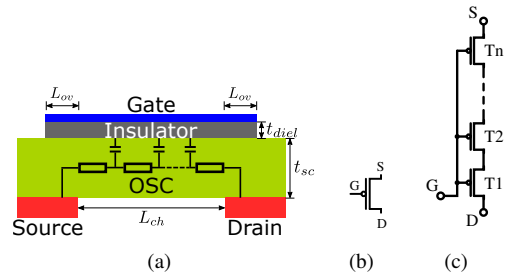


Fig. 1. (a) Schematic cross-section of an organic TFT in the staggered architecture including the transmission-line model. The capacitors represent the intrinsic channel capacitances, while the resistors represent sections of the Ohmic channel resistance [7]. (b) Symbol of the transistor [7]. (c) Circuit schematic of that transistor modeled as a series connection of  $n$  transmission-line segments [7]. The sum of the channel lengths of the  $n$  transmission-line segments in (c) is equal to the channel length of the transistor in (b).

a segment of the channel capacitance and each of the  $n$  resistors represents a segment of the gate-field induced carrier channel. In Fig. 1(c), the macro model comprising the  $n$  transistors is shown. The sum of the channel lengths of the transistor segments T1 to Tn equals  $L_{ch}$ . The transmission line conducts the same DC current as a single transistor, but the advantage of this model is that it more accurately captures the non-quasistatic effects. The reason is that, for example the channel capacitance of transistor T2 is charged through the channel resistance of T1. The frequency dependence of the capacitances is thus implicitly accounted for [5], [8].

## III. MODEL VERIFICATION

To verify the transmission-line model, staggered TFTs represented as transmission lines of various lengths were simulated in Cadence Virtuoso [9]. AC and transient analyses were performed. The results of the AC analysis are compared to the experimental results reported in [8] and to results from

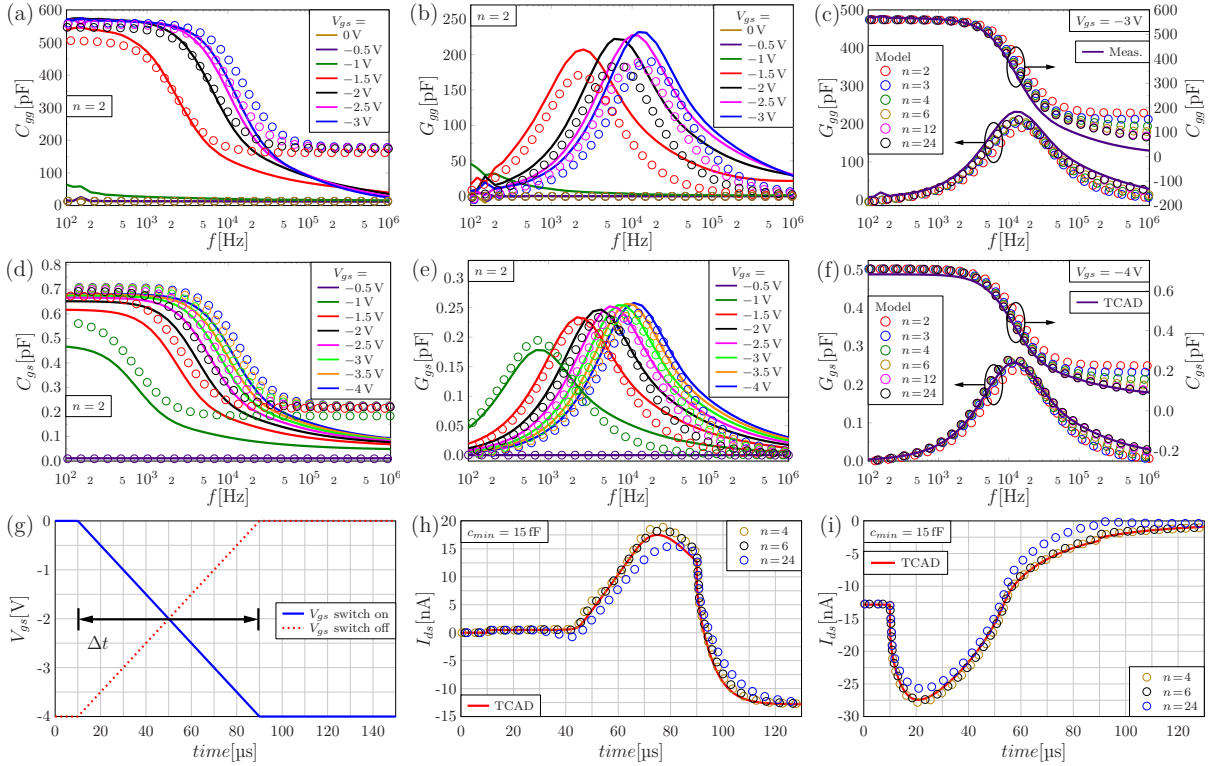


Fig. 2. (a) Gate-gate capacitance  $C_{gg}$  and (b) loss  $G_{gg}$  of an organic TFT for various gate-source voltages as a function of frequency. The experimental results reported in [8] are shown as lines, and the results of the transmission-line model are shown as symbols. In the model, the transmission line was partitioned into two segments ( $n=2$ ). (c)  $C_{gg}$  and  $G_{gg}$  of the same TFT for a gate-source-voltage of  $-3$  V as a function of frequency. The experimental results are shown as lines, and the results of the transmission-line model are shown as symbols. In the model, the transmission line was partitioned into 2, 3, 4, 6, 12 or 24 segments. (d) Gate-source capacitance  $C_{gs}$  and (e) loss  $G_{gs}$  of a TFT for various gate-source voltages as a function of frequency, similarly as presented in (a) and (b). (f)  $C_{gs}$  and  $G_{gs}$  of the same TFT for a gate voltage of  $-4$  V as a function of frequency, similarly as presented in (c). The drain-source voltage  $V_{ds}$  is 0 V for the experimental data and  $-1$  mV for the TCAD simulations and the model. (g) Gate-source-voltage transient defined for the TCAD simulations of the TFTs' switch on (solid blue line) and switch-off behavior (dotted red line). After a waiting time of 10  $\mu$ s, the gate-source voltage is ramped from 0 to  $-4$  V or from  $-4$  to 0 V, with a rise or fall time  $\Delta t = 80$   $\mu$ s. (h) Drain-current transient predicted by the transmission-line model (symbols) and the TCAD simulations (lines) in response to the switch-on process and (i) to the switch-off process. The drain-source voltage ( $V_{ds}$ ) for the transient sweep was set to  $-1$  V. All pictures are taken from [7].

TCAD Sentaurus [10] simulations. The results of the transient analysis are compared only to the simulation results. As we can see in Fig. 2, the model accurately predicts the simulated and measured capacitances and loss. Furthermore, the simulated drain-current transient is reproduced with good accuracy. For more detailed information please refer to [7].

#### IV. CONCLUSION

We have presented a macro model to describe the non-quasistatic behavior of organic TFTs fabricated in the staggered device architecture. This model is based on a charge-based quasistatic compact model and has been extended by a numerical method to capture non-quasistatic effects. We have shown that by modeling the transistor as a transmission line partitioned into a number of RC segments, each of which is modeled as a transistor, it is possible to correctly reproduce the small-signal AC and transient characteristics of organic TFTs observed experimentally and in TCAD simulations.

#### REFERENCES

- [1] J. W. Borchert, U. Zschieschang, F. Letzkus, M. Giorgio, R. T. Weitz, M. Caironi, J. N. Burghartz, S. Ludwigs, and H. Klauk, "Flexible low-voltage high-frequency organic thin-film transistors," *Science Advances*, vol. 6, no. 21, 2020, eaaz5156.
- [2] O. Marinov and M. J. Deen, "Quasistatic compact modelling of organic thin-film transistors," *Organic Electronics*, vol. 14, no. 1, pp. 295–311, 2013.
- [3] F. Hain, M. Graef, B. Iníguez, and A. Klös, "Charge based, continuous compact model for the channel current in organic thin-film transistors for all regions of operation," *Solid-State Electronics*, vol. 133, pp. 17–24, 2017.
- [4] J. Leise, J. Pruefer, G. Darbandy, M. Seifaei, Y. Manoli, H. Klauk, U. Zschieschang, B. Iniguez, and A. Kloes, "Charge-based compact modeling of capacitances in staggered multi-finger OTFTs," *IEEE Journal of the Electron Devices Society*, pp. 396–406, 2020.
- [5] C. Enz and E. Vittoz, *Charge-Based MOS Transistor Modeling: The EKV Model for Low-Power and RF IC Design / C.C. Enz, E.A. Vittoz*, 08 2006.
- [6] A. Valletta, M. Rapisarda, S. Calvi, L. Mariucci, and G. Fortunato, "A large signal non quasi static compact model for printed organic thin film transistors," in *2016 46th European Solid-State Device Research Conference (ESSDERC)*, 2016, pp. 460–463.
- [7] J. Leise, J. Pruefer, A. Nikolaou, G. Darbandy, H. Klauk, B. Iníguez, and A. Kloes, "Macromodel for ac and transient simulations of organic thin-film transistor circuits including nonquasistatic effects," *IEEE Transactions on Electron Devices*, vol. 67, no. 11, pp. 4672–4676, 2020.
- [8] T. Zaki, S. Scheinert, I. Hörselmann, R. Rödel, F. Letzkus, H. Richter, U. Zschieschang, H. Klauk, and J. N. Burghartz, "Accurate capacitance modeling and characterization of organic thin-film transistors," *IEEE Transactions on Electron Devices*, vol. 61, no. 1, pp. 98–104, Jan 2014.
- [9] Cadence Design Systems Inc., *Virtuoso® Analog Design Environment*, 2013, version IC6.1.6.
- [10] Synopsys Inc., *TCAD Sentaurus Device User Guide*, 2019, Version G-2019.12.



# Machine learning-based retention time prediction of trimethylsilyl derivatives of metabolites

Sara M. de Cripán<sup>1,2</sup>, Adrià Cereto-Massagué<sup>2</sup>, Pol Herrero<sup>2</sup>, Andrei Barcaru<sup>3</sup>,  
Núria Canela<sup>2</sup>, Xavier Domingo-Almenara<sup>1,2,4</sup>

<sup>1</sup>Metabolomics and Systems Biology Lab, Omics Sciences Unit, Eurecat – Technology Centre of Catalonia, Barcelona, Catalonia, Spain.

<sup>2</sup>Centre for Omics Sciences (COS), Eurecat – Technology Centre of Catalonia & Rovira i Virgili University joint unit, Unique Scientific and Technical Infrastructures (ICTS), Reus, Catalonia, Spain.

<sup>3</sup>Independent Researcher, Amsterdam, The Netherlands.

<sup>4</sup>Department of Electrical, Electronic and Control Engineering (DEEEA), Universitat Rovira i Virgili, Tarragona, Catalonia, Spain.

## Abstract

In gas chromatography coupled to mass spectrometry-based untargeted metabolomics, metabolites are identified by comparing mass spectra and chromatographic retention time with reference databases or standard materials analysis. However, the majority of metabolites are not commercially available or lack reference retention time in databases. The advent of machine learning in recent years has sparked broad interest in using this technology to bypass the use of experimental assays and the need of standard materials analysis. We propose a rationalized framework for machine learning-based retention time prediction of trimethylsilyl derivatives of metabolites in gas chromatography coupled to mass spectrometry.

## Introduction

Metabolites are small molecules that drive essential cellular functions, constituting the substrates and end-products of metabolism. Untargeted metabolomics aims to determine the extended range of metabolites present in a biological extract without previous knowledge of the metabolome. Gas chromatography coupled to mass spectrometry (GC-MS) is a widely used analytical platform in untargeted metabolomics for volatile and semi-volatile metabolite measurement.

Currently, molecular identification is one of the most important limitations in metabolomics [1]. Metabolites are identified by comparing mass spectra and chromatographic retention time with reference databases or standard materials analysis. However, databases are considered incomplete and standard materials are not always available.

Retention time depends on multiple variables, but the robustness of the capillary columns has facilitated the adoption of a relative retention time known as retention index (RI) [2]. Despite the utility of RI, few RI databases exist. Machine learning (ML) strategies have been designed to generate RI for any given molecule [3–5].

In GC–MS-based metabolomics, metabolites need to be derivatized to make them more volatile and protect them from thermal degradation. Despite the existence of studies focusing on GC retention time prediction using machine learning [3–5], retention index prediction of trimethylsilyl (TMS) derivatives of metabolites has been poorly studied. Herein, we have conducted a comprehensive study of the performance of retention index prediction, evaluating different machine learning paradigms and computational molecular representation fingerprint (FGPT) classes.

## RI prediction via Machine Learning models

We compared different combinations of ML methods and FGPT classes-encoding notation for molecular structures generated by different calculation software. We studied the performance of a total of five ML models: support vector machine algorithm with linear and polynomial kernel, deep neural network, convolutional neural network and random forest. Models were trained using the Golm Metabolome Database, we generated FGPTs for 1559 TMS metabolite derivatives. FGPT classes depend on the method employed to transform molecular representation into a bit string. We evaluated a total of 7 FGPT classes calculated with a combination of 5 different commercial and open-source software.

We determined the best combinations of FGPT and ML models after different rounds of hyperparameter optimization and testing. Due to limited data, we iteratively evaluated each ML model with 20 random splits of the data in training and test sets.

The best results were obtained by an SVM model using a linear kernel and trained with ECFP-class FGPTs generated with Dragon software, yielding median absolute and relative retention index errors of 37.1 retention index units and 2%, respectively.

Previous studies have reported that similar molecular structures have a similar RT [6]. We focused on assessing whether these observations were echoed in

GC-MS RI prediction. First, the same metabolites with different TMS groups (e.g., leucine 1TMS and leucine 2TMS) share a common molecular structure. Based on the assumption that similar molecules differing from the same moieties (TMS groups) should share a similar RI difference, we used a simple linear regression among RI values of metabolites with 1 and 2, and 2 and 3 TMS groups.

This procedure was as accurate as the SVM model trained with certain FGPTs, although its use is limited to metabolites having at least one TMS-derivatized RI from a metabolite in the training set.

### Training set structural similarity influence on prediction performance

The structural similarity also influences the prediction performance when using ML-based models and is mainly modulated by the training set used. We observed that prediction accuracy increases when there is at least one similar metabolite in the training set—the more similar the structure is, the lower the prediction error is. This demonstrates that the structural similarity between the training and test set modulates the prediction performance. Based on these observations, we introduced a novel approach to estimate the expected prediction error range using a probabilistic model that considers the similarity between molecules—calculated using Tanimoto similarity scores—in the training and test set.

For instance, we observed that the probability of obtaining a prediction error lower than 1% is 48% but only when the structural similarity is between 90% to 100%. This probability is reduced to 25.8% if the similarity is between 80% and 90%.

### Application of the prediction model

We demonstrated the application of our prediction model in two GC-MS-based untargeted metabolomics cases: i) simulating a case where there are several putative candidates with similar mass or similar spectra, and ii) in a clinical untargeted metabolomics study of plasma samples from patients with ulcerative colitis. We showed the application of predicted RI values in metabolomics when there are multiple candidates that can match a monoisotopic mass or spectrum. In simulated cases, even with more than 4 putative candidates with the same molecular formula, predicted RI values enabled ranking the correct metabolite identity among the top three candidates (those with the lowest predicted-experimental RI error) in up to 50% of the cases. Also, we determined that using a 3% predicted-experimental RI error filtering threshold we reduced the number of putative candidates to nearly half, but at cost of retaining a large number of false

identities and filtering out a large number of true identities.

The application in real samples allowed us to compare the differences between experimental to reference and experimental to predicted RI errors (Fig. 1). In the clinical application, the model showed a good capacity at ranking the true metabolite identity among other candidates similar to the use of reference data or the use of MS spectral data.

### Conclusion

Collectively, our study provides a rationalized framework for machine learning-based retention time prediction of trimethylsilyl derivatives of metabolites in GC-MS. Implementation of predicted retention index values in untargeted metabolomics studies may be of special utility in cases where reference data or commercial standards are unavailable.

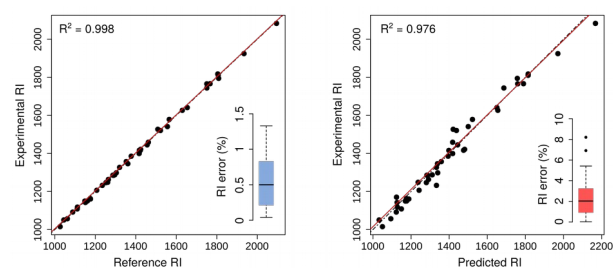


**Fig. 1.** Experimental vs reference RI (right) and experimental vs predicted RI (left) of the identified metabolites in the clinical trial.

### References

- [1] Domingo-Almenara X, et al. XCMS-MRM and METLIN-MRM: a cloud library and public resource for targeted analysis of small molecules. *Nat Methods* 2018;15:681–4. <https://doi.org/10.1038/s41592-018-0110-3>.
- [2] Kind T, et al. FiehnLib: Mass Spectral and Retention Index Libraries for Metabolomics Based on Quadrupole and Time-of-Flight Gas Chromatography/Mass Spectrometry. *Anal Chem* 2009;81:10038–48. <https://doi.org/10.1021/ac9019522>.
- [3] Vrzal T, Malečková M, Olšovská J. DeepRet: Deep learning-based gas chromatographic retention index predictor. *Anal Chim Acta* 2021;1147:64–71. <https://doi.org/10.1016/j.aca.2020.12.043>.
- [4] Matyushin DD, Buryak AK. Gas Chromatographic Retention Index Prediction Using Multimodal Machine Learning. *IEEE Access* 2020;8:223140–55. <https://doi.org/10.1109/ACCESS.2020.3045047>.
- [5] Dossin E, et al. Prediction Models of Retention Indices for Increased Confidence in Structural Elucidation during Complex Matrix Analysis: Application to Gas Chromatography Coupled with High-Resolution Mass Spectrometry. *Anal Chem* 2016;88:7539–47. <https://doi.org/10.1021/acs.analchem.6b00868>.
- [6] Wen Y, et al. Retention Index Prediction Using Quantitative Structure-Retention Relationships for Improving Structure Identification in Nontargeted Metabolomics. *Anal Chem* 2018;90:9434–40. <https://doi.org/10.1021/acs.analchem.8b02084>.

# Closed-Form Field Emission Current Model for Schottky Barrier Field-Effect Transistors

Christian Roemer, Ghader Darbandy, Mike Schwarz, Benjamín Iñíguez and Alexander Kloes

**Abstract**—In this document a set of physics-based compact equations is derived that is used to calculate the field emission current of Schottky barrier field-effect transistor devices. Therefore, this approach uses the Wentzel-Kramers-Brillouin approximation in order to calculate the charge carrier current that is tunneling through the Schottky barriers under the influence of a high electric field. The derived equations are also validated by using TCAD Sentaurus simulation results.

## I. INTRODUCTION

The DC characteristics of Schottky barrier field-effect transistors (SBFETs) as well as reconfigurable field-effect transistors (RFETs) based on Schottky barriers at their source and drain contacts are mostly dominated by the charge carrier injection through the device's Schottky barriers themselves. In case of devices with high Schottky barrier heights for electrons and holes, like shown in [1], [2], a simple consideration of only the thermionic emission (TE) current over the barriers is not sufficient in order to determine the device's drain current. Especially, in the device's on-state the high electric field over the Schottky barriers leads to a field emission (FE) current that consists of charge carriers tunneling through the barriers instead of overcoming them. This work shows the derivation of a closed-form equation that approximates the FE current of SBFET / RFET devices and is part of the compact model that we published in [3]. Additionally, a model fit to an SBFET device simulation demonstrates the functionality of the FE current calculation method. An example cross-section of an SBFET is shown in fig. 1.

## II. MODELLING APPROACH

Unlike the TE current, which is given by the charge carriers overcoming the Schottky barrier height, the FE current is given by those charge carriers tunneling through the barrier [3]. This type of current flow can only appear in case of a high electric field over the Schottky barrier that supports the current flow of a charge carrier type and leads to a strong band bending. This is demonstrated in fig. 2(a), which shows

a source-channel Schottky barrier of an SBFET in the on-state. The approximation for calculating the FE current uses a modified version of the Tsu-Esaki formula given by

$$J_{\text{FE}} = \frac{q\mu_n N_C}{k_b \vartheta} \cdot \int_{\mathcal{E}_{\min}}^{\mathcal{E}_0} f_m(\mathcal{E}) [1 - f_{\text{ch}}(\mathcal{E})] \times |E_x(\mathcal{E})| \cdot T(\vec{E}, \mathcal{E}) \cdot d\mathcal{E}, \quad (1)$$

where  $q$  is the elementary charge,  $\mu_n$  is the tunneling mobility of electrons,  $N_C$  is the density of states in the conduction band,  $k_b$  is the Boltzmann constant and  $\vartheta$  is the temperature [3], [4].  $\mathcal{E}$  is the energy from  $\mathcal{E}_{\min}$  which is the minimum conduction band energy in the channel to  $\mathcal{E}_0$  which is the maximum conduction band energy directly at the source-channel junction (at  $x = 0$  in fig. 2(a)). The right-hand side diagram in fig. 2(a) shows the components of the integral in (1), where the green line shows the product of the electric field in source-channel direction ( $E_x$ ) and the tunneling probability ( $T$ ) and the red line shows the product of the Fermi distribution for electrons ( $f_m$ ) in the source region, representing the number of electrons available for tunneling, and the Fermi distribution for holes in the channel region ( $1 - f_{\text{ch}}$ ), indicating unoccupied states the electrons can tunnel to [3]. The tunneling probability, which can be approximated by the Wentzel-Kramers-Brillouin approximation for triangular tunneling barrier shapes, given by

$$T(x) = \exp\left(-\frac{4}{3} \cdot \frac{\sqrt{2qm^*} \cdot (\Delta\Phi(x))^{3/2}}{\hbar \cdot |E_x(0)|}\right), \quad (2)$$

is used in this calculation, where  $\hbar$  is the reduced Planck's constant,  $m^*$  is the tunneling charge carrier mass and  $\Delta\Phi$  is the height of the barrier to be tunneled through by charge carriers [3], [4]. However, using (2) in (1) leads to an analytically unsolvable expression. Therefore, an approximation for (1) was introduced in [4] that approximates the product of the Fermi distributions with a Gaussian distribution and the product of the electric field and the tunneling probability with an exponential function, which results in

$$J_{\text{FE}} \approx \frac{q\mu_n N_C}{k_b \vartheta} \cdot \int_{\mathcal{E}_{\min}}^{\mathcal{E}_0} \frac{1}{4} \exp(-a(\mathcal{E} - E_f)^2) \times b \cdot \exp(-c(\mathcal{E}_0 - \mathcal{E})) \cdot d\mathcal{E}. \quad (3)$$

This project is funded by a grant from TH Mittelhessen University of Applied Sciences, Giessen, Germany. We acknowledge the support by Jens Trommer from NaMLab gGmbH, Dresden, Germany, André Heinzig from Chair for Nanoelectronics, TU Dresden, Dresden, Germany, Thomas Mikolajick from NaMLab gGmbH, Dresden, Germany and Chair for Nanoelectronics, TU Dresden, Dresden, Germany and Walter M. Weber from Institute of Solid State Electronics, TU Wien, Vienna, Austria.

Christian Roemer is with NanoP, TH Mittelhessen - University of Applied Sciences, Giessen, Germany and DEEEA, Universitat Rovira i Virgili, Tarragona, Spain (e-mail: christian.roemer@ei.thm.de). Ghader Darbandy, Mike Schwarz and Alexander Kloes are with NanoP, TH Mittelhessen - University of Applied Sciences, Giessen, Germany. Benjamín Iñíguez is with DEEEA, Universitat Rovira i Virgili, Tarragona, Spain.

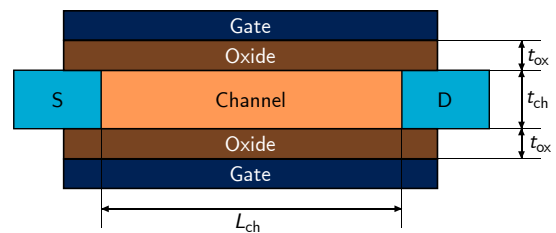


Figure 1. Schematic cross-section of an SBFET device that is used for the calculation and TCAD simulation.

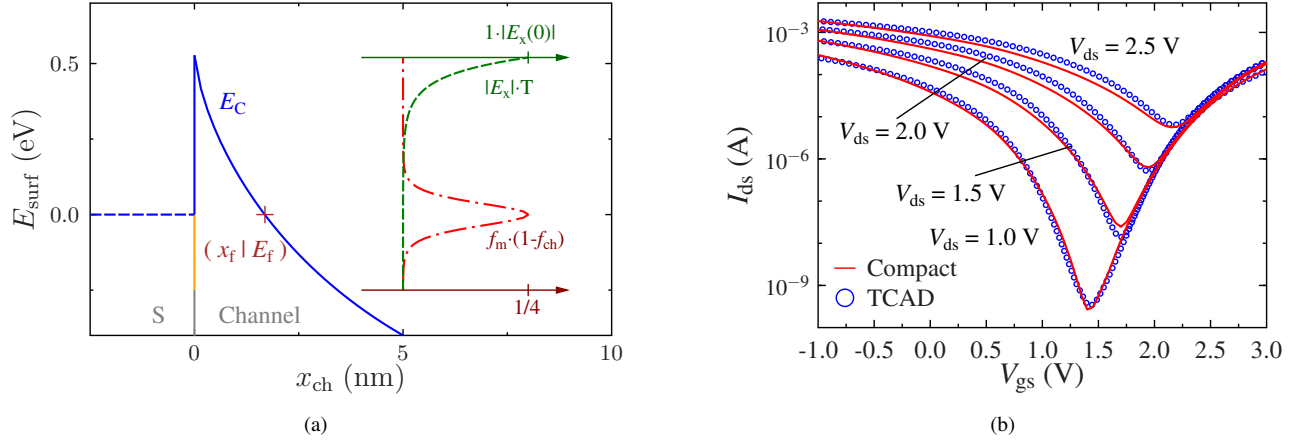


Figure 2. (a) shows the surface band diagram (at the channel-oxide surface) around the source-channel junction at  $x = 0$ . The blue solid line shows the conduction band energy and the blue dashed line shows the Fermi energy level in the metal. The right-hand side diagram shows the contributions to the integral of (1) depending on the energy. (b) shows the transfer characteristics in logarithmic scale of the model compared to a TCAD simulation. The blue dots represent the results of the TCAD simulation and the red lines are the compact model results.

The coefficients  $a$ ,  $b$  and  $c$  are energy independent and are reconstructed by using the equations (1), (2) and some auxiliary points. This leads to the expressions

$$a = \gamma_n \cdot \frac{\pi}{16 \cdot (k_b \vartheta)^2}, \quad (4)$$

$$b = E_x(0) \cdot T(0) \quad (5)$$

and

$$c = \ln \left( \frac{1}{b} \cdot E_x(x_f) \cdot T(x_f) \right) \cdot \frac{1}{\mathcal{E}(x_f) - \mathcal{E}(0)} \quad (6)$$

for the coefficients. The position  $x_f$  is shown in fig. 2(a) and is the position where the conduction band energy level gets lower than the Fermi energy level in the source region. This position is estimated to have the highest tunneling current density. The parameter  $\gamma_n$  is a fitting parameter, which shall compensate the difference between the Fermi function product from (1) and the Gaussian distribution from (3). With the given approximation the integral from (3) is now solvable. While the shown equations are used to calculate the FE current for electrons, it shall also be mentioned that the FE current for holes is calculated in a similar way by replacing the electron or conduction band related parameters ( $\mu_n$ ,  $N_C$  and  $\gamma_n$ ) to hole or valence band related parameters ( $\mu_p$ ,  $N_V$  and  $\gamma_p$ ). Some of the shown equations need the potential, energy band or electric field trace along the channel. In order to retrieve those values, a compact potential solution is used which is beyond the scope of this document, but can be found in [3].

### III. MODEL VERIFICATION

In order to verify the model equations, the calculated FE current is compared to the drain current of a simulated double-gate SBFET device, which is simulated by using TCAD Sentaurus [5]. The simulated device has a channel that consists of silicon with a length of  $L_{ch} = 40$  nm and a thickness of  $t_{ch} = 10$  nm. The gate oxide has a thickness of  $t_{ox} = 2$  nm and the gate material leads to a flatband-voltage of  $V_{fb} = 1$  V. The source and drain regions are made of nickel silicide leading to a Schottky barrier height for electrons of  $\Phi_{B,n} = 0.660$  V and  $\Phi_{B,p} = 0.495$  V for holes, which results in a total band-gap of  $E_{g,ch} = 1.155$  eV. The simulation and model results are

shown in fig. 2(b). While the TCAD simulation was done as a two-dimensional structure the resulting current is scaled to a channel width of  $W_{ch} = 1$   $\mu$ m.

The results in fig. 2(b) show the transfer characteristics for various drain voltages. The calculation is done with the compact model from [3], which consists of the FE current and TE current calculation. However, the given results are dominated by the FE current. An effect of the nearly equally high Schottky barriers for electrons and holes is the ambipolar device behavior. For increasing gate voltages the current increases, because of the FE current of electrons at the source-channel junction. In case of decreasing gate voltages, the current also increases, because of the FE current of holes at the drain-channel junction. In general, the results of the compact model show a good agreement to the TCAD simulation.

### IV. CONCLUSION

In this work a method of approximating the FE current calculation for SBFET and RFET devices was derived. Additionally, the FE current calculation has been validated by comparing the results to a TCAD simulation. The given equations are physics based and analytically solvable, which makes them straightforward usable in a compact model as demonstrated in [3].

### REFERENCES

- [1] A. Heinzig, S. Slesazek, F. Kreupl, T. Mikolajick, and W. M. Weber, "Reconfigurable silicon nanowire transistors," *Nano Letters*, vol. 12, no. 1, pp. 119–124, Dec. 2011.
- [2] W. Weber, A. Heinzig, J. Trommer, D. Martin, M. Grube, and T. Mikolajick, "Reconfigurable nanowire electronics – a review," *Solid-State Electronics*, vol. 102, pp. 12–24, Dec. 2014.
- [3] C. Roemer, G. Darbandy, M. Schwarz, J. Trommer, A. Heinzig, T. Mikolajick, W. M. Weber, B. Iniguez, and A. Kloes, "Uniform DC compact model for Schottky barrier and reconfigurable field-effect transistors," in *2021 IEEE Latin America Electron Devices Conference (LAEDC)*. IEEE, Apr. 2021.
- [4] M. Schwarz, T. Holtij, A. Kloes, and B. Iniguez, "Compact modeling solutions for short-channel SOI schottky barrier MOSFETs," *Solid-State Electronics*, vol. 82, pp. 86–98, Apr. 2013.
- [5] Synopsys Inc., *TCAD Sentaurus Device User Guide*, 2018, Version O-2018.06.

# Generic Scheme to Model the Schottky Barrier at the Drain Contact of Organic Transistors

Jakob Pruefer, Jakob Leise, Aristeidis Nikolaou, Ghader Darbandy, Benjamín Iñiguez, and Alexander Kloes

**Abstract**—We present a generic compact-modeling scheme to capture the influence of the Schottky barrier at the drain contact in organic transistors in compact dc models. We have derived an analytical equation for the voltage drop across the barrier, which is based on the drain current in the saturation regime of a barrier-less TFT. In order to implement the model, the voltage drop is implemented into the drain-source voltage of an existing charge-based compact dc model, but the generic scheme can be also applied to any compact dc model. Finally, the compact dc model is verified against the results of TCAD simulations of staggered organic TFTs with barrier heights ranging from 0 V to 0.39 V.

**Index Terms**—Schottky barrier, contact resistance, contact effects, short channel, organic thin-film transistor, compact modeling.

## I. INTRODUCTION

RESEARCH on organic transistors is working steadily on increasing the charge-carrier mobility of semiconductors and shortening the channel length to broaden the application range of them. Thereby, non-linear contact effects become more and more important [1], which are mainly caused by the Schottky barriers at the metal/semiconductor interfaces. However, many approaches model only the Schottky barrier at the source contact and neglect the drain barrier [2] to finally fit both emergent effects by the Schottky barriers with the model.

This work focuses on the influence of the Schottky barrier at the drain contact in organic TFTs on the current-voltage characteristics and develops a compact model in form of the voltage drop across the barrier. Therefore, the source-barrier height is assumed as zero to separate the influence of both Schottky barriers, although this is very unlikely in case of fabricated organic TFTs. In fact, the barriers at the source and drain contact have similar heights, and thus must be modeled simultaneously as in [5]. For verification, the compact dc model in [3] is used to fit TCAD simulations of staggered p-type organic TFTs.

## II. MODELING OF THE SCHOTTKY BARRIER

The Schottky barrier at the drain contact can be modeled as a diode operated in forward direction as illustrated in Fig. 1b. One well-known approach to model the diode current is

$$I_D = I_s \cdot \left( \exp \left( \frac{qV_{sb,d}}{\theta kT} \right) - 1 \right) \quad (1)$$

The project was funded by the German Federal Ministry of Education and Research ("SOMOFLEX", No. 13FH015IX6), EU H2020 RISE ("DOMINO", No. 645760), and the German Research Foundation (DFG) under the grant KL 1042/9-2 (SPP FFlexCom). We would like to thank Dr. Hagen Klauk from the Max Planck Institute for Solid State Research in Stuttgart, Germany, for many fruitful discussions and technical advice.

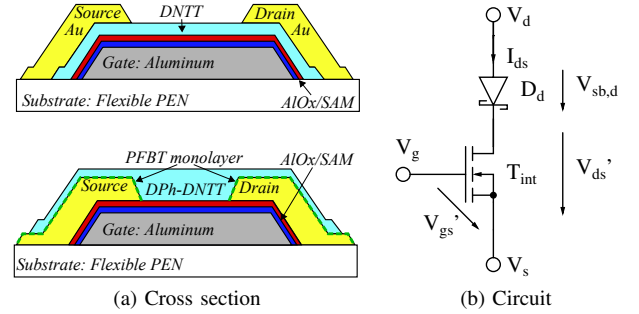


Fig. 1: (a) Cross sections of a staggered (top) and coplanar (bottom) architecture and (b) a circuit of an organic TFT in which the drain barrier is described by a diode in forward direction at the drain contact.

with the elementary charge  $q$ , the voltage drop across the barrier  $V_{sb,d}$ , the non-ideality factor of the diode  $\theta$ , the Boltzmann constant  $k$ , the temperature  $T$  and the reverse-bias saturation current  $I_s$ :

$$I_s = W_{ch} L_{inj} A^* T^2 \exp \left( -\frac{q\Phi_{B0}}{\eta kT} \right). \quad (2)$$

Here,  $W_{ch}$  is the channel width,  $\eta$  is the non-ideality factor of the reverse-bias saturation current, and  $A^* = 120 \text{ A}/(\text{cm}^2 \text{K}^2)$  is the effective Richardson constant. The injection length  $L_{inj}$  is in coplanar TFTs assumed to be identical to the thickness of the charge-carrier channel and in case of staggered devices it is identical to the characteristics length  $L_T$ .

The current of the diode equation  $I_D$  increases significantly above a certain voltage  $V_{sb,d}$ , which is known as the forward

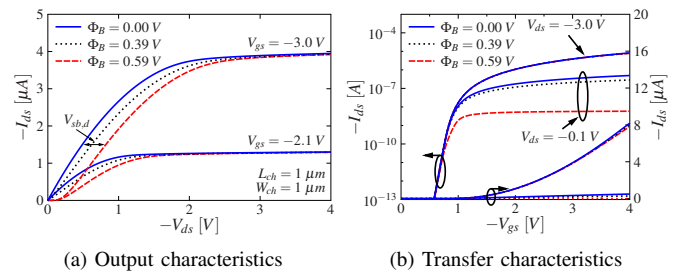


Fig. 2: Results of TCAD simulations illustrating the effect of the drain barrier on the output and transfer characteristics of a staggered p-channel TFT with a channel length and width of  $1 \mu\text{m}$  for three different barrier heights at the drain contact.



voltage  $V_F$ . If the drain-source voltage  $V_{ds}$  is greater than  $V_F$  (circuit in Fig. 1b), the voltage drop across the Schottky barrier  $V_{sb,d}$  saturates to approximately  $V_F$  and does not depend further on  $V_{ds}$ . If  $V_{ds} < V_F$ , the barrier is limiting the drain current of the organic TFT. The gate-source voltage  $V_{gs}$  is unaffected of the Schottky barrier at the drain/semiconductor interface.

Figure 2 confirms these considerations, where TCAD simulations are shown to illustrate the influence of the drain barrier on the output and transfer characteristics of a staggered organic TFT. Both figures, output and transfer characteristics, show that the drain current of the organic TFTs with different barrier heights at the drain contact are equal in the saturation regime, since  $V_{ds}$  is much higher as  $V_F$ . Thus, the voltage drop across the barrier  $V_{sb,d}$  in saturation regime can be calculated by equating the diode current  $I_D$  and the drain current of a barrier-less organic TFT  $I_{ds,bl}$ :

$$V_{sb,d,sat} = \frac{\theta kT}{q} \cdot \ln \left( \frac{I_{d,bl}}{I_{sb,d}} + 1 \right). \quad (3)$$

The drain current  $I_{ds,bl}$  must be calculated in deep saturation regime, e.g.  $V_{ds} = 5 \cdot (V_{gs} - V_T)$ . For this, any suitable model can be applied. In this work, we apply the compact dc model published in [3]. According to Fig. 2a, the drain-source voltage at which the voltage drop across the barrier saturates is larger than the drain-source voltage at which the drain current saturates. Therefore, the saturation condition for  $V_{sb,d}$  is defined with an additional fitting parameter  $w_{sat}$ :

$$V_{ds,sat,V_{sb,d}} = w_{sat} \cdot (V_{gs} - V_T). \quad (4)$$

In order to model all meaningful positive values of  $V_{ds}$ , the voltage drop across the barrier  $V_{sb,d}$  is assumed as a linear function of  $V_{ds}$  between  $V_{ds} = 0$  and  $V_{ds,sat,V_{sb,d}}$ . If  $V_{ds}$  is zero then the voltage drop across the barrier  $V_{sb,d}$  is also zero. Thus, the voltage drop across the barrier can be calculated as follows

$$V_{sb,d} = \begin{cases} V_{ds} \frac{V_{sb,d,sat}}{V_{ds,sat,V_{sb,d}}} & \text{for } 0 \leq V_{ds} < V_{ds,sat,V_{sb,d}} \\ V_{sb,d,sat} & \text{for } V_{ds} > V_{ds,sat,V_{sb,d}} \end{cases}. \quad (5)$$

To prevent numerical problems and to obtain an equation without case distinctions a smoothing function as in [4] is used:

$$V_{sb,d} = C \left( 1 - \frac{1}{B} \cdot \ln \left( 1 + \exp \left( A \left( 1 - \frac{x}{C} \right) \right) \right) \right), \quad (6)$$

$$x = V_{ds} \cdot \frac{V_{sb,d,sat}}{V_{ds,sat,V_{sb,d}}}, \quad A = 5,$$

$$B = \ln(1 + \exp(A)), \quad C = V_{sb,d,sat}.$$

Finally, the drain-source voltage  $V_{ds}$  of the applied compact dc model must be replaced by:

$$V_{ds,new} = V_{ds} - V_{sb,d}. \quad (7)$$

### III. RESULTS, VERIFICATION AND CONCLUSION

Figure 3 and 4 show the compact dc model in [3] extended with the voltage drop across the drain barrier  $V_{sb,d}$  fitted to current-voltage characteristics of organic TFTs with different

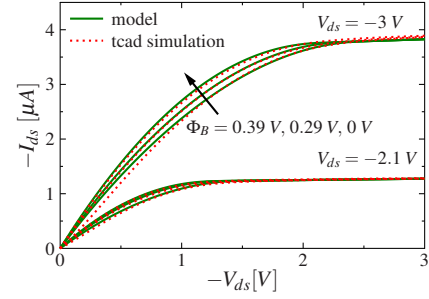


Fig. 3: Results of TCAD simulations illustrating the effect of the drain barrier on the output characteristics of a staggered p-channel TFT with a channel length and width of  $1 \mu\text{m}$  for three different drain-barrier heights.

barrier heights at the drain contact simulated with the TCAD software Sentaurus. The compact model is in good agreement with barrier heights up to 0.39 V, except at small drain-source voltages of organic TFTs with great barrier heights. Here, the simplified modeling of  $V_{sb,d}$  in the linear regime by a linear function of  $V_{ds}$  shows its disadvantages with small deviations. Nevertheless, the non-linearity in the linear regime of the

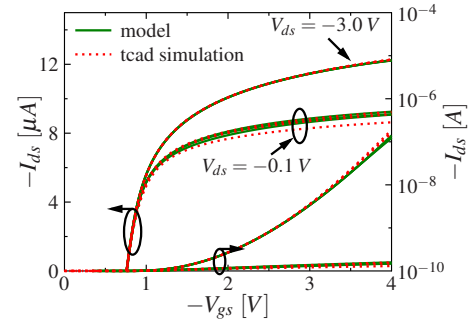


Fig. 4: Results of TCAD simulations illustrating the effect of the drain barrier on the transfer characteristics of a staggered p-channel TFT with a channel length and width of  $1 \mu\text{m}$  for three different drain-barrier heights.

output characteristics is mainly caused by the current injection over the source barrier, and thus the deviation of the drain barrier model is negligible.

### REFERENCES

- [1] A. Fischer et al., "Nonlinear Contact Effects in Staggered Thin-Film Transistors," *Phys. Rev. Applied*, vol. 8, no. 5, 054012, Nov 2017, doi: 10.1103/PhysRevApplied.8.054012.
- [2] A. Valletta et al., "Contact effects in high performance fully printed p-channel organic thin film transistors," *Applied Physics Letters*, vol. 99, no. 233309, Dec 2011, doi: 10.1063/1.3669701.
- [3] F. Hain, M. Graef, B. Iníguez and A. Kloes, "Charge based, continuous compact model for the channel current in organic thin-film transistors for all regions of operation," *Solid-State Electronics*, vol. 133, pp. 17–24, July 2017, doi: 10.1016/j.sse.2017.04.002
- [4] A. Kloes, "Analytische Modellierung mehrdimensionaler Effekte in Submikron-MOSFET's," Ph.D. dissertation, Technische Hochschule Darmstadt, 1997.
- [5] J. Prüfer, J. Leise, A. Nikolaou, J. W. Borchert, G. Darbandy, H. Klauk, B. Iniguez, T. Gneiting and A. Kloes, "Compact Modeling of Non-Linear Contact Effects in Short-Channel Coplanar and Staggered Organic Thin-Film Transistors," *IEEE Trans. Electron Devices*, accepted for publication in Jun 2021, doi: 10.1109/TED.2021.3088770.

# Iron-doped carbon dots as electrocatalysts for CO<sub>2</sub> reduction

Beatriu Domingo Tafalla<sup>a,\*</sup>, Joan Marc Bondia Pedra<sup>a,\*</sup>, Emilio Palomares<sup>a,\*,†</sup>

<sup>a</sup>Institute of Chemical Research of Catalonia (ICIQ), Avinguda del Països Catalans 16, 43007 Tarragona, Spain.

Tel: +34 977 920 200; E-mail: bdomingo@iciq.es

\*Universitat Rovira i Virgili (URV), N5- Edifici de Serveis Centrals Carrer Marcel·lí Domingo, 2-4-6, 43007- Tarragona

†Catalan Institution for Research and Advanced Studies (ICREA), Passeig de Lluís Companys 23, 08010 Barcelona, Spain.

†Université de Pau y Pays de l'Adour (UPPA), Avenue de l'Université, 64012 Pau, Francia

Teléfono: +33 5 59 40 70 00.

The conversion of CO<sub>2</sub> into valuable carbon products needs the development of Earth-abundant, stable and selective catalysts. Nitrogen-doped carbon dots (NCD), which can be further doped with metals in order to form M-N-C catalytically active centers, are promising candidates for the reduction of CO<sub>2</sub>. Herein, NCD are synthesized from urea and citric acid and are doped with iron. Although the indications of successful iron doping during and after the synthesis of NCD, the materials do not show catalytic activity in solution. On the other hand, bipyridine-Fe(III) functionalized NCD are the most promising synthesized catalysts for CO<sub>2</sub> reduction.

## Introduction

The electrochemical reduction of CO<sub>2</sub> (CO<sub>2</sub>RR) to useful carbon-containing fuels is a promising method to reduce the increased CO<sub>2</sub> levels attributed to human activity<sup>1</sup>. However, the stability of the CO<sub>2</sub> molecule requires active, selective and stable catalysts to decrease the overpotential and to avoid the hydrogen evolution reaction (HER), which is a side reaction<sup>1,2</sup>. Non-abundant metals such as Au, Ag, Pb and Sn primarily catalyze production of carbon monoxide (CO) or formate (HCOO<sup>-</sup>)<sup>3</sup>, while only Cu based catalysts produce C<sub>2</sub> hydrocarbons and oxygenates<sup>4</sup>. Thus, there is the need to develop low cost Earth-abundant catalysts with high Faraday Efficiency (FE) and current density as well as a high selectivity.

Carbon dots, with easy large-scale production, high chemical stability and excellent photo/electro properties have gained attention as promising candidates for the design of electrocatalysts<sup>5,6</sup>. Nitrogen doping of these materials breaks the electroneutrality and enhance the adsorption capacity of the CO<sub>2</sub> intermediate<sup>7</sup>. Moreover, nitrogen atoms can be used as ligands for metallic ions for the formation of M-N-C centers, which are proposed to be catalytic active sites, even with Earth abundant metals such as Fe, Co and Mn<sup>8</sup>.

In this work, the development of carbon-dot based electrocatalysts with M-N-C centers for the CO<sub>2</sub>RR is investigated. The nitrogen-doped carbon dots (NCD) are easily produced by hydrothermal synthesis methods and are further doped with metals in three different ways. The materials are characterized and their catalytic activity is assessed by means of cyclic voltammetry.

## Methods

NCD were synthesized by the hydrothermal method<sup>9</sup>. Urea and citric acid were dissolved in DMF in a Teflon lined autoclave and placed in the oven at 160-200 °C for

19 hours. These NCD were doped with iron following three pathways: 1) iron was added during the synthesis (Fe-NCD), 2) already synthesized NCD were dissolved in the presence of Fe<sup>3+</sup> salt, which complexed on the surface N-C centers of the NCD (psFe-NCD) and 3) already synthesized NCD were functionalized with a dicarboxy-bi-pyridine which functioned as the complexing centers of Fe<sup>3+</sup> (Py-Fe-NCD).

Cyclic voltammetry measurements of the metal-free and metal-doped NCD in solution were performed in DMF under Argon and CO<sub>2</sub> atmospheres. The three-electrode setup was used<sup>10</sup>.

## Results and discussion

NCD synthesized from urea and citric acid present two bands in the absorbance spectra, the  $\pi$ - $\pi^*$  band at 280-290 nm related to sp<sup>2</sup>-C bonds and the n- $\pi^*$  band at 340-360 nm attributed to surface states. These bands are shifted in energy when iron is introduced in the synthesis (Fig. 1A). NCD show an excitation dependent emission (Fig. 1B) which shape does not vary in the presence of a dopant. The Quantum Yield of the NCD (31 %) decreases with the addition of iron in the synthesis (11.5 %), and decreases more when the doping is done post-synthesis (8.9 %). Such phenomenon indicates the presence of iron into the structure and/or on the surface of the NCD, since iron is a fluorescence quencher. In the XRD profile, the graphite characteristic peak at 26.7 ° can be distinguished for non-doped NCD and psFe-NCD, whereas it is wide for Fe-NCD which also show other peaks probably coming from iron oxides phases.

The cyclic voltammograms of the synthesized catalysts measured in solution expose that psFe-NCD present very slight current increase with respect to the blank under CO<sub>2</sub> atmosphere (Fig. 2A). Non-doped NCD and Fe-NCD are not shown but did not have any catalytic activity. Only the catalyst Py-Fe-NCD shows a catalytic wave under CO<sub>2</sub> atmosphere (Fig. 2B).

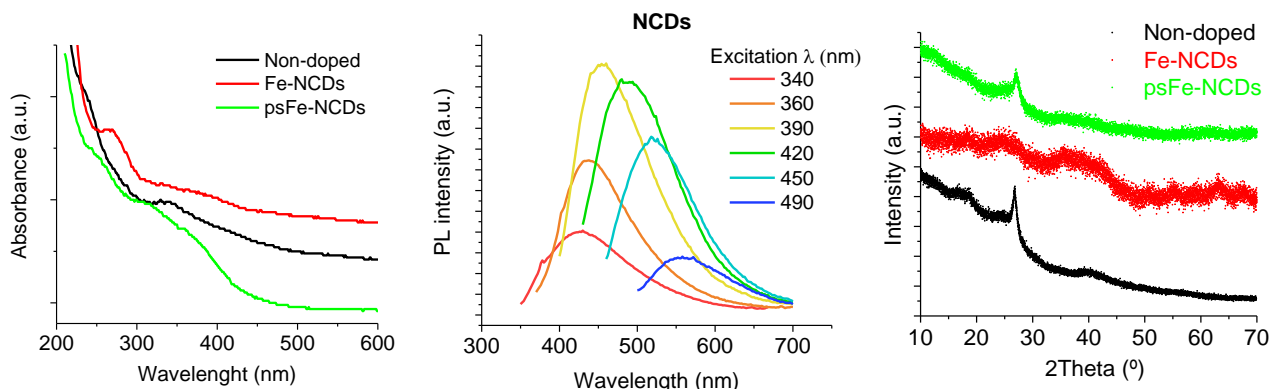


Figure 1. Characterization of Non-doped, Fe-doped and psFe-doped NCDs. Absorbance spectra (A), emission spectra of non-doped NCD (B) and X-ray diffraction profile (C).

Although there is indication that iron has been incorporated into Fe-NCD and psFe-NCD, due to the lower QY with respect to non-doped NCD, no catalytic activity is detected. The fact that these catalysts are not fully soluble in the electrolyte can account for these results. In order to overcome this difficulty, the catalyst should be measured as an ink deposited on the electrode surface. On the other hand, Py-Fe-NCD are promising materials but should be further studied in order to determine whether the catalytic wave is caused by the

NCD functionalized with the bipyridine-Fe(III) complex or by unbound bipyridine-Fe(III) complex in solution.

In conclusion, NCD are potential low-cost synthesis materials with versatile characteristics which make them suitable for obtaining Earth-abundant metal-doped catalysts for CO<sub>2</sub> reduction. However, further studies are ongoing to determine their catalytic activity as a function of the size and the ligand coverage.

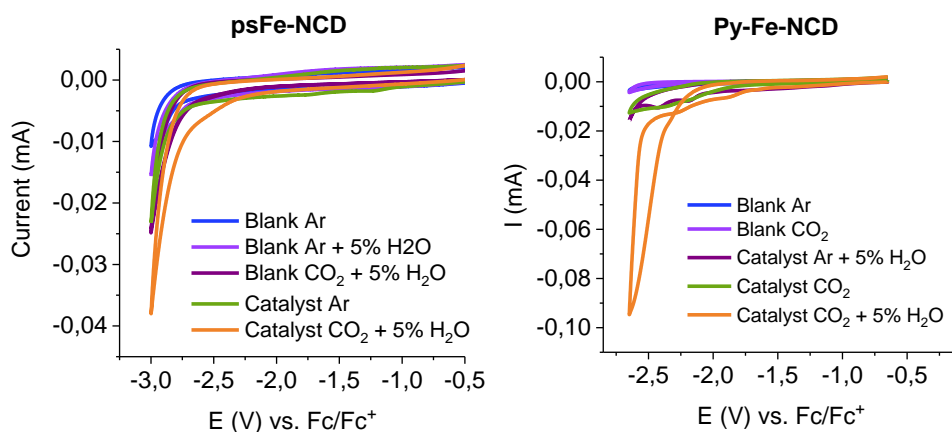


Figure 2. Cyclic voltammograms of psFe-NCDs and Py-Fe-NCDs dissolved in DMF 0.1 M TBAF<sub>6</sub>P.

## Bibliography

- Son, J., Song, D., Lee, K. R. & Han, J. I. Electrochemical reduction of CO<sub>2</sub> on Ag/MnO<sub>2</sub> binary catalyst. *J. Environ. Chem. Eng.* **7**, 8–11 (2019).
- Jia, C., Dastafkan, K., Ren, W., Yang, W. & Zhao, C. Carbon-based catalysts for electrochemical CO<sub>2</sub> reduction. *Sustain. Energy Fuels* **3**, 2890–2906 (2019).
- Hori, Y., Wakebe, H. H. I., Tsukamoto, T. & Koga, O. Electrocatalytic process of CO selectivity in electrochemical reduction of CO<sub>2</sub> at metal electrodes in aqueous media. *Electrochim. Acta* **39**, 1833–1839 (1994).
- Kuhl, K. P., Cave, E. R., Abram, D. N. & Jaramillo, T. F. New insights into the electrochemical reduction of carbon dioxide on metallic copper surfaces. *Energy Environ. Sci.* **5**, 7050–7059 (2012).
- Xu, X. *et al.* Electrophoretic analysis and purification of fluorescent single-walled carbon nanotube fragments. *J. Am. Chem. Soc.* **126**, 12736–12737 (2004).
- Gao, J., Zhu, M., Huang, H., Liu, Y. & Kang, Z. Advances, challenges and promises of carbon dots. *Inorg. Chem. Front.* **4**, 1963–1986 (2017).
- Wu, J. *et al.* Achieving Highly Efficient, Selective, and Stable CO<sub>2</sub> Reduction on Nitrogen-Doped Carbon Nanotubes. 5364–5371 (2015).
- Ju, W. *et al.* Understanding activity and selectivity of metal-nitrogen-doped carbon catalysts for electrochemical reduction of CO<sub>2</sub>. *Nat. Commun.* **8**, 1–9 (2017).
- Strauss, V., Wang, H., Delacroix, S., Ledendecker, M. & Wessig, P. Carbon nanodots revised: The thermal citric acid/urea reaction. *Chem. Sci.* **11**, 8256–8266 (2020).
- Chen, S. 2 - Practical Electrochemical Cells. in *Handbook of Electrochemistry* (ed. Zoski, C. G.) 33–56 (Elsevier, 2007). doi:https://doi.org/10.1016/B978-044451958-0.50003-3.



# Automated data analysis workflow for GCxGC-TOF-MS measurements

Maria Llambrich<sup>1,2</sup>, Raquel Cumeras<sup>1,2,3</sup>, Jesús Brezmes<sup>1,2</sup>

<sup>1</sup> Metabolomics Interdisciplinary Group MiL@b, Metabolomics Platform, Department of Electrical Electronic Engineering and Automation, Universitat Rovira i Virgili (URV), IISPV, CERCA, 43007 Tarragona, Spain; phone 977559700; fax 977 55 96 99; [maria.llambrich@urv.cat](mailto:maria.llambrich@urv.cat); [raquel.cumeras@urv.cat](mailto:raquel.cumeras@urv.cat); [jesus.brezmes@urv.cat](mailto:jesus.brezmes@urv.cat)

<sup>2</sup> Biomedical Research Centre, Diabetes and Associated Metabolic Disorders (CIBERDEM), ISCIII, Madrid, Spain

<sup>3</sup> Fiehn Lab, NIH West Coast Metabolomics Center, Genome Center, University of California Davis, Davis, CA, USA

## Abstract

Comprehensive gas chromatography is very well suited for the measurement of complex matrices, such those found in metabolomics. However, the high dimensionality of the raw data obtained makes the analysis and processing difficult to use in an automated way. Here we present an open-source workflow for GCxGC data which includes peak detection and identification using public databases. We identified 3 times more peaks compared to the golden standard commercial software. Moreover, 88.6% of the peaks found by the commercial software are present in our workflow too.

## 1. Introduction

Metabolomics is emerging as a potential tool for diagnosis, characterizing part of the compounds present in a living organism. It is a powerful tool to assess changes in key metabolic pathways which are linked with diseases. The metabolome is formed by small mass compounds present on the human body, particularly on biofluids such as blood, urine, feces or breath. These metabolites are detectable by diverse techniques but the most used are gas-chromatography or liquid-chromatography linked to mass spectrometry (GC/LC-MS). Chromatography allows the separation and characterization of individual compounds in complex samples, whereas mass spectrometry helps in the identification of this compounds [1].

Comprehensive gas chromatography (GCxGC-MS) consists of two columns connected in a serial configuration where a modulator transfers the sample portions on the first column to the second one. Its key advantages are increased peak capacity, increased resolution and increased sensitivity: all highly desirable for simultaneous detection and identification of compounds in complex matrices [2]. Using a non-polar first dimension, analytes are separated according to boiling point and volatility. As the second-dimension separation is fast, it is carried out under essentially isothermal conditions with little influence from sample volatility, so the separation is governed by the specific analyte interactions with the stationary phase.

GCxGC-MS data analysis is difficult and time-consuming due to the quantity and complexity of transforming the 3D raw data into chemical information. A typical workflow includes: acquiring data, correct artifacts, detect and identify chemical peaks, and statistical analysis of the datasets [3].

One of the bottlenecks on using this technique is the computer software automation process. Nowadays the huge quantity of data obtained on each measurement are only possible to analyze using commercial software from vendors which are protected and do not allow to automate the entire process. With this purpose, we are developing an automated workflow for an automated complete analysis of GCxGC-MS data in open-source code.

## 2. Methodology

### 2.1 Sample analysis

A set of 10 samples from essential oils was analyzed using a 7890 gas chromatogram from Agilent coupled to a Pegasus IV TOF/MS from Leco using a HP5 capillary column (30m × 0.32mm × 0.25mm) and a Rxi-17Si capillary column (1.5m × 0.15mm × 0.15mm). Analyses were performed using headspace into a splitless with helium constant flow of 1 mL·min<sup>-1</sup>. The GC oven temperature was held at 50°C for 1 min, then raised to 120°C at a rate of 3C/min, then at a rate of 15°C/min until 185°C. The second oven was set at 5°C. The mass spectrometer acquired m/z ratios between 35 and 500Da at 10 Hz and an electron impact energy of 70 eV.

### 2.2 Data processing

Raw data from the commercial system is transformed to CDF format, which can be imported to the R statistics platform. Chromatographic data requires several pre-processing steps. Based on Cain et al. [4] we had implemented in the workflow the following steps:

- i) data centering – mean values are adjusted to 0,
- ii) logarithmic transformation – increases the small signals.

The structure of Comprehensive gas chromatography data is three dimensional. The first dimension is related to retention time from the first column (retention time 1D), retention time for the second column (retention time

2D) is the second dimension and the intensity for each  $m/z$  value is the third dimension. In Figure 1 it is shown the total ion chromatogram plot of one of the samples analyzed. Pre-processing steps are applied at each  $m/z$  value separately, working with data as two-dimensional corresponding to retention time from first and second column.

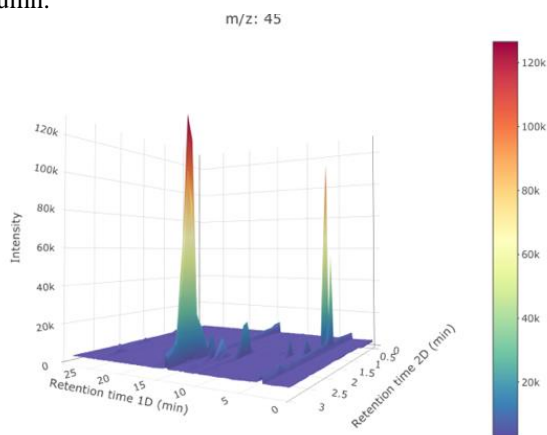


**Figure 1.** Three-dimensional chromatogram plots of Peppermint essential oil sample analyzed with GCxGC-TOF. Results with the workflow developed showing the results for the  $m/z$  45.

Then automatic peak detection is performed, also known as peak picking. As we have tridimensional data, we apply the watershed algorithm [5] for each  $m/z$  value individually. After this, peaks are grouped by the apex position (peak maximum). Deconvolution is applied for peaks that are close - peaks in the same point of retention time 1D and adjacent time points of retention time 2D- using multivariate curve resolution (MCR) implemented in the independent component analysis package developed previously by the group for GCxGC-MS [6]. At last, we obtain a list containing the peak number, retention time 1, retention time 2, intensity and spectra. Identification of the peaks is done comparing the spectra to a reference spectrum from different mass spectrometry libraries using the cosines similarity index [7]. The public libraries used were BinBase (<https://binvestigate.fiehnlab.ucdavis.edu/>), MONA (<https://massbank.us>), and GOLM (<http://gmd.mpimp-golm.mpg.de>).

### 3. Preliminary results

We have analyzed and processed 10 samples of essential oils, each one having one known essential oil. With our workflow, we have detected an average of 247 (s.d. 41.4) peaks per sample. To validate the method, we checked which of these peaks are detected using the commercial software ChromaTOF from LECO GCxGC-MS instrument. The 88.6% (s.d. 4.6) of peaks detected by the commercial software are detected with our software. In our workflow we are obtaining more peaks compared to the commercial software (see Table 1). There are some steps that are not yet implemented, such as removing

duplicate peaks. We used a cut-off for the identification of a similarity index higher than 80%, which was agreed by the 97.6% (s.d. 0.7) of the peaks.

Sample	Peaks detected using our workflow	Peaks detected using commercial software	% shared
Espliego	235	71	84.5
Laurel	250	84	90.3
Lavander	309	92	85.2
Lavandino	241	68	91.9
Coriander	160	47	78.3
Rosemary	287	96	86.5
Peppermint	213	75	90.3
Eucalyptus	218	70	84.3
PetitGrain	200	56	82.3
Caraway	207	68	94.4

**Table 1.** Results from peak detection on 10 samples using our workflow and a commercial software.

### 4. Conclusions

Comprehensive gas-chromatography is a promising technique in the metabolomics field. With the workflow we have developed it will be easily implemented in routine analysis. We continue working on the workflow to obtain more accurate results and automatizing all the process.

### Acknowledgments

This work has been supported by Spanish MINECO project Total2DChrom [RTI2018-098577-B-C21]. RC is thankful for her EU MSCA-project COLOVOC [798038]. MLL is thankful for her graduate fellowship from URV PMF-PIPF program (ref. 2019PMF-PIPF-37). We acknowledge AGAUR consolidated group grant (2017SGR1119). IISPV is a member of the CERCA Programme/Generalitat de Catalunya.

### References

- [1] W. Hon Kit Cheung and R. Cumeras, "Basics Of Gas Chromatography Mass Spectrometry System," in Volatile organic compound analysis in biomedical diagnosis applications, Apple Academic Press, 2020, pp. 31–50.
- [2] P. Vazquez-Roig and Y. Pico, "Gas chromatography and mass spectroscopy techniques for the detection of chemical contaminants and residues in foods," in Chemical Contaminants and Residues in Food, Elsevier Inc., 2012, pp. 17–61.
- [3] S. E. Reichenbach, "Chapter 4 Data Acquisition, Visualization, and Analysis," Comprehensive Analytical Chemistry, vol. 55. Elsevier, pp. 77–106, Jan. 2009.
- [4] C. N. Cain, S. Schöneich, and R. E. Synovec, "Development of an enhanced total ion current chromatogram algorithm to improve untargeted peak detection," Anal. Chem., vol. 92, no. 16, pp. 11365–11373, Aug. 2020, doi: 10.1021/acs.analchem.0c02136.
- [5] S. Beucher, "Watershed, Hierarchical Segmentation and Waterfall Algorithm," 1994, pp. 69–76.
- [6] X. Domingo-Almenara, A. Perera, N. Ramírez, and J. Brezmes, "Automated resolution of chromatographic signals by independent component analysis-orthogonal signal deconvolution in comprehensive gas chromatography/mass spectrometry-based metabolomics," Comput. Methods Programs Biomed., vol. 130, pp. 135–141, 2016, doi: 10.1016/j.cmpb.2016.03.007.
- [7] K. X. Wan, I. Vidavsky, and M. L. Gross, "Comparing similar spectra: From similarity index to spectral contrast angle," J. Am. Soc. Mass Spectrom., vol. 13, no. 1, pp. 85–88, 2002.

# Grid-connected LCL Filter Design with Different Damping Methods

S. Valedsaravi\*, A. El Aroudi, J. A. Barrado-Rodrigo, M. Hamzeh, A. Cid-Pastor, and L. Martinez-Salamero  
\*seyedamin.valedsaravi@urv.cat,

**Abstract**—Damping is necessary in grid-connected converters with LCL filters to avoid their destabilizing resonant behavior. This paper presents a novel damping method for a grid-connected inverter with an LCL filter. This damping technique consists of inserting a AC-DC converter acting as a Loss Free Resistor (LFR) in parallel with the filter capacitor leading to the same stabilizing/damping effects as with the passive resistor and the capacitor current feedback. The stability analysis of the closed loop system with the previous damping techniques is performed. The theoretical results are validated by numerical simulations performed in PSIM<sup>®</sup> software.

**Index Terms**—LCL filter, grid-connected, active damping, passive damping, loss free resistor, stabilization

## I. INTRODUCTION

The use of power electronic converters integrated with renewable energy sources is extensively increasing recently. Due to intermittent nature of these sources, e.g. wind and solar, it is necessary to have power electronic converters as interfaces to control the electrical variables. One of the most used power converters in this kind of applications is the single phase DC-AC inverter with two switches. Switching action in these inverters can lead to undesired harmonic content in the current injected to the grid. To mitigate this problem, an L, LC or LCL filter are used. LCL filters, known as third-order low pass filters, have higher attenuation and lower size than L and LC filters. The only disadvantage of LCL filters is their resonant behaviour which can give rise to instability and poor performances. Passive and active damping methods can be employed in order to overcome this disadvantage [1].

In this paper damping and stabilization of a grid connected LCL filter is considered. A novel damping technique is used to stabilize the LCL filter dynamics. The rest of this paper is organized as follows. In section II, the system description is presented. Section III is devoted to designing of an Active Damping (AD) technique based on emulating the passive resistor by an LFR [2] is tested also leading to the same stabilizing effect. Concluding remarks are drawn in section IV.

## II. SYSTEM DESCRIPTION AND MODELING

### A. System description

Fig. 1 shows the single-phase configuration of the system studied in this paper. It consists of a single half-bridge grid-connected voltage source converter (VSC) with an LCL filter under a PI controller for the grid current to be in phase with the grid voltage. It can also be considered as a building block for constructing a multi-phase VSC inverter. The DC side consists of two identical regulated voltage sources each with

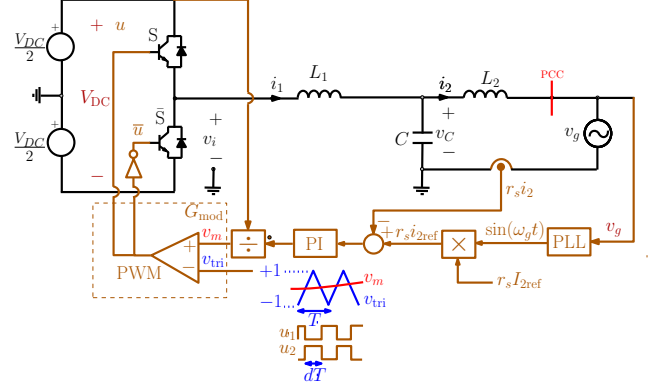


Fig. 1. Single-phase configuration of grid-connected LCL filter with grid-side current control technique through PI controller.

a voltage  $V_{DC}/2$  both referred to a midpoint considered here as the voltage reference node. It should be noted that each switch tolerate  $V_{DC}/2$  V. The LCL filter is used limit current harmonic pollution at the point of common coupling (PCC) which should be below 5% according to the IEEE standard 519-2014 [3].

## III. DIFFERENT DAMPING DESIGN METHODS AND THEIR VALIDATION BY NUMERICAL SIMULATIONS

The magnitude of the frequency response of the ideal LCL filter at the resonant frequency is high which can induce instability. Many studies have been done to stabilize such LCL filters by eliminating their resonant peaks. Roughly speaking, based on a literature survey, two practical techniques including passive damping and active damping based on capacitor current feedback can be used for compensation. In both of them the stabilization consists of introducing damping effects into the system. The innovative method of this article will be investigated in the following subsection [4], [5].

### A. Active damping based on connecting a power converter acting as a loss free resistor

The damping technique proposed in this paper is to utilize a power converter in parallel with the LCL filter capacitor. The idea is to take advantage of the fact that this converter will always coexist with the inverter in a microgrid. For instance, this converter can be used for battery charging. Fig. 2 shows the circuit diagram of the LCL filter with LFR-based converter used for damping. This converter has different stages. First, the filter capacitor voltage is rectified through a diode bridge.

Second, a boost converter topology is utilized in which the inductance of the inductor  $L_{lfr}$  is 1 mH. Finally, an LC low-pass filter is used to smooth the current injected into the battery. The values of  $L_f$  and  $C_f$  are selected as 1  $\mu$ H and 1  $\mu$ F. The LFR-based converter switching frequency is 160 kHz. It is worth noting that the parameters should be selected to guarantee the stability of the LFR. Design-rules for guarantee stability of an LFR are widely available in the literature [6]. Whenever the stability of the LFR used for damping is satisfied, its damping effect on the converter is the same as the one of a resistor. For simplicity an ideal LFR is considered in this paper. An LFR with losses would also have the same damping effect on the inverter. Fig. 3 shows the voltage and current at the input port of the LFR converter. It can be seen that the voltage and current are in phase hence emulating a resistor at this port. The control system was designed in such a way that the current  $i_{lfr}$  at the input port of the converter is proportional to the input port voltage  $v_{lfr}$ . The proportionality factor is  $R_d = 290.4 \Omega$  which is the same value for a passive damping method. The power processed by this stabilizer is related to the value of LFR resistor, which is 5% as in the passive damping method. However, with this damping method, this power is not lost and can be used for supplying non critical loads, charging batteries or can even be redirected to the grid. The battery charge current can be controlled by adding an external control loop. Fig. 4 shows

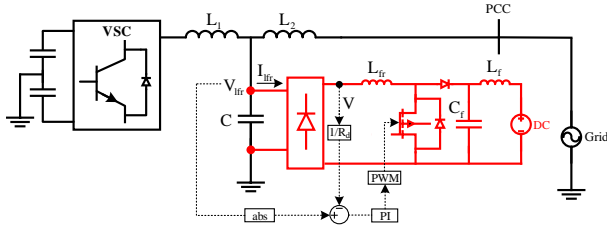


Fig. 2. Block diagram of the LCL filter with a LFR used as a damper.

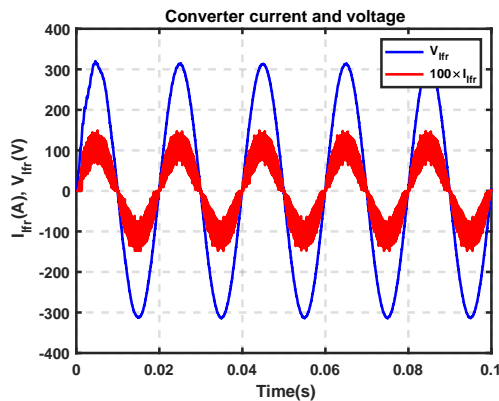


Fig. 3. The input voltage and current at the input port of the LFR acting as an AD.

the effect of different damping methods to the grid-connected

inverter with an LCL filter under a PI control. At  $t = 0.02$  s, all the damping techniques are disconnected from the system; thereby leading to instability. Then, they are activated again at  $t = 0.08$  s all resulting in stabilizing the inverter.

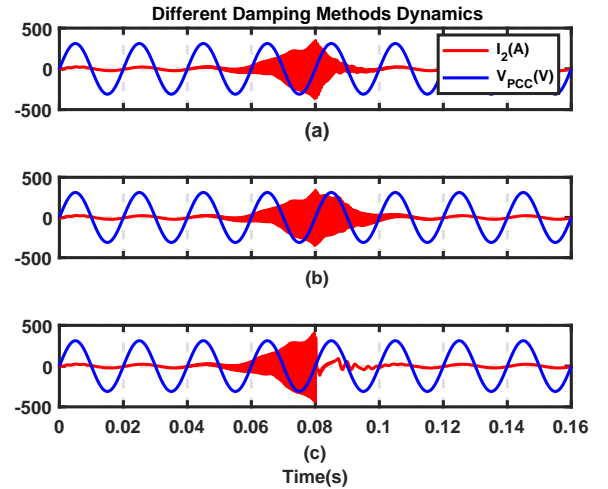


Fig. 4. Damping is disconnected in  $t \in [0.02, 0.08]$  s. (a) Passive damping based on the insertion of a parallel resistor. (b) Active damping based on capacitor current feedback. (c) Active damping based on connecting a power converter acting as an LFR.

#### IV. CONCLUSIONS

In this paper damping and stabilization of a grid connected LCL filter have been addressed. The technique consists of emulating the damping effect of the resistor by a DC-DC boost converter acting as a Loss Free Resistor (LFR). All the damping techniques are able to stabilize the system but with the novel damping technique, based on the LFR, the processed power can be utilized in microgrids for charging batteries while stabilizing the DC link voltage and DC loads or providing ancillary services to the main grid.

#### REFERENCES

- [1] M. Liserre, F. Blaabjerg, and S. Hansen, "Design and control of an LCL-filter-based three-phase active rectifier," *IEEE Transactions on Industry Applications*, vol. 41, no. 5, pp. 1281–1291, 2005.
- [2] A. Cid-Pastor, L. Martinez-Salamero, A. El Aroudi, R. Giral, J. Calvente, and R. Leyva, "Synthesis of loss-free resistors based on sliding-mode control and its applications in power processing," *Control Engineering Practice*, vol. 21, no. 5, pp. 689–699, 2013.
- [3] "IEEE recommended practice and requirements for harmonic control in electric power systems," *IEEE Std 519-2014 (Revision of IEEE Std 519-1992)*, pp. 1–29, 2014.
- [4] Q. Liu, L. Peng, Y. Kang, S. Tang, D. Wu, and Y. Qi, "A novel design and optimization method of an LCL filter for a shunt active power filter," *IEEE Transactions on Industrial Electronics*, vol. 61, no. 8, pp. 4000–4010, 2014.
- [5] S. Jayalath and M. Hanif, "Generalized LCL-filter design algorithm for grid-connected voltage-source inverter," *IEEE Transactions on Industrial Electronics*, vol. 64, no. 3, pp. 1905–1915, 2017.
- [6] R. Erickson and D. Maksimovic, *Fundamentals of Power Electronics*. Online access with purchase: Springer, Springer US, 2001.



# Synthesis conditions optimization of zinc oxide (ZnO) hierarchical nanostructures for gas sensing applications

Shuja Bashir Malik, Eduard Llobet Valero

MINOS, DEEEA, Universitat Rovira i Virgili, Països Catalans 26, 43007 Tarragona, Spain  
[shujabashir.malik@urv.cat](mailto:shujabashir.malik@urv.cat), [eduard.llobet@urv.cat](mailto:eduard.llobet@urv.cat)

## Abstract

ZnO nanostructures with floral morphologies were synthesized using hydrothermal synthesis at 150°C. The powdered samples were characterized for structural and morphological properties by X-ray diffraction (XRD) and Field Emission Scanning Electron Microscopy (FESEM) respectively. XRD studies confirmed the formation of hexagonal wurtzite structure of ZnO. The average crystallite size of the prepared nanopillars and nanoflowers were found to be 25 nm and 24 nm respectively. FESEM confirmed the formation of two floral structures. Assemblies of 2 - 3.5  $\mu\text{m}$  nanopillars are formed at longer reaction time while as floral structures ( $\sim 4 \mu\text{m}$ ) with petals are formed at short reaction time.

Keywords: Hydrothermal synthesis, gas sensing, hierarchical nanostructures

## 1. Introduction

Rampant use of fossil fuels for automobiles, electricity generation and industries lead to tremendous emission of greenhouse gases which are responsible for global warming [1]. Emission of hazardous gases by burning fossil fuel has led to a drastic increase in air pollution. The pollutants are toxic gases and volatile organic compounds (VOCs) which lead to major health problems [2]. Development of sensors for detection and monitoring of these pollutants is a highly critical area of research. Owing to their low cost, high stability, small size, and the suitability to detect both reducing and oxidizing gases [3], metal oxide semiconductor (MOS) gas sensors are being widely used. Among all the MOS, zinc oxide (ZnO) is highly desirable for its unique properties like non-toxicity, good optical properties, stability, and wide band gap (3.37 eV) at room temperature [4]. Keeping in view these distinctive properties of ZnO, it was chosen as a candidate for gas sensing applications.

In this work, we report the synthesis of ZnO hierarchical nanostructure growth by facile hydrothermal method at low temperature (150°C).

Nanoflowers were synthesized at short reaction times while as nano pillar assemblies were synthesized at higher reaction times. It was observed that the growth of the nanostructures is dependent on various factors like precursor concentration, reaction temperature, reaction time and pH. Several synthesis reactions were checked to examine the reproducibility of the reaction method and to optimize the synthesis conditions of the desired nanostructures.

## 2. Results

The crystal structure of the as-synthesized ZnO nanostructures was analysed by XRD as shown in Figure 1. The diffraction patterns are indexed to hexagonal wurtzite ZnO phase JCPDS card no. 01-075-1526. The crystal structure matches the space group of P63mc with lattice constant  $a = 0.3241 \text{ nm}$  and  $c = 0.5195 \text{ nm}$  for nanopillars and  $a = 0.3239 \text{ nm}$  and  $c = 0.5188 \text{ nm}$  for nano flowers. No characteristic peaks from other phases or impurities were observed indicating high purity of the prepared samples. Also, the strong and sharp peaks indicate high crystallinity of the prepared samples. The average crystallite sizes of nano pillars and nano flowers calculated by Scherer's formula are 25 nm and 24 nm respectively. Figure 2 and Figure 3 show FESEM images of as prepared ZnO nano pillar assemblies and ZnO nanoflower assemblies. Nanoflowers with an average size of  $\sim 4 \mu\text{m}$  were synthesized at lower reaction times while as nano pillar assemblies with an average size of  $\sim 3.5 \mu\text{m}$  were obtained at higher reaction times. The pillar assemblies are clusters of more than a dozen tapered hexagonal prism like ZnO nanorods with an average size of  $\sim 900 \text{ nm}$ . Figure 4 shows the FESEM image of disintegrated nano pillar assemblies after 1 minute sonication. However, the nanoflowers retain the shape after sonication. As can be seen from the FESEM images (Figure 2), the nanoflowers have many hollow structures and pores. The petals of the nanoflowers are rough which can be attributed to the clustering of the nanosized ZnO particles.

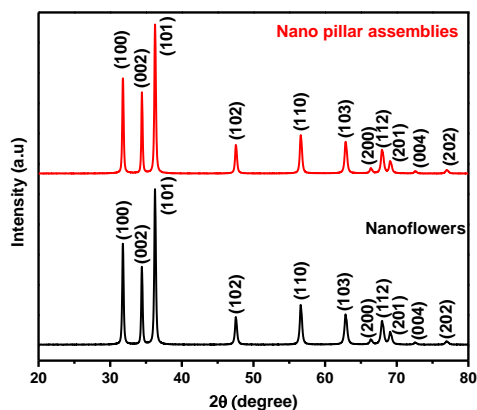


**Figure 1:** XRD patterns of as-prepared ZnO nanopillar assemblies and ZnO nanoflowers.

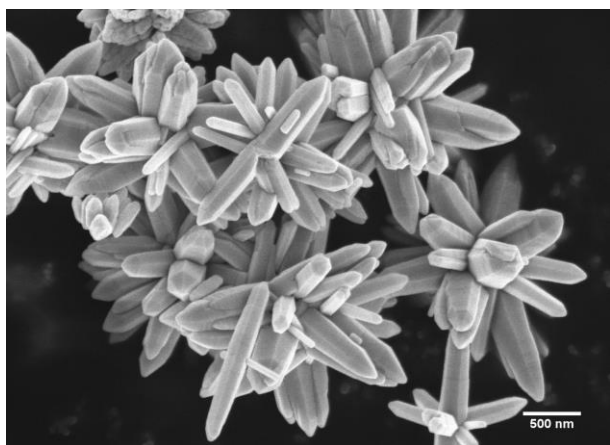


**Figure 2:** FESEM image of as prepared ZnO nano pillar assemblies

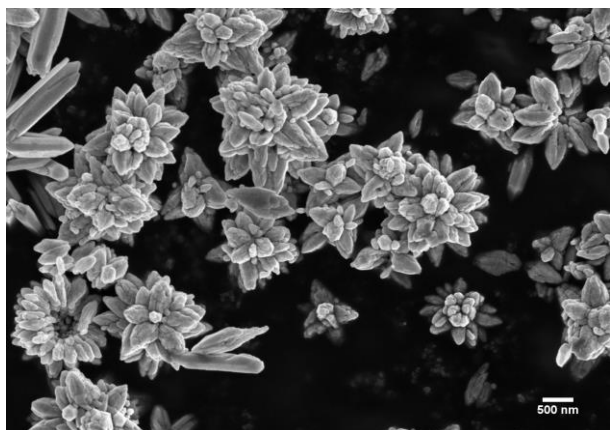


**Figure 3:** FESEM image of as prepared ZnO nano flower assemblies

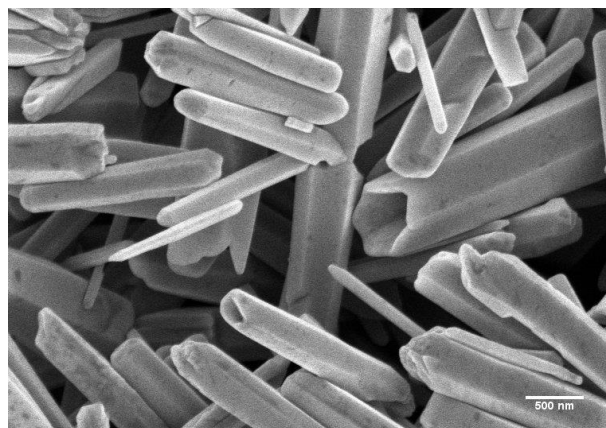


**Figure 4:** FESEM image of disintegrated nano pillar assemblies after 1 minute sonication.

### 3. Conclusions

Desired hierarchical ZnO nanostructures were successfully synthesized with great reproducibility using a facile one-pot hydrothermal synthesis. This work will be continued further to study the gas sensing properties of the pure and doped ZnO hierarchical nanostructures.

### 4. Acknowledgements

This project has received funding under Martí-Franquès Research grants Programme, Doctoral grants – 2019, (2019PMF-PIPF-14).

### References

- [1] Sitch, S., Brovkin, V., von Bloh, W., van Vuuren, D., Eickhout, B., and Ganopolski, A. (2005), Impacts of future land cover changes on atmospheric CO<sub>2</sub> and climate, *Global Biogeochem. Cycles*, 19, GB2013
- [2] M.J.S. Spencer, Gas sensing applications of 1D-nanostructured zinc oxide: insights from density functional theory calculations, *Prog. Mater. Sci.* 57 (2012) 437–486, <https://doi.org/10.1016/j.pmatsci.2011.06.001>.
- [3] M.J.S. Spencer, Gas sensing applications of 1D-nanostructured zinc oxide: insights from density functional theory calculations, *Prog. Mater. Sci.* 57 (2012) 437–486, <https://doi.org/10.1016/j.pmatsci.2011.06.001>.
- [4] Sonalika Agarwal, Prabhakar Rai, Eric Navarrete Gatell, Eduard Llobet, Frank Güell, Manoj Kumar, Kamalendra Awasthi, Gas sensing properties of ZnO nanostructures (flowers/rods) synthesized by hydrothermal method, *Sensors and Actuators B: Chemical*, <https://doi.org/10.1016/j.snb.2019.04.083>.

# Chemical Vapor Deposited ZnO Nanowires for Ethanol and NO<sub>2</sub> Gas Detection

Eric Navarrete <sup>1</sup>, Frank Güell <sup>2</sup>, Paulina R. Martínez-Alanis <sup>2</sup> and Eduard Llobet <sup>1,\*</sup>

<sup>1</sup>MINOS-EMaS, Universitat Rovira i Virgili, Avda. Paisos Catalans, 26, 43007 Tarragona, Spain

<sup>2</sup>ENFOCAT-IN2UB, Universitat de Barcelona, C/Martí i Franquès 1, 08028 Barcelona, Catalunya, Spain;

[frank.guell@ub.edu](mailto:frank.guell@ub.edu), [paulina.martinez@ub.edu](mailto:paulina.martinez@ub.edu)

\* Correspondence: [eduard.llobet@urv.cat](mailto:eduard.llobet@urv.cat); Tel.: +34 977 558 502

## Abstract

Randomly oriented ZnO nanowires were grown directly onto alumina substrates having platinum interdigitated screen-printed electrodes via the chemical vapor deposition method using Au as catalyst. Three different Au catalyst thicknesses (i.e., 3, 6 or 12 nm) were conducted in the growth of nanowires, and their gas sensing properties were studied for ethanol and NO<sub>2</sub> as reducing and oxidizing species, respectively. ZnO nanowires grown employing the 6 nm thick layer were the less defective and showed the most stable, repeatable gas sensing properties. Despite ZnO nanowires grown employing the thickest Au layer reached the highest responses under dry conditions, ZnO nanowires grown using the thinnest Au film were more resilient at detecting NO<sub>2</sub> in the presence of ambient moisture. The gas sensing results are discussed in light of the defects and the presence of Au impurities in the ZnO nanowires, as revealed by the characterization techniques used, such as X-ray diffraction, field-emission scanning electron microscopy, X-ray photoelectron spectroscopy and photoluminescence spectroscopy. Promising results were obtained by the implementation of ZnO NWs directly growth over the alumina substrate for the detection of ethanol and NO<sub>2</sub> substantially ameliorating our previously reported results.

## 1. Introduction

During the early eighties, different authors reported the use of ZnO, either pure or loaded with catalytic metals, for sensing ethanol, carbon monoxide, methane, hydrogen sulfide, hydrogen, ammonia or nitrogen oxides [1]. All these gaseous species are important targets for inexpensive gas sensors because they are relevant to many applications such as home safety, livestock building management or air quality monitoring [2]. Even though SnO<sub>2</sub> has become the most researched and the most successful material in commercial chemoresistive sensors, ZnO has retained its research appeal over the years. This

interest in ZnO as a gas sensitive material has increased even further in the last years, especially with the study of nanostructured materials such as nanorods, nanowires (NWs), nanospheres, nanotetrapods or nanoflowers [3,4]. Gas-sensitive ZnO nanomaterials have been synthesized using a wide range of methodologies, which include hydrothermal and solvothermal methods, electrospinning or chemical vapor deposition (CVD) [5], only to cite a few.

In this work, we report the direct growth of ZnO NWs on commercially available alumina substrates having screen-printed, platinum interdigitated electrodes and a heating meander. This direct assembly of the gas-sensitive nanomaterial on the transducer substrate eases the sensor fabrication process, avoiding the need for transferring the ZnO NWs from the growth substrate onto the application substrate. It also enables achieving good and stable contacts between the NWs and the electrodes. ZnO NWs were synthesized via a catalyzed CVD process that results in a vapor-liquid-solid (VLS) growth mechanism.

## 2. Sensor synthesis and gas characterization

**Gold catalyst deposition:** Au thin films with various nominal thicknesses of 3, 6 and 12 nm were deposited by sputtering over the electrode area (5 x 5 mm<sup>2</sup>) of the alumina transducers. The alumina substrate was a ceramic Rubalit 708 commercial available by Ceram Tech GmbH, Plochingen, Germany, with a medium grain size of 3 to 5 μm and a typical surface roughness of 0.35 μm.

**ZnO nanowires growth:** ZnO powder was mixed with graphite powder at 1:1 mole ratio and the synthesis was carried out in a horizontal quartz tube placed in a CVD furnace. Argon was used as an inert carrier gas and the furnace was heated from room temperature to 900 °C, kept at 900 °C for 30 min (phase in which the growth takes place), and then naturally cooled down to room temperature. The powder mixture and the substrate were placed in the center of the furnace. The argon gas flow was 400 sccm and the pressure inside the tube was maintained at 760 Torr during all the process. The 3 different type of

sensors fabricated were labelled as **ZnO 3**, **ZnO 6** and **ZnO 12**, according to thickness of the Au catalyst films.

**Gas sensing characterization:** The gas sensing tests were conducted in a laboratory environment where the sensor response and behavior towards an oxidizing gas ( $\text{NO}_2$  at 250, 500 and 1000 ppb) and a reducing vapor (ethanol at 5, 10 and 20 ppm) were studied. The different gas sensors were studied at the operating temperatures of 150, 200 and 250 °C. Gas sensing measurements consisted of continuously acquiring and recording the DC resistance of the sensors while they underwent repeated exposure and recovery cycles of either  $\text{NO}_2$  or ethanol. In addition to the gas sensing studies conducted in a background of dry air, measurements were conducted as well in a background of humidified air (50 % relative humidity) to better understand sensor behavior when ambient moisture is present.

### 3. Results

**Material characterization:** To fully characterize the material; the crystallographic phase was studied by means of XRD, the morphology of the ZnO NWs and a chemical mapping were investigated by FESEM, room-temperature PL measurements were made and XPS measurements were also performed. The results obtained are shown in the following figures.

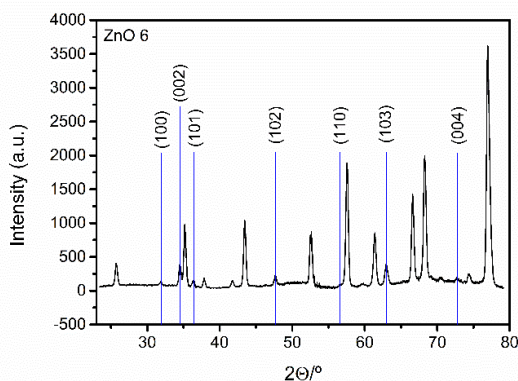


**Figure 1.** XRD diffractogram for a ZnO 6 sample grown on top of an alumina transducer substrate. The peaks with a blue line corresponds to the hexagonal ZnO pattern and the unlabeled peaks to the alumina substrate. All sensors presented the same XRD diffractogram.

	Length (nm)	Near tip (nm)	Near base (nm)
ZnO 3	1000 ± 250	33 ± 5	56 ± 15
ZnO 6	600 ± 118	34 ± 6	65 ± 14
ZnO 12	500 ± 139	44 ± 10	83 ± 13

**Table 1.** NW dimensions averaged values for 20 random measurement points for each Au catalyst thickness.

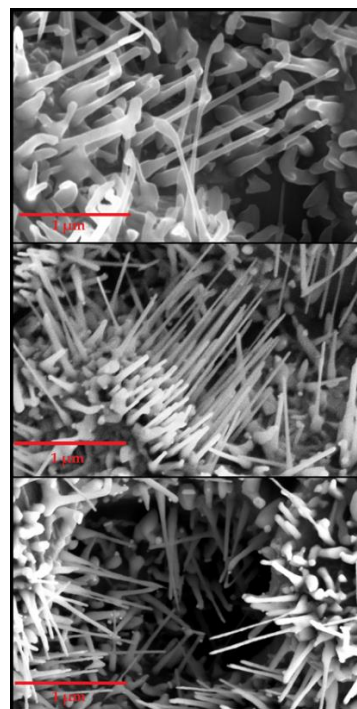


**Figure 2.** FESEM micrographs obtained from the surface of the 3 different types of samples. ZnO 3 (upper panel), ZnO 6 (middle panel) and ZnO 12 (lower panel).

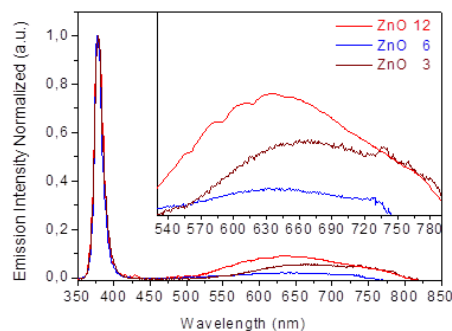


**Figure 3.** Room-temperature PL emission spectra for the ZnO NWs grown over the electrode area of alumina transducers as a function of the thickness of the sputtered Au film.

The PL provides significant information about the crystal-quality of the samples by its implication in the optical properties of the material. Figure 3 shows the room temperature PL spectra for the samples ZnO 3, ZnO 6 and ZnO 12. By pumping at 325 nm, we observed two emission bands, one strong emission in the UV at around 380 nm and a broader emission band in the visible range from 500 to 800 nm. The intensity of each spectrum was normalized to the intensity of the UV emission for relative comparison. The UV peak corresponds to the near band-edge emission, associated with exciton recombination processes [6], while the broad emission band observed in the visible range is generally attributed to defects [7].



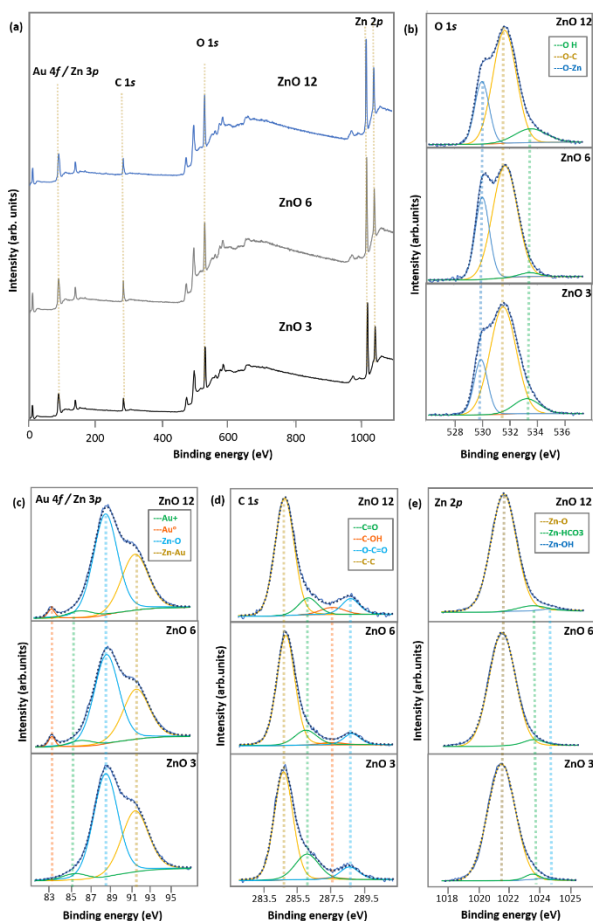


**Figure 4.** Overview XPS spectra of samples ZnO 3, ZnO 6 and ZnO 12 (a). High-resolution XPS spectra for the O 1s (b), the Au 4f and Zn 3p (c), the C 1s (d) and the Zn 2p (e) core levels.

The survey spectra of the samples ZnO 3, ZnO 6 and ZnO 12 show the main signals corresponding to the Au 4f, Zn 3p, C 1s, O 1s and Zn 2p core levels, see Figure 4 (a). The analysis of the high resolution spectra for the O 1s core level shows the contribution of the O-Zn, O=C, and OH species at around 530, 531.6 and 533. 5 eV BE, respectively, see Figure 4 (b) [7]. The analysis of the high resolution spectra for the Au 4f core level is presented in Figure 4 (c). In this figure, the bands associated to the Au 4f and the Zn 3p core levels are overlapped, and the complex spectrum was deconvoluted in four components for the samples ZnO 6 and ZnO 12 or three components for the sample ZnO 3. The bands centred at around 83.2, 85.6, 88.5 and 91.5 eV BE being related to the Au 4  $f^{7/2}$  core level of Au<sup>0</sup> and Au<sup>+</sup>, and to the Zn 3p<sup>3/2</sup> of the Zn-O and Zn-Au interaction, respectively, see figure 6 (c) [8]. Note that the Au 4  $f^{7/2}$  core level at 83.2 eV BE is not observed for the sample ZnO 3, see Figure 4 (c). This can be attributed to the kind of growth of the ZnO NWs in which the gold is encapsulated at the bottom for sample ZnO 3. For the samples ZnO 6 and ZnO 12, the gold catalyst Au<sup>0</sup> appears at the tip of the ZnO NWs [7], and the Au 4  $f^{7/2}$  core level at 83.2 eV BE is observed, see Figure 4 (c).

**Gas characterization:** The gas sensing studies were

conducted for each sensor operated at 150, 200 and 250 °C in order to determine the best optimal working temperature at three different concentration levels for each target gas NO<sub>2</sub> and Ethanol and summarized in table 2 and 3 respectively.

T (°C)	ZnO 3	±	ZnO 6	±	ZnO 12	±
150	6.5	0.4	2.5	0.1	3.1	0.1
200	16.7	0.6	5.0	0.2	5.6	0.2
250	36.3	6.9	25.0	1.8	51.0	5.9

**Table 2.** Averaged sensor responses ( $R_{\text{gas}}/R_{\text{air}}$ ) and their standard deviations when exposed to 1 ppm of NO<sub>2</sub> at different operating temperatures under dry air conditions.

After having determined experimentally 250 °C as the optimal working temperature for NO<sub>2</sub> detection, the impact of ambient humidity was studied. The gas sensing experiments were repeated at 250 °C and the gas flow was humidified to 50 % R.H. before being introduced into the test chamber. The results obtained are shown in Figure 5. When humidity was introduced in the system, the overall sensor responses were negatively impacted. In average, the decrease in sensor response observed for 1 ppm of NO<sub>2</sub> was near a factor of 2 for both ZnO 3 and ZnO 6 samples. However, the most humidity-affected material was ZnO 12 with a 4.5-fold decreased response. Interestingly, ZnO 3 displayed in this case the higher responses for NO<sub>2</sub> under humid conditions and it is worth pointing out that the response of this nanomaterial towards 250 and 500 ppb of NO<sub>2</sub> was barely affected by the presence of humidity. The important decrease in the response towards NO<sub>2</sub> for ZnO 12 could be attributed to its higher concentration of defects, as revealed by PL.

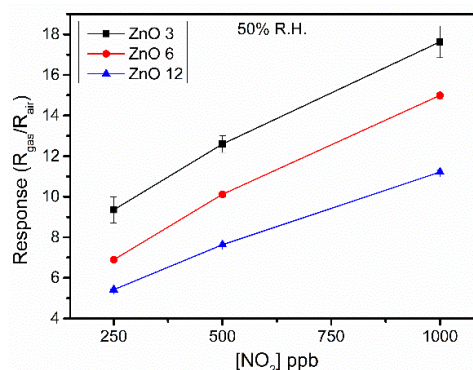


**Figure 5.** Sensor calibration curves for NO<sub>2</sub>. Sensors were operated at 250 °C under humidified air conditions (50% R.H.).

T (°C)	ZnO 3	±	ZnO 6	±	ZnO 12	±
150	1.4	0.1	1.1	0.01	1.2	0.02
200	4.6	0.6	6.0	1.0	9.2	2.1
250	3.8	0.4	5.2	0.4	6.6	0.6

**Table 3.** Averaged sensors responses ( $R_{\text{air}}/R_{\text{gas}}$ ) and their standard deviations when exposed to 20 ppm of ethanol at different operating temperatures under dry air conditions.

The impact of ambient humidity was also studied for ethanol. The operating temperature chosen to perform the test was 250 °C and the relative humidity was, once more, set to 50% in order to make a better comparison between the behavior of the different sensors in front of the two different gaseous species studied. Figure 6 shows the results obtained for the sensors when tested for ethanol vapors under humid conditions. When ambient humidity was present, the response of the ZnO 3 sensor towards ethanol completely disappeared, as the sensor was unable to react with the vapor. In the case of ZnO 6 and ZnO 12, the response behavior showed a similar pattern with the occurrence of a clear response saturation above 10 ppm of ethanol. In addition to this response saturation effect, ZnO 6 and ZnO 12 based sensors suffered a 2.4 and 3.5-fold decrease in their response to ethanol, respectively (for the two lowest concentrations tested). Considering the lack of ethanol response for ZnO 3, the decrease in response and response saturation observed for ZnO 6 and ZnO 12, it can be derived that the presence of ambient humidity has a higher impact in the detection of ethanol vapors than in NO<sub>2</sub> sensing.

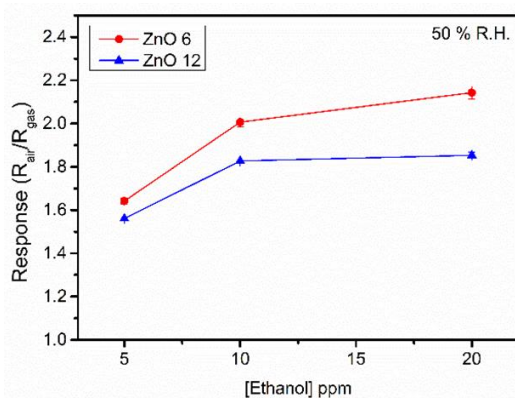


**Figure 6.** Sensor calibration curves for ethanol. Sensors were operated at 250 °C under humidified air conditions (50% R.H.). The curve for ZnO 3 does not appear in this plot due to the lack of response observed under humid conditions for this material.

## 5. Conclusions

ZnO NWs were successfully synthesized through CVD (VLS growth mechanism) after employing different thicknesses (3, 6 and 12 nm) for the Au catalyst layer deposited by sputtering. The thickness of the catalyst layer has a high influence in the number of defects in the resulting ZnO NWs and in the presence/absence of Au impurities. ZnO 6 is the sample with fewer defects and ZnO 3 is the only sample in which surface Au impurities are not detected in a chemical mapping. The direct growth of the gas sensitive nanomaterials onto the application substrates results in increased sensitivity and stability. ZnO NWs grow with no particular orientation in the form of disordered mats. Owing to their significant number of defects, as revealed by PL, ZnO NWs show high sensitivity towards NO<sub>2</sub> at ppb levels when operated at 250 °C. ZnO NWs having Au NPs at their tips and

surface show a moderate sensitivity to ethanol (in the ppm range). While a higher number of defects is favorable for the detection of NO<sub>2</sub>, the presence of Au impurities (e.g. in the form of Au NPs at the surface of ZnO NWs) is detrimental when in the presence of ambient moisture. In contrast, the presence of Au NPs helps enhance ethanol detection, possibly via a chemical sensitization effect. Given the fact that the ZnO 3 sample retains its responsiveness towards NO<sub>2</sub> in the presence of ambient moisture while it shows no response to ethanol, this makes ZnO 3 sample a potentially suitable material for detecting NO<sub>2</sub> in atmospheres where ethanol could be an interfering species.

## References

- [1] G. Heiland, "Homogeneous semiconducting gas sensors," *Sensor Actuat. B-Chem.*, vol. 2, pp. 343–361, 1981.
- [2] Q. Wan, Q. H. Li, Y. J. Chen, and T. H. Wang, "Fabrication and ethanol sensing characteristics of ZnO nanowire gas sensors," *Appl. Phys. Lett.*, 2004, vol. 84, no. 18, pp. 3654–3656.
- [3] Wang, J. X., Sun, X. W., Yang, Y., Huang, H., Lee, Y. C., Tan, O. K. and Vayssieres, L., "Hydrothermally grown oriented ZnO nanorod arrays for gas sensing applications," *Nanotechnology*, 2006, vol. 17, no. 19, pp. 4995–4998.
- [4] S. Agarwal, P. Rai, E. Navarrete, E. Llobet, F. Güell, M. Kumar and K. Awasthi, "Gas sensing properties of ZnO nanostructures (flowers/rods) synthesized by hydrothermal method," *Sensor Actuat. B-Chem.*, 2019, vol. 292, no. April, pp. 24–31.
- [5] S. Roso, F. Güell, P. R. Martínez-Alanis, A. Urakawa, and E. Llobet, "Synthesis of ZnO nanowires and impacts of their orientation and defects on their gas sensing properties," *Sensors Actuators, B Chem.*, vol. 230, pp. 109–114, 2016.
- [6] J. S. Reparaz, F. Güell, M. R. Wagner, G. Callsen, R. Kirste, S. Claramunt, J. R. Morante & A. Hoffmann, "Recombination dynamics in ZnO nanowires: Surface states versus mode quality factor," *Appl. Phys. Lett.*, 2010, vol. 97, no. 13, pp. 133116.
- [7] F. Güell, J.O. Ossó, Goñi A.R., Cornet A. and Morante J.R. "Direct imaging of the visible emission bands from individual ZnO nanowires by near-field optical spectroscopy." *Nanotechnology*. 2009, vol 20, no. 31, pp. 315701.
- [8] P. Kundu, N. Singhanian, G. Madras and N. Ravishankar. "ZnO–Au nanohybrids by rapid microwave-assisted synthesis for CO oxidation," *Dalton Trans.*, 2012, vol. 41, pp. 8762–8766.

# Optical Platform to Analyze a Model Drug-Loading and Releasing Profile Based on Nanoporous Anodic Alumina Gradient Index Filters

Pankaj Kapruwan, Josep Ferré-Borrull\*, Lluís F. Marsal\*

Engineering. Electrònica, Elèctrica i Automàtica, Universitat Rovira i Virgili, 43007, Tarragona, Spain

\*Email: josep.ferre@urv.cat, lluis.marsal@urv.cat

## Abstract

In this work, a methodology that exploits the optical properties of the nanoporous anodic alumina gradient index filters (NAA-GIFs) has been developed and applied to evaluate in real time the release dynamics of a cargo molecule, acting as a model drug, filling the pores. NAA-GIFs with two photonic stopbands (PSBs) were prepared with one of its stop bands in the same absorption wavelength range of the cargo molecule, whereas the second stopband away from this absorption range. Numerical simulation and experiments confirm that the relative height of the high reflectance bands in the reflectance spectra of NAA-GIFs filled with the drug can be related to the relative amount of drug filling the pores. This property has been applied in a flow cell setup to measure in real-time the release dynamics of NAA-GIFs with the inner pore surface modified by layer-by-layer deposition of polyelectrolytes and loaded with the cargo molecule.

## 1. Introduction

Recent years have seen tremendous growth in the design and engineering of nanoporous structures based on modified anodization strategies. Amongst the porous structures, nanoporous anodic alumina (NAA) is a material that offers ease of fabrication, mechanical robustness, widely tuneability of surface chemistry and stable optical properties [1-3]. Recent developments in NAA pore engineering have made it possible to develop numerous optically active templates (e.g. distributed Bragg reflectors, gradient-index filters, etc.)

In this work, we propose to obtain NAA-GIFs with two high reflection bands, one of them in the wavelength range where a cargo molecule has a maximum optical absorption, while the other in a wavelength range far from such absorption. As a cargo molecule, we use Rhodamine 6G (Rh6G) having high fluorescence properties. Once the changes between both the PSBs were correlated and verified, this method was applied to demonstrate the pH responsiveness of NAA-GIFs in real-time.

## 2. Experimental section

**Fabrication:** NAA-GIFs were fabricated by a one-step electrochemical anodization process by applying a sinusoidal anodization profile described here [4]. In brief, the aluminum substrates were treated with acetone, ethanol, and water in sequence to remove all organic impurities present on the surface. Pre-treated aluminum foils were electropolished in a mixture of 4:1 v/v of ethanol: perchloric acid at 20 V for 5 min, followed by anodization in an electrochemical cell containing 0.3 M oxalic acid at 5 °C under controlled stirring.

The samples prepared in this study were obtained with  $J_{average} = 2.6 \text{ mAcm}^{-2}$ ,  $J_{amplitude} = 1.3 \text{ mAcm}^{-2}$ ,  $T_1 = 152 \text{ s}$  and  $T_2 = 210 \text{ s}$ . Three different sets of samples were prepared with  $N = 150$ ,  $N = 200$  and  $N = 250$ .

After fabrication, the remaining aluminium was etched from the back side using a solution of copper chloride ( $\text{CuCl}_2$ ) and hydrochloric acid (HCl) followed by a pore widening step of 10 minutes using 5 wt%  $\text{H}_3\text{PO}_4$  at 35 °C for 15 min. Next, the loading of the pores was performed by successive repetitive cycles of drop casting 10  $\mu\text{l}$  of Rhodamine solution (1 mg/ml) onto the surface of NAA-GIFs and drying at room temperature. To hold the cargo molecules inside the NAA-GIFs, an incorporation of multilayered polyelectrolytes have been performed in a separate procedure.

## 3. Results and Discussion

Figure 1 represents the applied anodization current density and measured anodization voltage graphs as a function of time for different samples prepared by applying different numbers of periods, i.e.,  $N = 150$ , 200, and 250.

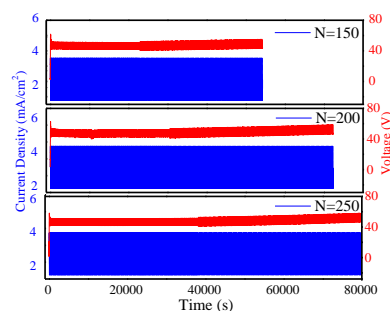


**Figure 1.** Complete sinusoidal anodization profile applied to obtain NAA-GIFs

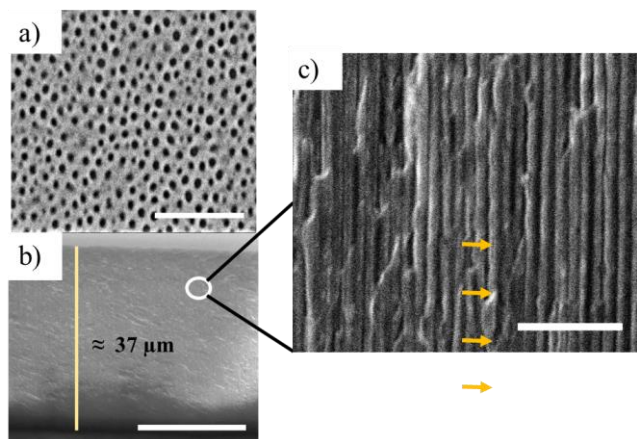


**Figure 2.** ESEM pictures of as-produced NAA-GIFs for samples with  $N = 200$ ; (a) Top view (Scale bar =  $1 \mu\text{m}$ ); (b) cross section (Scale bar =  $25 \mu\text{m}$ ); (c) Magnified view of figure (b) showing the modulations in the structure (Scale bar =  $1 \mu\text{m}$ ). Average pore diameter (dp) of  $45 \pm 4 \text{ nm}$ .

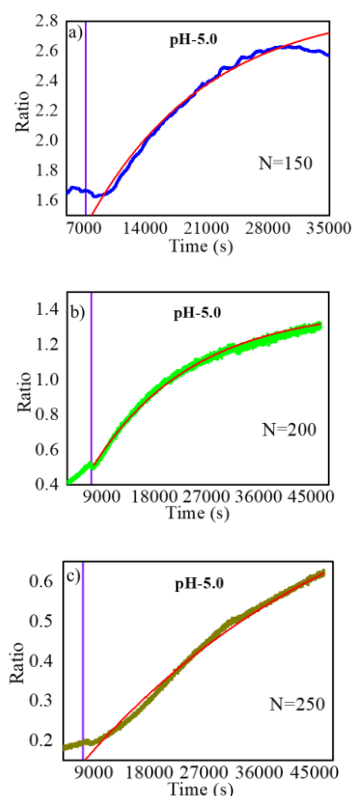


**Figure 3.** Ratio of the maximum intensity of the signal band to the maximum intensity of the reference band as a function of time, for samples with (a)  $N = 150$ , (b)  $N = 200$ , (c)  $N = 250$ . The line in each graph is the best fit for an exponential function as described in the text.

Figure 3 demonstrates the three real-time release curves showing an increasing trend for the release of cargo molecules after the introduction of the pH 5.0 solution. For the curve corresponding to  $N = 150$ , the increasing trend stops at approximately 7.7 h. Instead, for  $N = 200$ , it can be observed that the trend reduces its increase rate with time, but without reaching a stabilization. Finally, for  $N = 250$  the curve also shows a reduction of the increase rate, but with a smaller scale.

#### 4. Conclusions

This study successfully demonstrates the ability of NAA-GIFs to be used as an optical platform for analyzing the loading and release of a cargo molecule. Real-time release measurements were carried out in a flow cell that allows measuring the changes in the stopbands during the release process. We believe that the methodology developed in this work, exploiting the optical properties of the porous nanostructures can be further applied to the study of drug delivery systems to obtain information about the filling process and real-time data for the releasing process.

#### 5. Acknowledgement

This work was partially supported by the Spanish Ministerio de Ciencia, Innovación y Universidades (MICINN/FEDER) RTI2018-094040-B-I00, by the Agency for Management of University and Research Grants (AGAUR) ref. 2017-SGR- 1527 and by the Catalan Institution for Research and Advanced Studies (ICREA) under the ICREA Academia Award.

#### 6. References

- 1) Macias G, Ferré-Borrull J, Pallarès J, Marsal LF. *Nanoscale Res Lett.* 2014;9(1):1-6.
- 2) Porta-i-Batalla M, Xifré-Pérez E, Eckstein C, Ferré-Borrull J, Marsal LF. *Nanomaterials.* 2017;7(8):227.
- 3) Rahman MM, Marsal LF, Pallarès J, Ferré-Borrull J. *ACS Appl Mater Interfaces.* 2013;5(24):13375.
- 4) Acosta LK, Bertó-Roselló F, Xifre-Perez E, Santos A, Ferré-Borrull J, Marsal LF. *ACS Appl Mater Interfaces.* 2019;11(3):3360.



# Metabolic Dysregulations Associated to Thirdhand Smoke Exposure in Mice: Implications for Human Urine Biomonitoring

Carla Merino<sup>1</sup>, Sara Samino<sup>1</sup>, Beatrix Paton<sup>1</sup>, Manuela Martins-Green<sup>2</sup>,  
María Vinaixa<sup>1</sup>, Noelia Ramírez<sup>1</sup>

1. Metabolomics Interdisciplinary Lab, Department of Electrical Electronic Engineering and Automation, University Rovira i Virgili, Institute for Health Investigation Pere Virgili, CIBERDEM, 2. Department of Cell Biology and Neuroscience, University of California, Riverside CA 92521, U.S.A.

E-mail contact: [carlanelissa.merino@urv.cat](mailto:carlanelissa.merino@urv.cat)

## 1. Introduction

Tobacco smoke, formed by a complex mixture of particles and thousands of toxicants including over 70 carcinogens according to the International Agency for Research on Cancer [1], is a ubiquitous outdoor and indoor environmental pollutant that has been overlooked to date by the environmental and health policies. Most of the smoke gases and particles deposit, age and remain for long periods of time in fabrics, surfaces and dust forming the so-called **thirdhand smoke** (THS), a less studied source of exposure to tobacco smoke toxicants that especially affects children living with smokers. THS components not only remain on surfaces and in settled dust, but they can also be re-emitted into the gas phase or even react with oxidants and other atmospheric compounds to yield secondary contaminants, some of them with increased toxicity [2]. In recent years, many studies have focused on the assessment of THS exposure impact, progressing on THS chemical composition and risks and providing evidences on the adverse health effects, including *in vitro* and *in vivo* studies that revealed genotoxicity, DNA damage, tumour incidence, cellular oxidative stress, non-alcoholic fatty liver disease, hyperglycaemia, insulin resistance, poor wound healing, impairment in immune function, and hyperactivity [3]. However, the metabolic profiling to assess THS exposure impact in non-invasive biofluids as urine is still understudied.

## 2. Objective

The aim of this study is to characterize THS exposure in urine of exposed mice. To accomplish this, we analysed urine from mice exposed to THS under conditions that mimic human exposure in smokers' homes. The metabolic alterations caused by this exposure were evaluated with an untargeted multiplatform metabolomics approach using both LC-MS and GC-MS.

## 3. Materials and methods

### 3.1. THS exposure model design

Animal models have been developed at the Cell and Biology Department at the University of California Riverside, following THS exposure protocols previously reported [4,5]. Briefly, C57BL/6 mice were divided into control and experimental group. The experimental group was exposed to household fabrics polluted with THS from weaning (three weeks of age) to 24 weeks without exposure to SHS at anytime during the study; the control group was never exposed to THS or SHS. Mice were fed a standard chow diet (percent calories: 58% carbohydrate, 28.5% protein, and 13.5% fat). Urine samples of the five biological replicates per group were collected at the end of the exposure, snap frozen, and sent to our group facilities in dry ice.

### 3.2. Metabolic and lipidomic sample extraction

Urine samples were extracted using standard protocols for LC-MS and GC-MS with some modifications. For LC-MS, 200  $\mu$ L of MeOH:H<sub>2</sub>O (8:1) and 20  $\mu$ L of internal standard solution were added to 40  $\mu$ L of urine samples, vortex mixed for 1 min, kept at 4°C for 20 min and centrifuged at 4°C and 15000 rpm for 10 min. For GC-MS, 20  $\mu$ L aliquots of each mice urine were vortex mixed with 40  $\mu$ L of urease suspension (80 mg/mL in ultrapure water) and incubated at 37°C and 500 rpm for one hour. Following urea depletion, 100  $\mu$ L of MeOH:H<sub>2</sub>O (8:1) was added to the samples, vortex mixed and centrifuged at 4°C for 10 min at 15,000 rpm. Aliquots of 70  $\mu$ L of supernatant of each sample were dried under nitrogen and lyophilized overnight. The next day, 30  $\mu$ L of oxymation reagent were added to the dried metabolic extracts, incubated for 1.5 h, at 37°C and 500 rpm, next derivatized by adding 45  $\mu$ L of MSTFA with 1% TMCS and incubated at room temperature under darkness for one hour. Quality control samples (QCs) for LC-MS and GC-MS analysis were prepared by pooling equal volumes of each sample, respectively. Samples and QCs were stored at -80 °C until further analysis.

### 3.3. Untargeted LC-MS and GC-MS

For LC-MS, samples were analysed in a 1290 UHPLC system coupled to a 6550 quadrupole time of flight (QTOF) mass spectrometer, both from Agilent Technologies (Palo Alto, CA, USA) operated in positive electrospray ionization (ESI+) mode and separated using a using an ACQUITY UPLC HSS T3 C18 reverse phase column (150  $\times$  2.1 mm, 1.8  $\mu$ m) from Waters (Milford, MA, USA). For GC-MS, derivatized extracts were analysed in a 7890A gas chromatograph coupled to a 7200 quadrupole-time of flight mass spectrometer, both from Agilent using an HP-5 MS capillary column (30 mm  $\times$  0.25 mm  $\times$  0.25  $\mu$ m), also from Agilent. In both

analytical techniques, several QCs were injected before the first sample and then repeatedly analysed throughout the sequence.

### 3.4. Data analysis and pathway

Following data acquisition and processing, univariate and multivariate statistical analysis was performed to differentiate the significant features. Metabolite identification were done by comparison the MS/MS spectrum with reference standards or using METLIN database, in the case of LC-MS data, or GMD, in the case of GC-MS data. Pathway enrichment of identified metabolites was performed in Metabolomic Pathway Analysis (MetPA) using *Mus musculus* as background organism generated at MetaboAnalyst.

## 4. Results and discussion

### 4.1. THS exposure biomarkers

To evaluate the extent of nicotine and TSNA's absorption because of THS exposure, we monitored the presence of tobacco specific metabolites in the urine extracts. We identified a large number of tobacco constituents including nicotine—one of the most prevalent constituents in tobacco smoke [6], and NNK and NNN—the two most harmful TSNA's considered carcinogenic Group 1 for humans by the IARC [7] which produced tumours at multiple organ level in different mammalian models [8]. Exposed mice also metabolized those compounds and activated pathways of NNK and NNN carcinogenesis through CYP450-mediated  $\alpha$ -hydroxylation [8], demonstrating for the first time the generation of HPBA and OPBA in a THS-exposed model.

### 4.2. Metabolomics alterations caused by THS exposure

Our multiplatform metabolic analysis revealed the vast extent of metabolic disturbances related with THS in urine of exposed mice, as illustrates the Cloud Plot of Figure 1. We identified seventy-seven dysregulated metabolites—being most of them upregulated in THS group—that were involved in fifteen altered pathways, demonstrating the metabolic detrimental effect of THS in exposed mice.

Pathway analysis of Figure 2 revealed that tryptophan metabolism was one of the most enriched pathways with sixteen metabolites dysregulated, including the neurotransmitter serotonin, and those related with the kynurenine pathway. Besides, THS exposure also produced the upregulation of the neurotransmitters: dopamine, epinephrine, GABA, and glutamate, and the glucocorticoid hormones: cortexolone, cortisol, and cortisone. We observe a higher quinolinic acid/kynurenine acid ratio in exposed group, indicating an increment of neurotoxicity [9] and demonstrating for the first time a possible explanation of molecular alterations behind THS-related neurological and neuro-behavioural alterations.

## 5. Conclusions

The results summarized here demonstrate for the first time the possible metabolic mechanism behind THS-related neurotoxicity, adds further evidences on THS detrimental effect, and provides new bases for human urine biomonitoring in THS research.

## 6. References

- [1] IARC Monograph Vol. 83. Tobacco Smoke and Involuntary Smoking; 2004.
- [2] Matt, G. *et al.* Environmental Health Perspectives. 2011; 119(9): 1218–1226.
- [3] Díez-Izquierdo, A. *et al.* Environmental Health Perspectives. 2018; 167: 341–371
- [4] Adhami, N. *et al.* PLoS One. 2016; 11(3): e0149510
- [5] Martins-Green, M. *et al.* PLoS ONE. 2014; 9(1): e86391
- [6] Benowitz, N. *et al.* Handbook of Experimental Pharmacology. 2009; (192): 29–60.
- [7] IARC Monograph Vol. 89. Evaluation of Carcinogenic Risks to Humans Smokeless Tobacco and Some Tobacco-specific N-Nitrosamines; 2007.
- [8] Hecht, S. Chemical Research in Toxicology. 1998; 11(6): 559–603
- [9] O'Farrell, K. *et al.* Neuropharmacology. 2017; 112: 307e323

**Acknowledgements** – The authors want to acknowledge the financial support of Direcció General de Recerca of the Government of Catalonia (2020 FI\_B2 00118); the Spanish Ministry of Economy (IJCI-2015-23158); the Instituto de Salud Carlos III (CP19/00060); and the Tobacco-Related Disease Research Program (TRDRP) of the University of California (2RT-0121 and 23DT-0103)

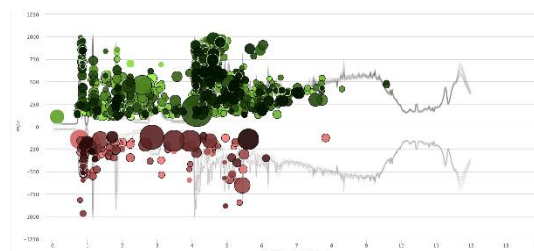


**Figure 1.** Cloud Plot of dysregulated features ( $p$  val < 0.01, FC > 2). The figure shows the total ion chromatograms, the upregulated (in green) and the down regulated (in red) features. The size of the bubble indicates de log fold change of the feature and the intensity of the colour the statistical significance.

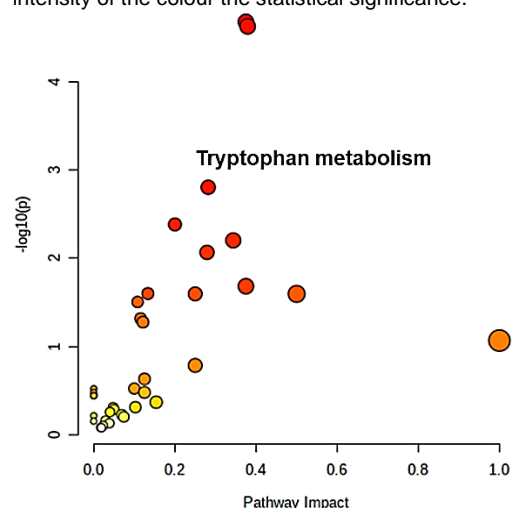


**Figure 2.** Metabolomic Pathway Analysis (MetPA) of significant endogenous metabolites altered by THS exposure.

# Contribution to the Development of a Multifrequency Energy Distribution System for Battery Charging in Electric Vehicles

X. Genaro-Muñoz<sup>1</sup>, H. Valderrama-Blavi<sup>1</sup>, R. Giral<sup>1</sup>.

<sup>1</sup>GAEI Laboratory, Rovira i Virgili University. Av. Països Catalans 26, 43007 Tarragona, CAT-Spain

**Abstract**— This work investigates the selective energy transfer between users located inside a multifrequency bus. Multifrequency power transfer involves the combination of two or more alternating signals of different frequencies on the same power transmission line to subsequently supply loads at one or more of these frequencies.

As an example, this proposal manages the charge of two batteries for electric vehicles (EV). One EV battery is charged from grid power and the other one with renewable energy using the additional power channel in the same distribution bus.

In this case, the multifrequency system uses the grid frequency and its third harmonic, so that each power channel uses one of the frequencies.

To demonstrate the viability of this proposal, a set of paired converters, a transmitter and a receiver located at different points on the bus, are designed to perform a power transfer at the additional frequency. The energy transfer is performed point to point without interfering the operation of the other elements connected to the bus. The synchronization of the controls creates a virtual power path for each installed sender-receiver set.

**Keywords** — Multifrequency, distributed system, battery management, electric vehicles, power transmission, power transfer, converter control.

## I. INTRODUCTION

At present, energy distribution problems, large increases in demand, and the growth of renewable energies leads to a serious reconsidering of current energy distribution systems. Many Microgrid type proposals [1] include distributions with reduced and more spread out power generation points. The case of Smart Grids is a clear example of decentralization of the energy management. Other proposals for Microgrids contemplates an increase on DC systems demand [2]. Other systems combine two distribution lines, one with alternating current and a second one with direct current; merging both in the same bus as a first type of multifrequency system (DC + AC) [3], [4].

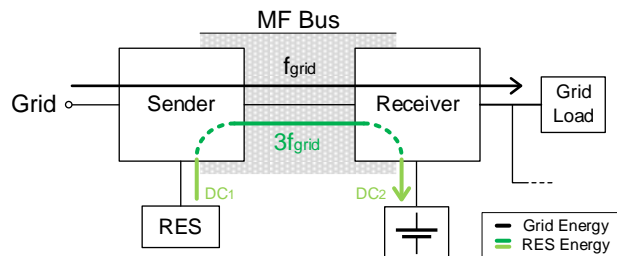


Figure 1: Proposed Multifrequency Power Transfer System.

From this set of proposals for distribution systems, some already well-established and others more emerging, this work is oriented towards multifrequency with the combination of two alternating signals (AC1 + AC2).

Figure 1 illustrates the system described. The power generated in a renewable source is superimposed on a pre-existing grid-frequency AC bus, using the third harmonic to send it to the battery of an electric vehicle at the other end of the bus. In the chosen example, the renewable generation point also uses a battery to decouple the renewable intermittent generation from the vehicle's battery charge profile.

This type of power transmission requires control synchronization over the mirror-configured converters that constitute the sender-receiver set. The sender injects energy to the bus in third harmonic from. Then the receiver absorbs the injected harmonic entirely to avoid distortions on the signals of the elements connected to the bus at grid frequency. As the network loads and generation points are considered a priority, the transfer of energy by means of the third harmonic must coexist without interfering. For this reason, the additional power channel takes advantage of the current carrying capacity of the bus cables not used by the transfer at grid frequency.

The aim of this work is to provide a possible technological solution to start validating the concept of multifrequency transmission system of AC1+AC2 type.

## II. MULTI-FREQUENCY POWER TRANSFER: THE 3-PORT CONVERTER

To transfer energy at a given specific frequency, it is required that voltage and current at that frequency coexist. This transfer is maximized if the voltage and current harmonics are in phase. To perform third-harmonic power injection, a voltage source is inserted in series into one of the wires of the pre-existing system, as well as a current source is connected in parallel to the same system. Conversely, in order to extract the energy at the other end of the bus, it is necessary to insert a series voltage source cancelling the voltage harmonic and a current sink extracting from the bus exactly the same amount of current previously injected. Each set of voltage and current sources is implemented with a tri-port converter, as shown in Figure 2.

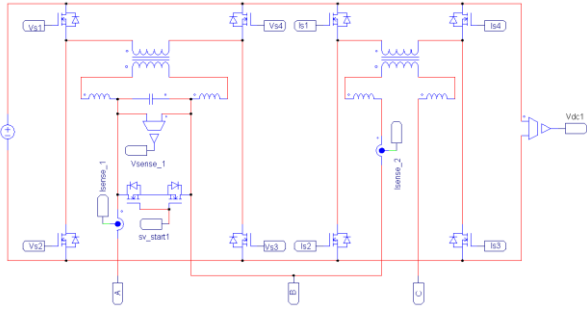


Figure 2: V-I Tri-port converter topology.

The figure above shows two inverter structures that implement the voltage and current set of sources. These structures are symmetrical and differ in the output capacitor of the voltage inverter and a current bypass. The transformer placed between the DC and AC parts provides the necessary galvanic isolation for the inverters to share a single DC battery as common power source.

The control of each inverter has its own regulation loop. Voltage inverters have an inner current and outer voltage control loops, while the current inverter only needs a current regulation. The corresponding references for each of these loops are obtained using a modified PLL (Phase-Locked-Loop), customized to synchronize with the third harmonic of a fundamental frequency, in our case the grid.

Lastly, a control unit installed in each of the tri-port systems manages its start-up, synchronization, and shutdown. The control unit also monitors the energy circulating on the bus and adapts the references for the tri-port systems to take advantage of the remaining current carrying capability of the bus cables.

### III. SIMULATION RESULTS

Figure 3a waveforms show the third-harmonic voltage injected by the sender and the corresponding cancelling signal at the receiver, shown as equal sinusoidal waveforms due to the mirrored configuration of the voltage inverters.  $180^\circ$  out-of-phase waveforms in Figure 3b correspond to the third-harmonic current injected by the sender and the one absorbed by the receiver.

Figure 4 illustrates how each inverter participates in the power transfer between batteries. Waveforms in Figure 4a show the voltage evolution of the batteries supplying the voltage inverters. A compensation is observed every cycle, resulting in a zero-power transfer. Figure 4b waveforms show that the voltage of the batteries supplying the current inverters, increase or decrease depending on the power transfer direction. The capacities of the batteries have been resized to shorten the test.

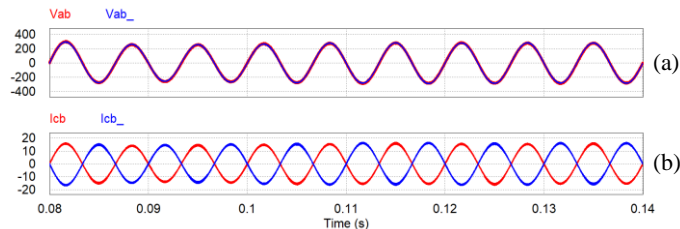


Figure 3: Third harmonic injection. (a) Sender (red) and receiver voltage (blue) (b) Sender (red) and receiver current (blue).

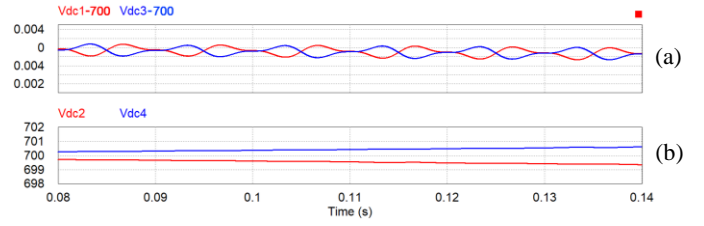


Figure 4: Battery discharge involvement from each inverter. (a) Sender voltage inverter (red) and receiver (blue). (b) Sender current inverter (red) and receiver (blue).

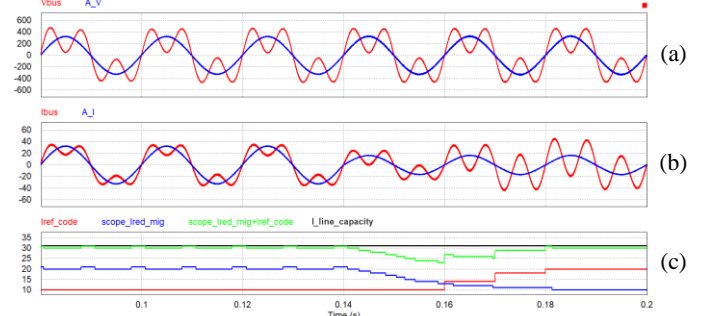


Figure 5: Load change at grid frequency. (a) Bus voltage (red), grid voltage (blue). (b) Bus current (red), grid current (blue). (c) Current third harmonic reference (red), grid current monitoring (blue), occupied capacity (green), line current capacity (black).

Figure 5 corresponds to a load transient at grid frequency. Voltage and current signals from the grid and the bus can be observed in Figure 5a and 5b respectively. Finally, Figure 5c illustrates the evolution of the third harmonic current reference. Given a current capacity of the line (black), the reference for the third harmonic current (red) is calculated after sensing the average value of the rectified grid harmonic (blue). After the load change, the third harmonic current increases in amplitude to occupy the freed-up space, as depicted by the signal representing the actual occupied cable capacity (green).

### IV. CONCLUSIONS

The proposed system allows a multifrequency power transfer of AC1+AC2 type through the third harmonic of a pre-existent system at a main frequency. The system does not interfere in the performance of the other elements from the bus. The tri-port converter circuits are feasible, and the third harmonic power transfer is possible.

### V. REFERENCES

- [1] S. Parhizi, H. Lotfi, A. Khodaei, and S. Bahramirad, "State of the art in research on microgrids: A review," *IEEE Access*, vol. 3, pp. 890–925, 2015, doi: 10.1109/ACCESS.2015.2443119.
- [2] E. Unamuno and J. A. Barrena, "Hybrid ac/dc microgrids - Part I: Review and classification of topologies," *Renew. Sustain. Energy Rev.*, vol. 52, pp. 1251–1259, 2015, doi: 10.1016/j.rser.2015.07.194.
- [3] R. Y. B. Conte, "Investigation of Multi-Frequency Power Transmission and System," Texas A&M University, 2011.
- [4] V. Chitransh and M. Veerachary, "Multi-frequency power system for renewable source integration in smart grid," *IET Power Electron.*, vol. 12, no. 7, pp. 1800–1808, 2019, doi: 10.1049/iet-pel.2018.5101.



# Gas Sensing Properties of Perovskite Decorated Graphene

Mohamed Ayoub Alouani, Juan Casanova Chafer, Eduard Llobet

Universitat Rovira I Virgili

[Mohamedayoub.alouani@urv.cat](mailto:Mohamedayoub.alouani@urv.cat), [juan.casanova@urv.cat](mailto:juan.casanova@urv.cat), [eduard.llobet@urv.cat](mailto:eduard.llobet@urv.cat)

## Abstract

This work explores the gas sensing properties of graphene nanolayers decorated with Cubic Zinc Stannate ( $Zn_2SnO_4$ ) nanoparticles for the detection of toxic gases such as Nitrogen Dioxide ( $NO_2$ ). The synthesized nanoparticles and the decorated nanolayer were characterized using several techniques such as X-Ray Diffraction, Field Emission Scanning Electron Microscopy and Transmission Electron Microscopy. High responses were obtained towards the nitrogen dioxide showing enhanced sensitivity when the graphene is doped with  $Zn_2SnO_4$  Nanoparticles.

## 1. Introduction

Gas sensors play an increasingly important role in our modern society, particularly for industrial gas emission control and public health security. Among many different gases, the rapid detection of dangerous gases such as nitrogen dioxide is technologically essential as these gases are causing atmospheric contamination (green house effect) and can be dangerous for human health very above low levels of exposure. Chemioresistive sensors have been presented as one of the promising sensors for detecting these type of gases due to their high sensitivity, low cost, reproducibility and simplicity. Thanks to its extraordinary high Carrier density and mobility, Graphene was seen as the ideal candidate to make these chemioresistive gas sensors and to enhance even more these characteristics, perovskite nanoparticles were loaded in the Graphene since they have exceptional properties such as large absorption coefficient, long carrier lifetime and high carrier mobility

## 2. Materials and Methods

### 2.1. Zinc Stannate nanoparticles Synthesis

Cubic Zinc Stannate nanoparticles were synthesised following a similar approach as the one used by Fakhrazad et al. where  $ZnO$  and  $SnO_2$  powders (99% purity) were mixed with different molar ratios of  $ZnO:SnO_2$  (2:1 and 4:1), then the mixed powder was

milled by hand for 30 min and the final step was an annealing at  $900^\circ C$  for 120 min.

### 2.2. Graphene Preparation and Decoration

Graphene nanoplatelets from Strem Chemicals, Inc. (USA) were dispersed in 10 ml of a mixture of ethanol and methanol (80%-20% respectively) and then sonicated for 30 min. The same procedure was followed to disperse the synthesised Zinc Stannate powders.

The decoration process consists of adding few drops of the Cubic  $Zn_2SnO_4$  solution in the graphene one under constant stirring at  $50^\circ C$ . Then let it stir for 30 min. The final mixed solution was put in sonification for another 30 min. 3 Solutions were prepared, one with bare graphene, one with graphene decorated with Zinc stannate NP's with 2:1  $ZnO:SnO_2$  molar ratio and another one with graphene decorated with 4:1  $ZnO:SnO_2$ .

### 2.3. Sensor Fabrication

The obtained materials, Graphene decorated with different Zinc Stannate nanoparticles, were deposited on commercial alumina sensors using a multiple droplet drop casting method at  $70^\circ C$ .

### 2.4. Material characterization

The synthesized nanoparticles and decorated graphene were characterized using different techniques such as the X-ray Diffraction (XRD), Transmission Electron Microscopy (TEM) and Field Emission Scanning Electron Microscopy (FESEM).

XRD was used to study the crystal structure of the synthesized nanoparticles, their shape and size in the graphene layer was studied using TEM and finally FESEM to check their dispersion on the Surface of the nanolayer.

### 2.5. Gas Sensing Measurements

The resistance changes under  $NO_2$  gas and experimental conditions were monitored using an Agilent HP 34972A multimeter connected to the gas sensing chamber.

## 3. Results

### 3.1 Material characterization

XRD graphs presented in figures 1a and 1b shows the same cubic phase for both 4:1 and 2:1 Synthesized Zinc

## Stannate nanoparticles

Transmission Electron Microscopy analysis was conducted to characterize the different sizes and shapes of both 2:1 and 4:1 ZnO:SnO<sub>2</sub> synthesised zinc stannate nanoparticles decorated in the graphene layer. Both Figures 2a and 2b shows good circular shapes and sizes ranges from 11.5 to 65 nm of the different molar ratios nanoparticles.

FESEM Images highlights the presence of the NP's with bright spots and also shows very good dispersion of them in the graphene layer with a slightly better dispersion of the 2:1 Zinc Stannate NP's shown in figure 3a than the 4:1 one shown in figure 3b. A porous surface of the graphene was observed also which is interesting for gas sensing.

### 3.2 Gas sensing Results

Nitrogen Dioxide (NO<sub>2</sub>) detection was performed by applying repeated exposure and recovery cycles to increasing concentrations of the gas. Figure 4 shows the calibration curves obtained for 40-60-80-100ppb of NO<sub>2</sub>, in which graphene decorated with different molar ratios of ZnO:SnO<sub>2</sub> Zinc Stannate NP's presents higher responses (up to 3 times) compared to bare graphene.

## 4. Conclusions

In Summary, we have successfully synthesized cubic Zinc Stannate Nanoparticles with different molar ratios and used them for bare graphene decoration to fabricate a chemoresistive sensor with enhanced gas sensing properties. These decorated nanolayers showed promising results regarding NO<sub>2</sub> sensing at very low concentrations compared to the bare one, also we noticed the slight enhancement effect of the change of the molar ratios on the sensing property of the bare graphene where the 2:1 Zinc stannate decorated nanolayers shows a slightly higher responses to the Nitrogen Dioxide than the 4:1 Zinc Stannate decorated Zinc stannate Graphene.

## 6. Graphs

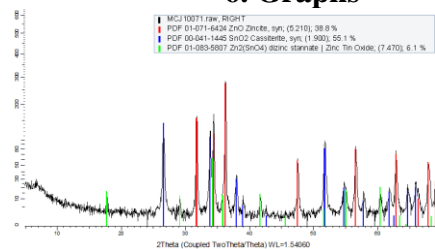


**Fig.1.a** Xray Diffraction graph for synthesized 2:1 Zinc Stannate nanoparticles

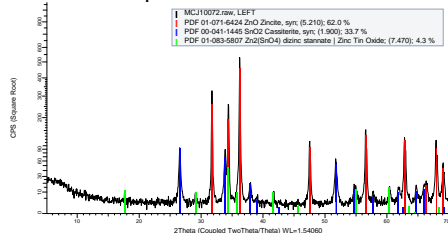


**Fig.1.b** Xray Diffraction graph for synthesized 4:1 Zinc Stannate nanoparticles

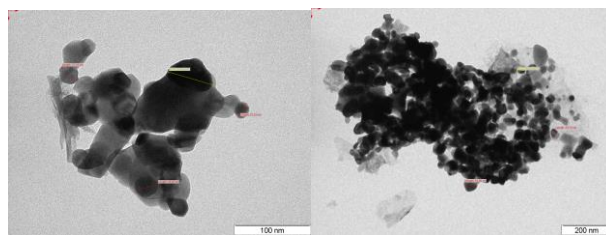


**Fig.2.a** TEM Image showing the size and shape of 2:1 Zn<sub>2</sub>SnO<sub>4</sub> NP's.

**Fig.2.b** TEM Image showing the size and shape of 4:1 Zn<sub>2</sub>SnO<sub>4</sub> NP's

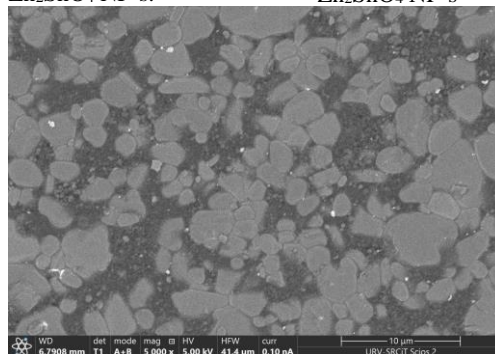


**Fig.3.a** FESEM image recorded with Back-Scattered Electron (BSE) detector, showing the graphene decorated with 2:1 perovskite nanocrystals (bright spots).

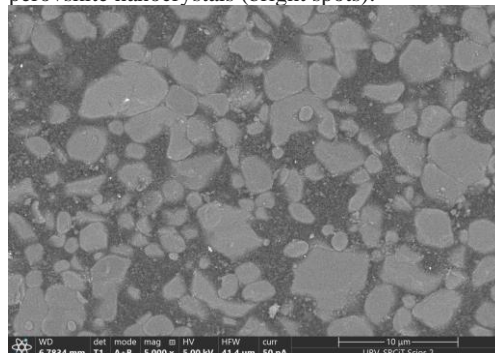


**Fig.3.b** FESEM image recorded with Back-Scattered Electron (BSE) detector, showing the graphene decorated with 4:1 perovskite nanocrystals (bright spots).

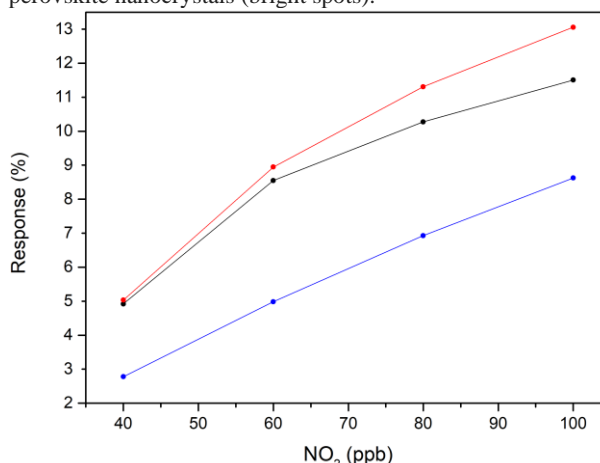


**Fig.4.** Calibration curves obtained for decorated Graphene with 4:1 Zinc Stannate NP's (red), Graphene decorated with 4:1 Zinc Stannate (black) and bare Graphene (Blue) detecting different concentrations of NO<sub>2</sub> at ppb range.

# Modelization and annotation of peptides to reconstruct the spatial distribution of proteins in MALDI MSI using rMSIannotation.

Lluc Sementé<sup>1</sup>, Mari García-Altres<sup>1,3</sup>, Xavier Correig<sup>1,2,3</sup>, Pere Ràfols<sup>1,2,3</sup>

<sup>1</sup> Department of Electronic Engineering, Rovira i Virgili University, Tarragona, Spain;

<sup>2</sup> Institut d'Investigació Sanitària Pere Virgili, Tarragona, Spain;

<sup>3</sup> Spanish Biomedical Research Centre in Diabetes and Associated Metabolic Disorders (CIBERDEM), Madrid, Spain;

## 1. Introduction

Mass spectrometry imaging (MSI) is capable of sampling the spatial distribution of various families of compounds by tuning the sample preparation to the target compounds. Matrix assisted laser desorption/ionization (MALDI) is a trendy MSI technology that combines a soft ionization source with the application of a matrix to enhance the ionization of specific compounds. The versatility in sample preparation procedures allows to obtain spectra from low mass compounds like metabolites or lipids (100 to 1000 Da), to long chains of peptides or intact small proteins (up to 30k Da).

Usually, when the target compounds are proteins, the sample preparation includes enzymes to digest the proteins and cleave them in smaller peptide chains. This allows to work with Formalin-Fixed Paraffin-Embedded (FFPE) samples and to break down big proteins (impossible to directly measure them), obtaining images of the distribution of their peptides. This procedure generates complex spectra that requires rebuilding the puzzle in order to determine which signals are peptides and which peptides belong to which proteins. To facilitate this task, we have extended the capabilities of the MSI peak annotation tool rMSIannotation[1] to annotate peptides in the spectra up to 6k Da.

## 2. Method

The algorithm input is an rMSIproc peak matrix where, rows represent spectra and columns represent  $m/z$  species. For each  $m/z$  specie, the algorithm searches for other  $m/z$  species that are at one neutron distance (1.003355 Da) and computes the isotopic likelihood score (ILS) which includes three metrics: mass error, correlation and intensity ratio. The measured intensity ratio is compared against a model that links the  $m/z$  ratio of monoisotopic peaks to the intensity ratio of the isotopes in the pattern. The previous iteration of rMSIannotation included a model of the metabolites and lipids in the Human Metabolome Database (HMDB)[2] up to 1200 Da, excluding all peptides and other compounds. Moreover, the modelization of the intensity ratios for metabolites and lipids produced a big bias in the peptides mass range as

peptides have less amount of carbon atoms per Da than metabolites and lipids, and the number of carbon atoms is the main factor for the intensity ratios of a compound. To solve this issue, we have modeled the Human Peptide Atlas[3], a library containing 5 million peptide sequences, and included it in rMSIannotation. Figure 1 shows the difference between the two models included in rMSIannotation. After including the new model, we have annotated the peptides found in a dataset of human colorectal cancer measured with MALDI-FT-ICR containing 1236  $m/z$  features and 10331 spectra. Later, we have compared the annotations with the identifications produced using samples of the same dataset by liquid chromatography mass spectrometry (LC-MS).

## 3. Results

Before implementing the new model, rMSIannotation was capable of annotating only 12 monoisotopic compounds, and all of them in the metabolites and lipids range. After including the new model, rMSIannotation produced 162 monoisotopic peak annotations and 252 isotopic peaks, combined add up to one third of the total number of peaks in the dataset. Moreover, we found 119 adduct relationship between the monoisotopic peaks. After producing the annotations, we have matched them with the library of identified compounds with LC-MS, which includes proton and sodium adducts, with a maximum mass error of 5 ppms. This resulted in 100 matches between both libraries including, most of them, more than one peptide sequence per annotated feature.

## 4. Conclusions

Extending the capabilities of rMSIannotation to the peptides mass range allows to work with new compounds and datasets more reliably using the MSI processing environment rMSIproc[4]. Further work will be directed in discerning the best match for each  $m/z$  feature and the multiple peptide sequences using the adducts information contained in the LC-MS library and the number of carbon atoms measured by rMSIannotation from the data. As this is a common procedure in proteomics for MSI, we expect to be able to standardize this procedure and reach the final goal of linking peptides to the proteins they belong to.

## 5. References

- [1] L. Sementé, G. Baquer, M. García-Altres, X. Correig-Blanchar, and P. Ràfols, “rMSIannotation: a peak annotation tool for mass spectrometry imaging based on the analysis of isotopic intensity ratios,” *Anal. Chim. Acta*, vol. 1171, p. 338669, 2021, doi: 10.1016/j.aca.2021.338669.
- [2] D. S. Wishart et al., “HMDB 4.0: The human metabolome database for 2018,” *Nucleic Acids Res.*, 2018, doi: 10.1093/nar/gkx1089.
- [3] F. Desiere et al., “The PeptideAtlas project,” *Nucleic Acids Res.*, vol. 34, no. Database issue, pp. 655–658, 2006, doi: 10.1093/nar/gkj040.
- [4] P. Ràfols et al., “rMSIproc: an R package for mass spectrometry imaging data processing,” *Bioinformatics*, vol. 36, no. 11, pp. 3618–3619, 2020, doi: 10.1093/bioinformatics/btaa142.

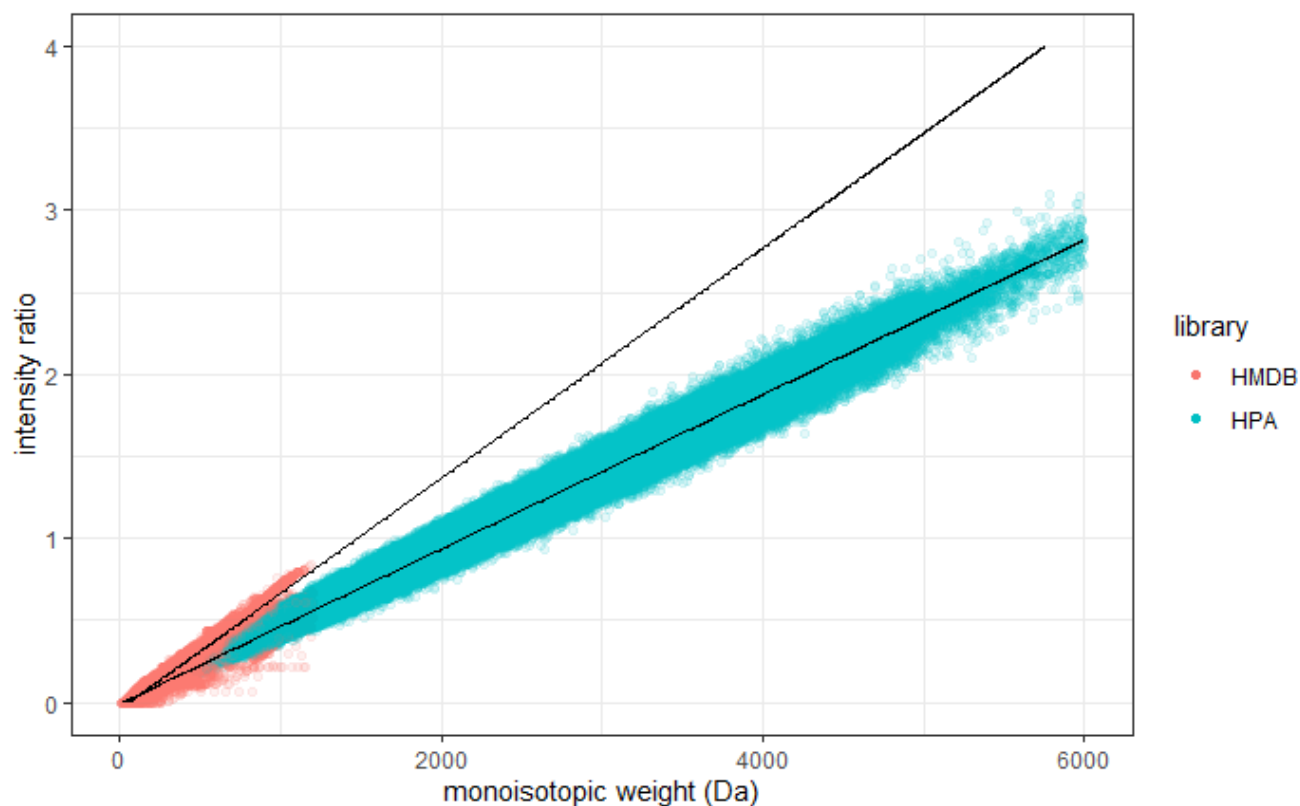


**Figure 1.** Scatter plot of the compounds in the Human Metabolome Database (HMDB) and the Human Peptide Atlas (HPA). Black lines represent the linear models build using both libraries. The discrepancies between them are based on the number of carbon atoms per unit of mass of the families of compounds. rMSIannotation includes both models in order to annotate peaks at both mass ranges.

# 3D assembly of WS<sub>2</sub> nanomaterial for H<sub>2</sub>S gas sensing application

Aanchal Alagh\*, Fatima Ezahra Annanouch\*, Jean François Colomer<sup>†</sup>, Eduard Llobet\*

\*(MINOS-EMaS), Department of Electrical Electronic Engineering and Automation  
Universitat Rovira i Virgili, Tarragona, Spain

<sup>†</sup>Research Group on Carbon Nanostructures (CARBONNAGE) and Laboratoire d'Analyse par Réaction Nucléaires (LARN)<sup>†</sup>, Namur Institute of Structured Matter (NISM), University of Namur,  
61 Rue de Bruxelles, 5000 Namur, Belgium

[alagh.aanchal@urv.cat](mailto:alagh.aanchal@urv.cat), [fatimaezahra.annanouch@urv.cat](mailto:fatimaezahra.annanouch@urv.cat), [jean-francois.colomer@unamur.be](mailto:jean-francois.colomer@unamur.be),  
[eduard.llobet@urv.cat](mailto:eduard.llobet@urv.cat)

## Abstract

Here, we demonstrate a facile route to synthesize a continuous film of WS<sub>2</sub> deposited by a combination of aerosol-assisted chemical vapor deposition (AACVD) with H<sub>2</sub> free atmospheric pressure CVD techniques. This synthesis strategy allows us a direct integration of the sensing material onto the sensor transducer with high growth yield and uniform coverage. SEM and Raman spectroscopy were used to investigate the morphology and composition of the grown material. The performance of WS<sub>2</sub> sensors in the detection of H<sub>2</sub>S has been studied and results show that the synthesized material behaves as a p-type semiconductor with high sensitivity towards H<sub>2</sub>S at sub-ppm level.

Keywords: 2D, TMDs, sensor, APCVD, WS<sub>2</sub>, H<sub>2</sub>S

## Introduction

In recent years, there has been a significant amount of research dedicated to new materials such as transition metal dichalcogenides (TMDs). These two-dimensional (2D) semiconducting TMD materials show exceptional electrochemical properties with tunable band gap and high chemical stability [1]. The rich family of TMDs having chemical formula MX<sub>2</sub> (M = Mo, W; X = S, Se), comprises of about 40 members, which provides plentiful applications for the next generation of flexible and wearable electronics [2]. The ultrathin nature of these materials provides them with exceptional optical and wearable properties with high mechanical flexibility [3].

Despite numerous advantages their application is limited by the synthesis process currently employed to grow films of high quality, with wafer-scale uniformity and layer number controllability [4].

In this regard, we report on the growth of a continuous film of 2D layered WS<sub>2</sub> nanotriangles assembled on 1D WS<sub>2</sub> nanoneedles. The layered film of WS<sub>2</sub> is grown by a combination of AACVD with H<sub>2</sub> free atmospheric pressure CVD technique. The as-grown material is characterized using SEM and Raman spectroscopy to investigate the morphology and composition of the grown material. Moreover, our deposition strategy allows us to directly grow WS<sub>2</sub> film with uniform coverage onto commercial alumina transducer thereby leading to facile sensor fabrication. Henceforth, the

gas-sensing performance of the fabricated sensor is studied, and results demonstrate that the synthesized material behaves as a p-type semiconductor with high sensitivity towards sub-ppm level of H<sub>2</sub>S at low operating temperatures.

## Results and Discussion

Fig. 2 depicts the SEM images of WO<sub>3</sub> and WS<sub>2</sub> films. From the results obtained, WO<sub>3</sub> grown by AACVD technique consisted of thin and elongated NNs of WO<sub>3</sub> which were randomly aligned and homogeneously distributed over the alumina substrate.

After sulfurization, the morphology of these nanoneedles changed completely to form a continuous film of WS<sub>2</sub> having a mixed morphology of NTs and NNs, as shown in Figure 2(b). The composition of the WS<sub>2</sub> films was studied by Raman spectroscopy.

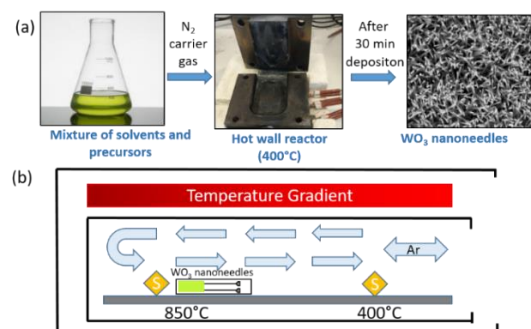


Figure 1 (a) WO<sub>3</sub> synthesis by AACVD process (b) WS<sub>2</sub> synthesis adopting CVD technique

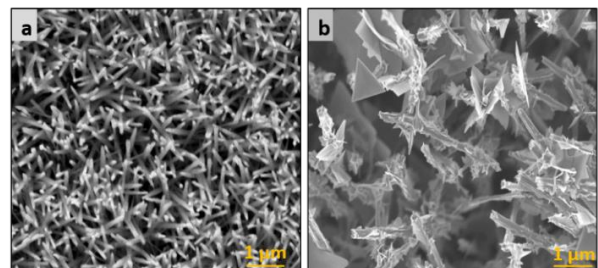


Figure 2 SEM images of (a) WO<sub>3</sub> Nanoneedles (b) WS<sub>2</sub> Nanotriangles attached with nanoneedles



Raman spectroscopy is a powerful technique to evaluate the crystal quality and film thickness of 2D materials and hence is used to analyze the as-fabricated material [5]. Fig.3 depicts Raman spectra obtained for the as-fabricated WS<sub>2</sub> nanofilms and WO<sub>3</sub> NNs. The lower spectrum depicts peaks at 271 cm<sup>-1</sup>, 327 cm<sup>-1</sup>, 715 cm<sup>-1</sup> and 805 cm<sup>-1</sup>, which indicates the formation of monoclinic tungsten trioxide phase, which is in a good accordance with our previous works [6][7]. From the upper spectrum, the two main Raman active modes for 2H-WS<sub>2</sub> were found, E<sup>1</sup><sub>2g</sub> at 348.5 cm<sup>-1</sup> and A<sub>1g</sub> at 414.5 cm<sup>-1</sup>, where A<sub>1g</sub> mode indicates in plane vibrations and E<sup>1</sup><sub>2g</sub> mode indicates out-of-plane vibrations. In addition, two broad peaks at 700 cm<sup>-1</sup> and 803 cm<sup>-1</sup>, were detected with low intensity compared to WS<sub>2</sub> spectrum, indicating the presence of some WO<sub>3</sub> impurities.

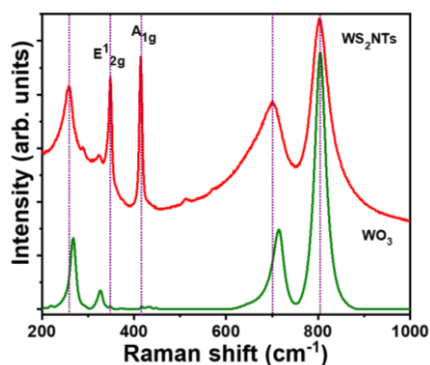


Figure 3 Raman spectrum of the multi-layered WS<sub>2</sub>

Furthermore, Fig.4 (a) and (b) demonstrates the gas sensing results of WS<sub>2</sub> sensor towards 40 and 5 ppm of H<sub>2</sub>S. Gas sensing results demonstrate that the fabricated WS<sub>2</sub> sensor behaves as a p-type semiconductor material: increasing resistance when exposed to a reducing gas such as H<sub>2</sub>S and decreasing resistance when exposed to air and vice-versa. It is observed that the fabricated WS<sub>2</sub> sensor showed very high sensitivity with good stability and repeatability towards the targeted gas even at low operating temperature (150°C). The sensor response was calculated to be 53.05% and 15.6% towards 40 and 5 ppm of hydrogen sulfide gas respectively. During these measurements, the sensor was tested at 150°C towards different concentrations of H<sub>2</sub>S. It is evident from the results obtained that there is an increase in response with each increment in analyte concentration.

### Conclusion

We have successfully deposited WS<sub>2</sub> samples directly on commercial sensor transducers via a combination of two types of CVD techniques. The results obtained show that the sensor is composed of a hybrid structure of nanotriangles and nanoneedles of WS<sub>2</sub> with high quality and crystallinity as confirmed by Raman and SEM characterization techniques. The obtained material was used as a chemoresistive H<sub>2</sub>S gas sensor. Our results demonstrate better sensing performance for WS<sub>2</sub> nanofilms with higher sensitivity towards H<sub>2</sub>S than previously reported for WS<sub>2</sub> nanofilms. This is attributed to

the porous surface and increased number of sulfur edges in WS<sub>2</sub> NTs. These were created by the random 3D assembly of WS<sub>2</sub> nanosheets on WS<sub>2</sub> nanoneedles. This leads us to the conclusion that the morphology and arrangement of WS<sub>2</sub> nanosheets plays a significant role for chemical gas sensing. Hence, our results could be beneficial for future H<sub>2</sub>S gas sensing studies with commercial potential due to the stable and higher responses attained at much lower operating temperature as compared to the traditional metal-oxide based gas sensors. Furthermore, the direct growth of WS<sub>2</sub> nanofilms on the sensor transducer with high degree of scalability and controllability makes the production of these nanofilms much more feasible.

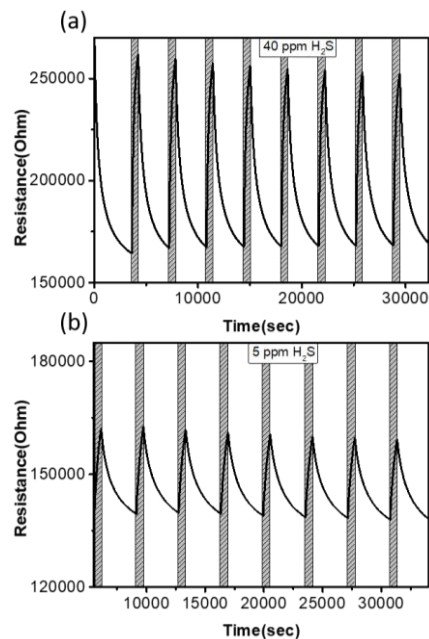


Figure 4 Repeated response and recovery cycles for a WS<sub>2</sub> sensor towards (a) 40 ppm (b) 5 ppm

### Acknowledgement

This project has received funding from the European Union's Horizon 2020 research and innovation programme under the Marie Skłodowska-Curie grant agreement No. 713679.

### References

- [1] A. Alagh, F. E. Annanouch, E. Llobet, U. R. I. Virgili, and A. P. Catalans, "Single-step CVD synthesis of layered WS<sub>2</sub> films for NO<sub>2</sub> gas sensing," *2019 IEEE SENSORS*, no. 2, pp. 1–4, 2020.
- [2] M. Okada *et al.*, "Direct chemical vapor deposition growth of WS<sub>2</sub> atomic layers on hexagonal boron nitride," *ACS Nano*, vol. 8, no. 8, pp. 8273–8277, 2014, doi: 10.1021/nn503093k.
- [3] C. Yan *et al.*, "2D Group IVB Transition Metal Dichalcogenides," *Adv. Funct. Mater.*, vol. 28, no. 39, pp. 1–18, 2018, doi: 10.1002/adfm.201803305.
- [4] J.-G. Song, K. Park, J. Park, and H. Kim, "Vapor Deposition Techniques for Synthesis of Two-Dimensional Transition Metal Dichalcogenides," *Appl. Microsc.*, vol. 45, no. 3, pp. 119–125, 2015, doi: 10.9729/AM.2015.45.3.119.

# Numerical approach to input filter design for switching converters

Ramon Estalella, Angel Cid, Carlos Olalla

Universitat Rovira i Virgili

## Abstract

Switching power converters often require input filters to reduce current and voltage ripple and to comply with conducted electromagnetic interference (EMI) regulations. The design of these filters is typically carried out by hand, using conservative constraints that allow to largely simplify the problem. This paper presents an alternative approach using numerical methods.

## 1. Introduction

When designing an input filter for a switching converter, the main goal is to comply with EMI limitations and limit the performance degradation that such filter could add to the overall system.

Since input filters are typically designed on top of existing converters, designers must consider the possible dynamic interactions that may arise, which may even lead to instability. Usually a second or third order filter is added to a converter, so analysing the dynamics of the entire system can be challenging. For that reason conventional design approaches typically rely on simplifications of the stability criteria to assist on the process.

The basis for what can be considered conventional design is given by [1]. Our goal is to create a numerical method that matches or improves the conventional design method in performance of the overall system, while making the design process of said filter easier and quicker. Another goal would be able to scale up the numerical method to systems of higher complexity.

## 2. Proposed design method

Instead of providing an “optimal” filter we will search for a parameter region that ensures our performance design criteria. Then the designer has a range of filter parameter options to choose from according to other restrictions (cost, weight, etc.). We will base the approach on [2] and on [3] works.

Consider the following continuous-time linear system:

$$\dot{x}(t) = \left( A_0 + \sum_{i=1}^k \alpha_i E_i \right) x(t) \quad (1)$$

where  $x \in \mathbb{R}^n$ ,  $A_0 \in \mathbb{R}^{n \times n}$  is the nominal matrix of the system,  $E_i \in \mathbb{R}^{n \times n}$ ,  $i = 1, \dots, k$  are given matrices representing the direction of perturbation and  $\alpha_i \in \mathbb{R}$ ,  $i = 1, \dots, k$ , define the amount of perturbations allowed.

The aim is to determine the maximum domain  $([-\alpha_m^i, \alpha_M^i])$  where our conditions are ensured. This is accomplished by a heuristic search, previous knowledge of the system can be used to make a more optimized search. A more detailed description of this procedure for just a stability condition is given in [2].

The final designed values for the filter will depend on: the initial values (set on  $A_0$ ), the *scale* parameters (set on  $E_i$ ) and the limits of  $\alpha_i$  found.

For each perturbation direction we can compute the designed parameters by solving

$$A_i = A_0 + \alpha_i E_i \quad (2)$$

## 3. Pole placement conditions

In order to be able to design a filter we need to force some dynamic behaviour apart from simply being stable. This is accomplished by pole placement techniques. Its possible to directly relate the attenuation and the damping ratio to a sphere centred on  $0 + 0j$  with radius  $\rho$  and an angle  $\theta$  respectively (see Figure 1) [4]. With the last one also ensuring the stability of the system.

Starting with the  $\theta$  condition presented on [4] and following a similar procedure to the one described on [2] for the stability LMI we can obtain the pole placement LMIs required to ensure a specified damping ratio  $\zeta = \cos \theta$  (expressions 3 and 4).

For the attenuation we use the condition derived in [3] with the circle centred on  $0 + 0j$  and without state feedback.

$$\begin{pmatrix} \sin\theta(A_j \mathbf{W}_j + \mathbf{W}_j A'_j) & \cos\theta(A_j \mathbf{W}_j - \mathbf{W}_j A'_j) \\ \cos\theta(-A_j \mathbf{W}_j + \mathbf{W}_j A'_j) & \sin\theta(A_j \mathbf{W}_j + \mathbf{W}_j A'_j) \end{pmatrix} < \mathbf{I} \quad ; \quad j = 1, \dots, N \quad (3)$$

$$\begin{pmatrix} \sin\theta(A_j W_k + A_k W_j + W_j A'_k + W_k A'_j) & \cos\theta(A_j W_k + A_k W_j - W_j A'_k - W_k A'_j) \\ \cos\theta(-A_j W_k - A_k W_j + W_j A'_k + W_k A'_j) & \sin\theta(A_j W_k + A_k W_j + W_j A'_k + W_k A'_j) \end{pmatrix} < \frac{1}{N-1} \mathbf{I} \quad (4)$$

$j = 1, \dots, N-1 \quad ; \quad k = j, \dots, N$

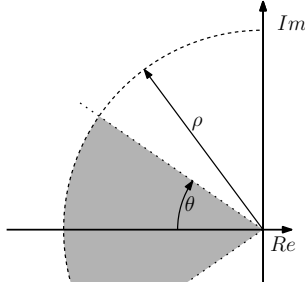


Figure 1: Region defined with the pole placement LMIs

#### 4. Short example

We will apply the previously defined technique to an example RLC filter with the load modelled as a CPL. Load parameters are  $V = 10 \text{ V}$  and  $P = 30 \text{ W}$ . Design conditions are  $\zeta = 0.5$  and minimum attenuation of  $-60 \text{ dB}$  at the switching frequency of  $f_s = 100 \text{ kHz}$ .

Initial and perturbation matrices are defined as follow:

$$A_0 = \begin{pmatrix} -\frac{R_{L_0}}{L_0} & \frac{-1}{C_0} \\ \frac{1}{C_0} & \frac{L_p}{C_0 V^2} \end{pmatrix}; \quad E_1 = \begin{pmatrix} -\frac{R_{L_{scale}}}{L_{scale}} & 0 \\ 0 & 0 \end{pmatrix}; \quad (5)$$

$$E_2 = \begin{pmatrix} 0 & \frac{-1}{L_{scale}} \\ 0 & 0 \end{pmatrix}; \quad E_3 = \begin{pmatrix} 0 & 0 \\ \frac{1}{C_{scale}} & \frac{P}{C_{scale} V^2} \end{pmatrix}$$

In Figure 2 we can see the obtained region of the filter parameters. With the center point being the initial point where the algorithm started the search. This gives us the possibility to choose from a range of different filters that can be used for our system.

#### 5. Conclusions

We have obtained a filter parameter region which has certain performance conditions set by the design criteria. We can now choose any filter defined inside our region according to other design criteria such as cost, size, etc.

Future work would be to improve on the region search, work with different filters/loads and optimize the process.

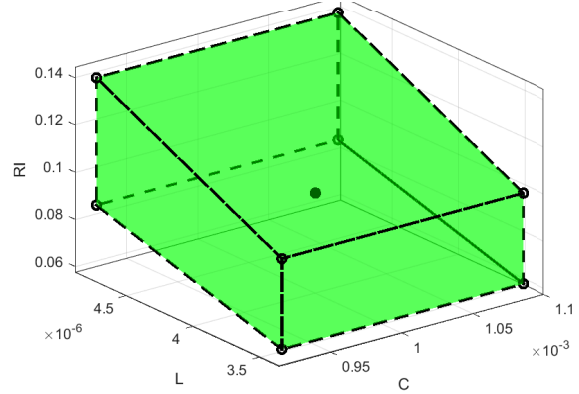


Figure 2: Region of the filter parameters

#### References

- [1] R. W. Erickson and D. Maksimovic, *Fundamentals of Power Electronics 2nd Edition*, February, 2008, ISBN: 0306480484. DOI: 10 . 1017 / CBO9781107415324 . 004. arXiv: arXiv : 1011.1669v3.
- [2] D. C. Ramos and P. L. Peres, "An LMI approach to compute robust stability domains for uncertain linear systems," *Proceedings of the American Control Conference*, vol. 5, no. 2, pp. 4073–4078, 2001, ISSN: 07431619. DOI: 10 . 1109 / ACC . 2001 . 946351.
- [3] V. J. Leite, V. F. Montagner, and P. L. Peres, "Robust pole location by parameter dependent state feedback control," *Proceedings of the IEEE Conference on Decision and Control*, vol. 2, no. December, pp. 1864–1869, 2002, ISSN: 01912216. DOI: 10 . 1109 / cdc . 2002 . 1184796.
- [4] M. Chilali and P. Gahinet, "Design with Pole Place Constraints: An LMI Approach," *Ieee Transactions on Automatic Control*, vol. 41, no. 3, pp. 358–367, 1996.

# An automated annotation tool of lipid adducts and in-source fragments in MALDI-MSI

Gerard Baquer, Lluç Sementé, María García-Altres, Xavier Correig & Pere Ràfols

1 Department of Electronic Engineering, Rovira i Virgili University, Tarragona, Spain.

2 Spanish Biomedical Research Centre in Diabetes and Associated Metabolic Disorders (CIBERDEM), 28029 Madrid, Spain.

3 Institut d'Investigació Sanitària Pere Virgili, Tarragona, Spain.

## Abstract

Matrix-Assisted Laser Desorption Ionization Mass Spectrometry Imaging (MALDI-MSI) reveals the chemical composition and spatial information of tissues. The identification of mass spectrometry signals is challenging given that MALDI-MSI usually lacks chromatographic separation or tandem mass spectrometry. In this work, we use a recent study [1] on the fragmentation pathways and adduct formation of several lipid classes to develop an automated framework to identify lipid fragments and parental ions. The compound matches are ranked using a novel score that demonstrated an area under the curve of 0.77 in a ROC analysis. This indicates a confident molecular annotation without relying on an orthogonal analytical technique.

## 1. Introduction

Matrix-Assisted Laser Desorption Ionization Mass Spectrometry Imaging (MALDI-MSI) is an established analytical technique used in biochemical and medical studies to reveal the chemical composition and spatial information of the tissues under study. Complete and univocal identification of the MS signals of a typical experiment is a major challenge. To achieve this ambitious identification goal, mass spectrometry techniques usually rely on chromatographic separation (LC-MS, GC-MS) or tandem mass spectrometry. However, MALDI-MSI does not include such separation steps and tandem mass spectrometry is hardly performed due to increased data complexity and experimental running time.

As an alternative, many studies have advocated for the use of in-source fragmentation (i.e. fragments generated naturally inside the ion source) as a fast way of obtaining complementary fragmentation information to assist identification. The annotation of fragments can

not only strengthen the degree of confidence of current automatic identification schemes but also reduce their number of misidentifications by excluding the list of fragments.

Recently, Garete et al [1], proposed a thorough study of the fragmentation pathways and adduct formation of 17 lipid classes. Based on this work, we develop an automated framework to automatically identify both: lipid fragments and parental ions. The compound database matches are ranked using two novel metrics.

## 2. Data-base search and ranking

Experimental data is preprocessed using rMSIproc [2]. The user can filter isotopes using rMSIannotation [3]. The resulting peak matrix in centroid mode is used as an input to the annotation algorithm.

The list of  $m/z$  found in the dataset is used to perform a database search considering all adducts and fragmentation pathways for each of the 17 lipid classes reported in Garete et al [1]. LipidMAPS [4] is the default database but other public or in-house alternatives can be used.

The list of matches is then ranked based on two metrics: (1) number of occurrences and (2) spatial correlation of MS signals tentatively assigned to the same lipid. Additionally, the user can opt to also rank according to the adduct likelihood score presented in Garete et al [1].

The result is a ranked table with the following fields: experimental  $m/z$ , lipid, chemical formula, adduct, fragmentation and ranking scores. The table can be filtered to only return the top N candidates for each  $m/z$ .

### 3. Validation & Results

A total of 9 sections of human nevi acquired with MALDI-MSI were used for validation (6 in negative ion mode and 3 in positive ion mode).

In all cases, we report over 80% match (81.5% in positive mode and 86.88% in negative mode) to the manual annotations presented in the original paper [1]. The manual annotations not found with our approach can be attributed to one of the following reasons: (1) using different search databases, (2) miscalculations in the original publication, (3) unidentified adduct reported or (4) ppm errors over the predefined tolerance threshold.

Figure 1 shows an example annotation of experimental mass  $m/z$  885.61 in negative mode. All manual annotations reported in Garete et al [1] are returned by our automated algorithm.

**A**

m/z	annotation	theoretical m/z	abs. error	ppm error
	*[PA_38:2 + DAN - H]-	885.612	0.002	2.716
885.610	*[PC_36:1 - N(CH3)3 + DAN - H]-	885.613	0.003	3.365
	*[PE_36:1 - NH2 + DAN - H]-	885.613	0.003	3.252

**B**

m/z	lipid	fragmentation	adduct	occurrences	correlation	ppm error
885.6096	PC 33:1	-NH3	M+Dan-H	26	0.4379317	4.2140704
885.6096	PC 38:1	-N(CH3)3	M+Dan-H	12	0.4532620	3.9888577
885.6096	PC 38:2	-Cho	M+Dan-H	11	0.3805415	3.8612398
885.6096	PC 35:2	-EtnA	M+Dan-H	21	0.4131532	4.0719042
885.6096	PC 37:2	-CN(CH3)3	M+Dan-H	14	0.4451963	3.9289954
885.6096	PE 36:1	-NH3	M+Dan-H	26	0.4379317	4.2140704
885.6096	PE 38:2	-EtnA	M+Dan-H	21	0.4131532	4.0719042
885.6096	PE 40:2	-CN(CH3)3	M+Dan-H	14	0.4451963	3.9289954
885.6096	PE 34:1	-NH3	M+Dan-H	26	0.4379317	4.2140704
885.6096	PE 36:2	-EtnA	M+Dan-H	21	0.4131532	4.0719042
885.6096	PE 39:1	-N(CH3)3	M+Dan-H	12	0.4532620	3.9888577
885.6096	PE 41:2	-Cho	M+Dan-H	11	0.3805415	3.8612398
885.6096	PS 38:2	-Serine	M+Dan-H	20	0.3892678	3.1805656
885.6096	PG 35:0	2H2O	M+Dan-H	12	0.2231814	4.1103438
885.6096	PI 36:0	-C4H19O5	M+Dan-H	20	0.3818924	3.6275116
885.6096	PI 38:2	-Hex	M+Dan-H	19	0.3668389	3.5297553
885.6096	PI 38:2	-Inositol	M+Dan-H	19	0.3668389	3.5297553
885.6096	PA 38:2		M+Dan-H	7	0.1521611	4.3127085
885.6096	PI 36:1	-P_EtnA	M-	25	0.2389937	2.9730826
885.6096	PC 40:0	-OH	M+Na-2h	28	0.2744027	2.1422655
885.6096	PC 40:0	-C4H18O5	M-2(H2O)	12	0.3780080	0.1249919

**C**

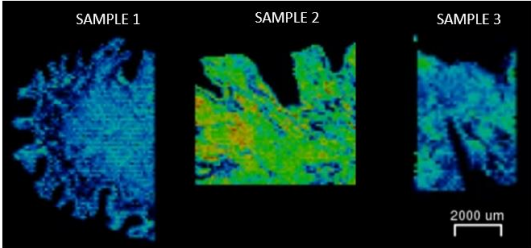


**Fig.1.** Annotation example of  $m/z$  885.61 in negative mode (A) Table of manually reported annotations [1] (B) Table of automated annotations (C) Spatial distribution in two example sections.

A target-decoy strategy [5] is used to estimate the performance of the two ranking metrics proposed (lipid occurrences and lipid correlation). LipidMAPS [4] is the target database and the decoy database is a subset of ChEBI [6] containing lipids and metabolites of non-animal origin (plants, algae, bacteria, fungi, xenobiotics and environmental contaminants). The

decoy database is resampled to match the number of compounds and  $m/z$  distribution of the target. Figure 2 shows that the product of the two ranking metrics obtained an area under the curve of 0.77 in a ROC analysis. This indicates a confident molecular annotation without relying on an orthogonal analytical technique.

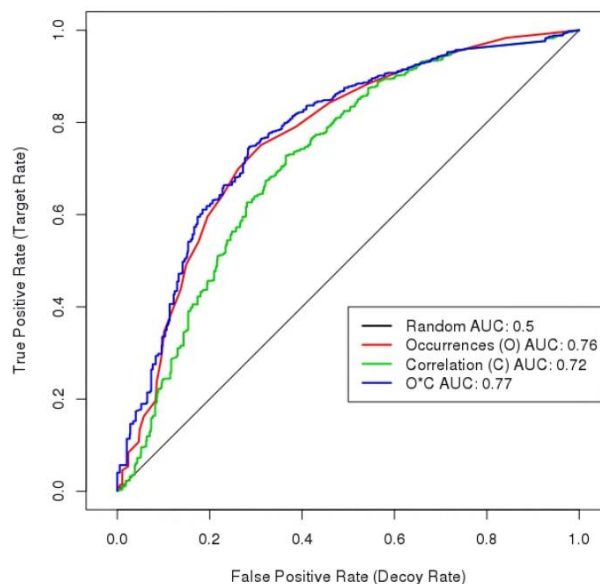


**Fig.2.** Estimation of the ROC curve using a Target-Decoy strategy to evaluate the performance of the two ranking metrics proposed.

### 5. Conclusions

Our approach exploits knowledge about lipid adduct formation and in-source fragmentation pathways to successfully annotate in-source fragments and adducts in MALDI-MSI experiments. This overcomes the intrinsic limitations imposed by the lack of a chromatographic separation step and tandem mass spectrometry.

### References

- [1] J. Garate et al., "Influence of Lipid Fragmentation in the Data Analysis of Imaging Mass Spectrometry Experiments," *J. Am. Soc. Mass Spectrom.*, vol. 31, no. 3, pp. 517–526, Mar. 2020.
- [2] P. Ràfols et al., "RMSIproc: An R package for mass spectrometry imaging data processing," *Bioinformatics*, vol. 36, no. 11, pp. 3618–3619, Jun. 2020.
- [3] L. Sementé, G. Baquer, M. García-Altres, X. Correig-Blanchar, and P. Ràfols, "rMSIannotation: A peak annotation tool for mass spectrometry imaging based on the analysis of isotopic intensity ratios," *Anal. Chim. Acta*, vol. 1171, p. 338669, Aug. 2021.
- [4] E. Fahy et al., "Update of the LIPID MAPS comprehensive classification system for lipids," *Journal of Lipid Research*, vol. 50, no. SUPPL. Elsevier, pp. S9–S14, 01-Apr-2009.
- [5] A. Palmer et al., "FDR-controlled metabolite



annotation for high-resolution imaging mass spectrometry,” *Nat. Methods*, vol. 14, no. 1, pp. 57–60, Dec. 2016.

[6] J. Hastings et al., “ChEBI in 2016: Improved services and an expanding collection of metabolites,” *Nucleic Acids Res.*, vol. 44, no. D1, pp. D1214–D1219, Jan. 2016.



# MS2ID: An R package for high throughput mass spectral annotation

J.M. Badia<sup>1,2</sup>, J. Capellades<sup>1</sup>, G. Baquer<sup>1</sup>, R. Giné<sup>1</sup>, O. Yanes<sup>1</sup>, M. Vinaixa<sup>1</sup>

<sup>1</sup> MIL@b, Department of Electronic Engineering, Metabolomics Platform, IISPV, Universitat Rovira i Virgili<sup>2</sup> Email: josepmaria.badia@estudiants.urv.cat

## Abstract

Unknown to known fragmentation spectra comparison is still the preferential method to annotate tandem mass spectrometry (MS2 or MS/MS) data and to identify metabolites in mass spectrometry-based metabolomics. Currently, no freeware tool exists to compare high throughput experimental mass spectra against public or in-house libraries. Here, we present MS2ID, an R package for fast annotation of large sets of mass spectra using public or in-house spectral repositories. MS2ID is compatible with the packages CompoundDB and Spectra and offers a graphical user interface (GUI) to facilitate visual inspection of the results.

## 1. Introduction

Comprehensive metabolome analyses by LC-MS are essential for biomedical, environmental and biotechnological research [1]. Metabolite annotation and identification are crucial steps in LC/MS-based metabolomics to obtain biologically interpretable results. Annotation commonly relies on the comparison of experimentally obtained fragmentation spectra (MS/MS) against reference spectral databases (that contain spectra from known purified standards). Moreover, increasingly large size of mass spectral databases (typically multi-gigabyte data sets) calls for a conceptually new matching algorithm where the spectra can be compared against the whole library without causing a considerable computational overload. Currently, there are no open-source approaches to annotate MS/MS data in a high throughput manner. The development of open-source solutions to annotate compounds by MS/MS spectral comparison has been hampered by the inner nature of publicly available MS databases usually being constructed in distinct structure and file formats, among various repositories such as HMDB [2], Massbank, GNPS and others [3]. Some tools addressing this limitation have recently emerged. M. Wang et al, presented MASST [4] - a web engine for single MS/MS spectrum search against combined public repositories. On the other hand, CompoundDB [5] automatically creates R-based compound databases generated from publicly available mass spectral repositories and offers

low-throughput tools for MS/MS comparison. Here we describe MS2ID, an R package that compares efficiently experimental MS/MS spectra against a compact in-house spectral library populated with publicly available spectral repositories.

## 2. Implementation

MS2ID is an R package for high-throughput compound annotation using open-source mass spectral libraries. The MS2ID object operates as a spectral database, and its pivotal method annotates query mass spectra (in mzML format) towards an Annot object. This final object also contains the metadata and the spectral data linked to the resulting annotations. In addition, MS2ID features a GUI application to browse and visualize Annot objects.

### 2.1 MS2ID class

The MS2ID constructor mutates primal libraries into a reusable MS2ID object. Primal libraries can be obtained from in-house databases or parsed - using the CompoundDb package - from public repositories, such as HMDB, MoNA, or LIPID MAPS. The MS2ID function bins, merges, and, optionally, compacts the libraries: spectra with the same fragmentation pattern and metabolites with identical InChIKey are eliminated. Figure 1 shows the reduction ratios obtained by compacting HMDB and MoNA MS/MS spectra databases; the resulting MS2ID object is reduced to 34% and 28% of the original spectra and metabolites, respectively. Finally, the function indexes in a table (named fragments index) all the mass fragments (no precursor masses) present in the reference spectra database. This table speeds up the annotation algorithm by locating quickly which reference spectra have, among its top n fragments, m fragments in common with the query spectrum.

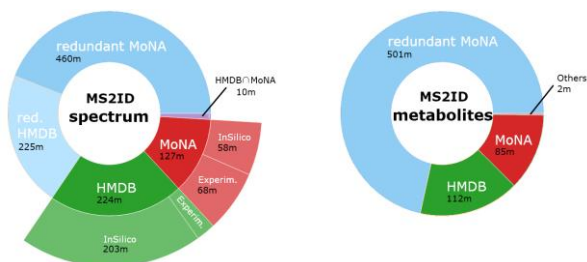


**Fig.1.** MS2ID composition and redundant data

To increase data access efficiency and speed, we established an MS2ID backend that allocates all the data on disk, not in RAM. The backend structure combines two strategies: A SQL database to query the metadata easily and memory-mapped files to read, at a much faster speed, big chunks of spectral and fragments index information [6].

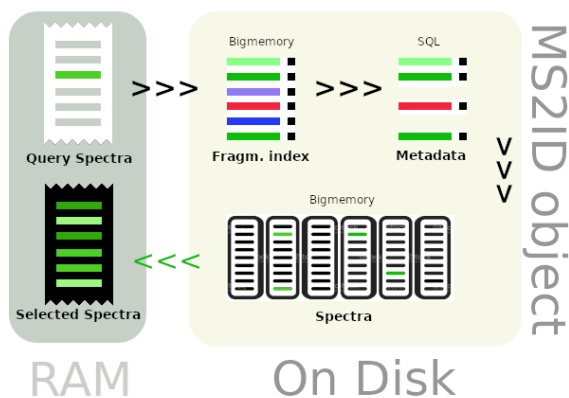


**Fig.2.** Subsetting of spectral data per query spectrum.

## 2.2 MS2ID methods

The annotation method refines mzML data, summarizing clusters of consecutive similar spectra to purge noisy fragments and increase the annotation speed efficiency. Every cluster results in a consensus spectrum made of the fragments present in a minimum percentage of the spectra.

According to fragments and metadata variables (e.g., ionization mode), every consensus spectrum extracts a subset of MS2ID spectra, as Fig. 2 shows, and loads it into memory. Then the algorithm compares them against the consensus spectrum by using different metrics (e.g., cosine similarity, fidelity, or any user-defined function) and embeds the results into an *Annot* object. This object contains all the data related to the annotations to ensure a fully traceable object, and the spectral data uses the *RforMassSpectrometry* package structure to take advantage of its multiples facilities for spectrum handling.

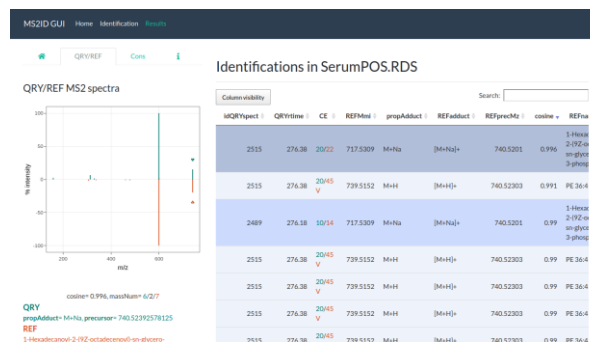


**Fig 3.** MS2ID GUI snapshot

Finally, MS2ID provides a GUI interface to visualize the resulting annotations and the formation of consensus spectrum (Fig. 3).

## 3. Results

The M2ID workflow was applied to the annotation of 20.020 experimental MS/MS spectra (42 mzML files) against a library of 1.436.580 spectra. Annotations took 0.04 s and 0.14 s per experimental spectrum depending on whether the reference spectra were prefiltered by neutral mass or not, respectively. A 64-bit Intel® Core™ i7-8565U CPU @ 1.80GHz × 8, 16 GiB was used, with no parallelization, under Ubuntu 20.04.1 LTS, R 4.0.3v and RStudio 1.3.1093v.

## References

- [1] C. B. Newgard, “Metabolomics and Metabolic Diseases: Where Do We Stand?,” *Cell Metab.*, vol. 25, no. 1, pp. 43–56, Jan. 2017, doi: 10.1016/j.cmet.2016.09.018.
- [2] D. S. Wishart et al., “HMDB 4.0: the human metabolome database for 2018,” *Nucleic Acids Res.*, vol. 46, no. D1, pp. D608–D617, Nov. 2017, doi: 10.1093/nar/gkx1089.
- [3] I. Blaženović, T. Kind, J. Ji, and O. Fiehn, “Software Tools and Approaches for Compound Identification of LC-MS/MS Data in Metabolomics,” *Metabolites*, vol. 8, no. 2, May 2018, doi: 10.3390/metabo8020031.
- [4] M. Wang et al., “Mass spectrometry searches using MASST,” *Nat. Biotechnol.*, vol. 38, no. 1, pp. 23–26, Jan. 2020, doi: 10.1038/s41587-019-0375-9.
- [5] Rainer J, Jan Stanstrup J, (2021). *CompoundDB: Creating and using (chemical) compound databases*. R package version 0.8.0, <https://github.com/EuracBiomedicalResearch/CompoundDb>.
- [6] C. Wang, M.-H. Chen, E. Schifano, J. Wu, and J. Yan, “Statistical Methods and Computing for Big Data,” *arXiv [stat.CO]*, Feb. 27, 2015.
- [7] Gatto L, Rainer J, Gibb S (2021). *Spectra: Spectra Infrastructure for Mass Spectrometry Data*. R package version 1.2.0, <https://github.com/RforMassSpectrometry/Spectra>.